Global climate modeling of Saturn's atmosphere. Part II: Multi-annual high-resolution dynamical simulations

Aymeric Spiga[a,b,*], Sandrine Guerlet[a], Ehouarn Millour[a], Mikel Indurain[a], Yann Meurdesoif[c], Simon Cabanes[a], Thomas Dubos[a], Jérémy Leconte[d], Alexandre Boissinot[a], Sébastien Lebonnois[a], Mélody Sylvestre[a,e,f], Thierry Fouchet[f]

[a] Laboratoire de Météorologie Dynamique/Institut Pierre-Simon Laplace (LMD/IPSL), Sorbonne Université, Centre National de la Recherche Scientifique (CNRS), École Polytechnique, École Normale Supérieure (ENS), Campus Pierre et Marie Curie BC99, 4 place Jussieu, Paris 75005, France
[b] Institut Universitaire de France (IUF), 1 rue Descartes, Paris 75005, France
[c] Laboratoire des Sciences du Climat et de l'Environnement (LSCE/IPSL), Commissariat à l'énergie atomique et aux énergies alternatives (CEA), Centre National de la Recherche Scientifique, Université Paris-Saclay, Campus du CEA - Orme des Merisiers, Saclay, France
[d] Laboratoire d'Astrophysique de Bordeaux (LAB), Univ. Bordeaux, Centre National de la Recherche Scientifique (CNRS), B18N, allée Geoffroy Saint-Hilaire, Pessac 33615, France
[e] School of Earth Sciences, University of Bristol, Wills Memorial Building, Queens Road, Bristol BS8 1RJ, UK
[f] Laboratoire d'Études Spatiales et d'Instrumentation en Astrophysique (LESIA), Observatoire de Paris, Université Paris Sciences et Lettres (PSL), Centre National de la Recherche Scientifique (CNRS), Sorbonne Université, Univ. Paris Diderot, 5 place Jules Janssen, Meudon 92195, France

A B S T R A C T

The Cassini mission unveiled the intense and diverse activity in Saturn's atmosphere: banded jets, waves, vortices, equatorial oscillations. To set the path towards a better understanding of those phenomena, we performed high-resolution multi-annual numerical simulations of Saturn's atmospheric dynamics. We built a new Global Climate Model [GCM] for Saturn, named the Saturn DYNAMICO GCM, by combining a radiative-seasonal model tailored for Saturn to a hydrodynamical solver based on an icosahedral grid suitable for massively-parallel architectures. The impact of numerical dissipation, and the conservation of angular momentum, are examined in the model before a reference simulation employing the Saturn DYNAMICO GCM with a $1/2°$ latitude-longitude resolution is considered for analysis. Mid-latitude banded jets showing similarity with observations are reproduced by our model. Those jets are accelerated and maintained by eddy momentum transfers to the mean flow, with the magnitude of momentum fluxes compliant with the observed values. The eddy activity is not regularly distributed with time, but appears as bursts; both barotropic and baroclinic instabilities could play a role in the eddy activity. The steady-state latitude of occurrence of jets is controlled by poleward migration during the spin-up of our model. At the equator, a weakly-superrotating tropospheric jet and vertically-stacked alternating stratospheric jets are obtained in our GCM simulations. The model produces Yanai (Rossby-gravity), Rossby and Kelvin waves at the equator, as well as extratropical Rossby waves, and large-scale vortices in polar regions. Challenges remain to reproduce Saturn's powerful superrotating jet and hexagon-shaped circumpolar jet in the troposphere, and downward-propagating equatorial oscillation in the stratosphere.

1. Introduction

It has been decades since Saturn's meteorological phenomena observed by Earth-based and space telescopes, and the pioneering Voyager missions, are challenging the fundamental knowledge of geophysical fluid mechanics (e.g., Ingersoll, 1990; Dowling, 1995). Yet, a mission as richly instrumented as Cassini (Porco et al., 2005), offering from 2004 to 2017 an unprecedented spatial and seasonal coverage of Saturn's weather layer, brought a new impulse to the studies of giant planets' atmospheric dynamics (e.g., review papers by Del Genio et al., 2009; Showman et al., 2018a).

In Saturn's troposphere, the Cassini measurements confirmed the banded structure of alternating westward (retrograde) and eastward (prograde) jets, which features a $450\,\mathrm{m\,s^{-1}}$ super-rotating equatorial jet (Porco et al., 2005; García-Melendo et al., 2010; Studwell et al., 2018). Furthermore, the Cassini instruments assessed the remarkable stability of the enigmatic hexagonal jet in the northern polar region (Baines et al., 2009; Sánchez-Lavega et al., 2014; Antuñano et al., 2015; Fletcher et al., 2018), with exquisite details on the structure of the turbulent polar vortex (Sayanagi et al., 2017; Baines et al., 2018). They also offered a detailed record of mid-latitude convective storms (Dyudina et al., 2007; del Río-Gaztelurrutia et al., 2012) and vortices (Vasavada et al., 2006; Dyudina et al., 2008; Trammell et al., 2016; del Río-Gaztelurrutia et al., 2018), including a chain of infrared bright

---

spots named the "String of Pearls" (Sayanagi et al., 2014) and an exceptional coverage of Saturn's latest Great White Spot (Fischer et al., 2011; Sánchez-Lavega, 2011; Sayanagi et al., 2013). Cassini observations of Saturn's cloud layer was also employed to demonstrate the high rate of conversion of energy from eddies to jets (Del Genio et al., 2007; Del Genio and Barbara, 2012), to detail the structure of vorticity (Read et al., 2009a), and to explore Jupiter's and Saturn's atmospheric energetic spectra across spatial scales (Galperin et al., 2014; Young and Read, 2017), confirming pre-Cassini theoretical studies about geostrophic turbulence and the inverse energy cascade (Sukoriansky et al., 2002). All those observations strongly suggest that large-scale tropospheric banded jets emerge from forcing by smaller-scale eddies and waves arising from hydrodynamical instabilities.

In Saturn's stratosphere, not only the Cassini instruments led to key discoveries, but the longevity of the mission permitted a seasonal monitoring of the unveiled phenomena. Cassini's highlights in atmospheric science for the stratosphere include a spectacular stratospheric warming associated with the 2010 Great White Spot (Fletcher et al., 2011b; Fletcher et al., 2012; Fouchet et al., 2016), an equatorial oscillation of temperature in Saturn's stratosphere (Fouchet et al., 2008; Guerlet et al., 2011; Li et al., 2011) with semi-annual periodicity (Orton et al., 2008; Guerlet et al., 2018), and a seasonal monitoring of the meridional distribution of Saturn's stratospheric hydrocarbons (Guerlet et al., 2009; Guerlet et al., 2010; Sinclair et al., 2013; Fletcher et al., 2015; Sylvestre et al., 2015; Guerlet et al., 2015b), hinting at a possible interhemispheric transport of chemical species. Cassini measurements even enabled to link a disruption in the downward propagation of the equatorial oscillation to the 2010 Great White Spot occurrence (Fletcher et al., 2017). Analogies can be drawn between Saturn's and the Earth's stratospheres (Dowling, 2008). Saturn's equatorial oscillation is reminiscent of Earth's Quasi-Biennal Oscillation and Semi-Annual Oscillation (Andrews et al., 1987; Baldwin et al., 2001; Lott and Guez, 2013; Guerlet et al., 2018), driven by the propagation and breaking of Rossby, Kelvin and inertio-gravity waves. The interhemispheric transport of chemical species, which may affect the hydrocarbons distribution, might be analogous to the Earth's Brewer-Dobson circulation (Butchart, 2014).

In this stimulating observational context, new modeling efforts are needed to broaden the knowledge of Saturn's atmospheric dynamics by demonstrating the mechanisms underlying the above-mentioned observed phenomena. A great deal of past modeling work focused on the processes responsible for the banded tropospheric jets. A major difficulty with a giant planet is that the depth at which the atmosphere merges with the internal dynamo region and the strength at which the atmospheric circulations couple with magnetic disturbances have remained poorly constrained by observations (Ingersoll, 1990; Liu et al., 2008) until gravity measurements were recently performed on board Juno and Cassini (Kaspi, 2013; Galanti and Kaspi, 2017; Kaspi et al., 2018; Galanti et al., 2019). Two distinct modeling approaches have been adopted to account for Saturn's tropospheric jets: "shallow-forcing" climate models [see next paragraph for references] account for processes in the weather layer (baroclinic instability, moist convective storms), while "deep-forcing" dynamo-like models (Heimpel et al., 2005; Yano et al., 2005; Kaspi et al., 2009; Heimpel and Gómez Pérez, 2011; Gastine et al., 2014; Heimpel et al., 2016; Cabanes et al., 2017) resolve convection throughout gas giants' molecular envelopes. Contrary to deep models, shallow climate models have had difficulties reproducing gas giants' equatorial super-rotating jets. This has been overcome by including either bottom drag and intrinsic heat fluxes to simulate deep interior phenomena (Lian and Showman, 2008; Schneider and Liu, 2009; Liu and Schneider, 2010), or latent heating by moist convective storms (Lian and Showman, 2010), although the simulated equatorial jets are still about twice as less strong in simulations than in observations (e.g., García-Melendo et al., 2010). The situation for off-equatorial jets is reversed, with better agreement with observations obtained by shallow models compared to deep models,

although the latter can be modified to obtain more realistic results (Heimpel et al., 2005). The recent results from the Juno mission for Jupiter (Kaspi et al., 2018; Guillot et al., 2018) and the Cassini mission for Saturn (Galanti et al., 2019) show that banded jets extend several thousand kilometers below the cloud layer, i.e. deeper than what shallow models consider and shallower than what deep models consider, which probably indicates that shallow and deep models have both their virtues to represent part of the reality.

Here, we adopt the approach of "shallow-forcing" climate modeling to study Saturn. In the last decade, the traditional approach using idealized modeling (Cho and Polvani, 1996; Williams, 2003; Vasavada and Showman, 2005) – which still has great value to study how baroclinic and barotropic instabilities shape Saturn's jets (Li et al., 2006; Kaspi and Flierl, 2007; Showman, 2007), including its polar hexagonal jet (Rostami et al., 2017) and central vortex (O'Neill et al., 2015) – has been complemented by the development of complete three-dimensional Global Climate Models (GCMs) for Saturn and giant planets (Dowling et al., 2006, 1998; Lian and Showman, 2010; Liu and Schneider, 2010; Young et al., 2019a,b). A GCM is obtained by coupling a hydrodynamical solver of the Navier-Stokes equations for the atmospheric fluid on the sphere (the GCM's "dynamical core") with realistic models for physical processes operating at unresolved scales: radiation, turbulent mixing, phase changes, chemistry (the GCM's "physical packages"). Most of those existing GCM studies for Saturn address the formation of tropospheric jets by angular momentum transfer through eddies and waves, often with either a theoretical approach aiming to address giant planets' atmospheric dynamics (Schneider and Liu, 2009; Lian and Showman, 2010; Liu and Schneider, 2010, 2015) rather than a focused approach aiming to address Saturn specifically, or with a limited-domain approach using a latitudinal channel enclosing one specific jet to explain structures such as the Ribbon wave or the String of Pearls (Sayanagi et al., 2014, 2010), to investigate the impact of convective outbursts (Sayanagi and Showman, 2007; García-Melendo et al., 2013), or to discuss the polar hexagonal jet (Morales-Juberías et al., 2011, 2015). The idealized GCM approach can also be employed to study equatorial oscillations in gas giants (Showman et al., 2018b). All those existing studies use simple radiative forcing rather than computing a realistic "physical package" that includes seasonally-varying radiative transfer. The latter approach has been explored to study Saturn's stratosphere, either to constrain large-scale advection / eddy mixing in photochemical models (Friedson and Moses, 2012), or to build a modeling framework applicable to extrasolar hot gas giants (Medvedev et al., 2013). Those studies of Saturn's stratosphere make use, however, of prescribed, *ad hoc*, tropospheric jets.

The existing body of work on "shallow-forcing" modeling has thus paved the path towards a complete three-dimensional Global Climate Model (GCM) for giant planets. However, such a complete troposphere-to-stratosphere GCM for Saturn, capable to address the theoretical challenges opened by observations is yet to emerge. We propose that four challenges shall be overcome to develop a complete state-of-the-art GCM for Saturn and gas giants.

C_1 The radiative transfer computations necessary to predict the evolution of atmospheric temperature, especially in the stratosphere, must be optimized for integration over decade-long giant planets' years, while still keeping robustness against observations.

C_2 Large-scale jets and vortices emerge from smaller-scale hydrodynamical eddies, through an inverse energy cascade driven by geostrophic turbulence. Relevant interaction scales (e.g. Rossby deformation radius) are only 1° latitude-longitude in gas giants vs. 20° on the Earth, making eddy-resolving global simulations over a full year four orders of magnitude more computationally expensive in gas giants.

C_3 Terrestrial experience shows that models need to extend from the troposphere to the stratosphere with sufficient vertical resolution to resolve the vertical propagation of waves responsible for large-

scale structures in both parts of the atmosphere. Moreover, a specific requirement of giant planets is to extend the model high enough in the stratosphere to model the photochemistry of key hydrocarbons impacting stratospheric temperatures (Hue et al., 2016).

C_4 Climate models cannot extend neither deep enough to predict how tropospheric jets interact with interior convective fluxes and planetary magnetic field (Kaspi et al., 2009; Heimpel and Gómez Pérez, 2011), nor high enough to capture the coupling of stratospheric circulations with thermospheric and ionospheric processes (Müller-Wodarg et al., 2012; Koskinen et al., 2015). A suitable approach to couple the weather layer with either the slowly-evolving convective interior, or the rapidly-evolving ionized external layers, remains elusive.

Here, we report the development and preliminary dynamical simulations of a new Saturn GCM at Laboratoire de Météorologie Dynamique (LMD), which aims at understanding the seasonal variability, large-scale circulations, and eddy & wave activity in Saturn's troposphere and stratosphere. It is a first step to further design a modeling platform dedicated to atmospheric circulations of Saturn and other solar system's giant planets. Challenge C_1 about building fast and accurate radiative transfer for the Saturn GCM is addressed in Guerlet et al. (2014). In Guerlet et al. (2014), which serves as Part I for the present study, a seasonal radiative–convective model of Saturn's upper troposphere and stratosphere is described and the sensitivity to composition, aerosols, internal heat flux and ring shadowing is assessed, with comparisons to the observed thermal structure by Cassini and ground-based telescopes. In this Part II paper, we address Challenge C_2 by performing high-resolution dynamical simulations with our Saturn GCM. Our GCM is built by coupling the physical packages (notably, radiative transfer) of Guerlet et al. (2014) with DYNAMICO, a new dynamical core developed at LMD which uses an original icosahedral mapping of the planetary sphere to ensure excellent conservation and scalability properties in massively parallel resources (Dubos et al., 2015). We describe here the insights gained from GCM simulations at high horizontal resolutions (reference at 1/2° latitude/longitude, and tests at 1/4° and 1/8°) with two unprecedented characteristics at those horizontal resolutions: inclusion of realistic radiative transfer and long integration times up to fifteen simulated Saturn years.

The paper is organized as follows. Notations are defined in Table 1. In Section 2, we provide details on the characteristics of our Saturn DYNAMICO GCM, and the assumptions and settings adopted for the simulations discussed in subsequent sections, with Appendix A featuring a necessary analysis of the impact of horizontal dissipation and the conservation of angular momentum in our Saturn GCM. In Section 3, we describe the results obtained with our reference 15-year-long 1/2° Saturn DYNAMICO GCM simulation, with an emphasis on the driving and evolution of jets in Section 4. In Section 5, we summarize our conclusions and draw perspectives for future improvements of our Saturn DYNAMICO GCM needed to fully achieve challenges C_2, C_3 and C_4, as it comes to no surprise that the present study is only a preliminary path towards fulfilling arguably ambitious scientific goals.

2. Characteristics of the Saturn DYNAMICO GCM

2.1. Building the model

As is reminded in the introduction, a GCM consists in coupling a dynamical core interfaced with physical packages (or parameterizations). Our project to develop a Saturn GCM started by the development of the latter: the physical packages used in our GCM are described in full detail in Guerlet et al. (2014). Our model's radiative computations are based on a versatile correlated-k method, suitable for any planetary composition (Wordsworth et al., 2010; Charnay et al., 2013; Leconte et al., 2013) with k-coefficients derived from detailed line-by-line

Table 1

Physical quantities used in the paper. The numerical values provided in the right column corresponds to the values set in our Global Climate Model (Section 2.2).

Coordinates		
t	Time	s
(λ, φ)	Longitude, Latitude	°E, °N
(x,y)	WE coordinate, SN coordinate (local frame)	m
z	Altitude	m
L_s	Saturn's heliocentric longitude (0° N spring)	°
Meteorological variables		
p	Pressure	Pa
T	Temperature	K
u	Zonal wind component (W → E)	m s^{-1}
v	Meridional wind component (S → N)	m s^{-1}
w	Vertical wind component	m s^{-1}
m	Atmospheric mass	kg
$\mathcal{M}$	Axial Angular Momentum (AAM)	kg m^2 s^{-1}
μ	Specific AAM (per unit mass, Eq. (18))	m^2 s^{-1}
ζ	Relative vorticity (vertical component $-\partial u/\partial y + \partial v/\partial x$)	m s^{-2}
q	Ertel potential vorticity	kg m^2 s^{-1} K^{-1}
Planetary parameters and model settings		
Ω	Rotation rate[★]	1.651×10^{-4} s^{-1}
ω	Obliquity	26.73°
g	Acceleration of gravity	10.44 m s^{-2}
a	Planetary radius	6.0268×10^7 m
c_p	Specific heat capacity	11,500 J kg^{-1} K^{-1}
M	Molecular mass	2.34 g mol^{-1}
R	Ideal gas constant normalized with M	0.309 c_p
Φ_i	Internal heat flux	2.6 W m^{-2}
τ_R	Timescale for bottom Rayleigh drag	100 Earth days
φ_R	Minimum latitude ($\pm \varphi_R$) for bottom drag	33°
Computations		
$f = 2\,\Omega \sin \varphi$	Coriolis parameter at latitude φ	s^{-1}
$\beta = \frac{\partial f}{\partial y} = \frac{2\,\Omega \cos \varphi}{a}$	Beta parameter (meridional derivative of f)	m^{-1} s^{-1}
$H = \frac{R\,T}{g}$	Atmospheric scale height	m
$N^2 = \frac{g}{\theta}\,\frac{\partial \theta}{\partial z}$	Brunt-Väisälä frequency	s^{-2}
$\bar{\psi}$	Axisymmetric component of variable ψ	Zonal average
$\psi' = \psi - \bar{\psi}$	Eddy[†] component of variable ψ	Zonal anomaly

[★] The rotation rate corresponds to Saturn "days" of 38,052 s, according to the value obtained in Read et al. (2009b) using an approach based on potential vorticity (denoted System IIIw).

[†] Eddies are defined as deviations (perturbations) from the zonal-mean flow and can represent the effects of turbulence, waves, and instabilities.

computations using the HITRAN spectroscopic database (Rothman et al., 2013). Radiative contributions include the three main hydrocarbons (methane, ethane and acetylene), the broad H_2-H_2 and H_2-He collision-induced absorption (Wordsworth, 2012), and tropospheric and stratospheric aerosols layers. Our radiative computations also feature ring shadowing (Appendix A in Guerlet et al., 2014) and account for internal heat flux independent with latitude (Section 2 in Guerlet et al., 2014) .

The spectral discretization of the correlated-k model is optimized for Saturn, with a particular emphasis on accounting for absorption and emission bands of stratospheric methane CH_4 (the prominent driver of Saturn's stratospheric heating), and other hydrocarbons produced by its photodissociation (ethane C_2H_6 and acetylene C_2H_2, the prominent drivers of Saturn's stratospheric cooling). Compared to Guerlet et al. (2014), the line list for methane has been updated beyond 9200 cm^{-1} (Rey et al., 2018, in lieu of the Karkoschka and Tomasko, 2010 band model) and the two main isotopes $^{13}CH_4$ and CH_3D are now included. This improves the predicted temperatures in the middle stratosphere (1–10 mbar) by about 2 K. The vertical profiles of hydrocarbons'

abundances are held constant with latitude and season, and set as is described in Guerlet et al. (2014) using a combination of Cassini observations (Guerlet et al., 2009) and photochemical modeling (Moses et al., 2000). Variations up to 100% of acetylene abundance are observed at high latitudes (Fletcher et al., 2015, note that Sylvestre et al. (2015) found weaker variations) which would entail temperature variations of a couple K in the vicinity of the 1-mbar level (Guerlet et al., 2014, Section 4.4); coupling our radiative model with a seasonal photochemical scheme is considered as a future development for dedicated middle-to-upper stratosphere GCM simulations (see Challenge C_3, as well as Hue et al., 2016, 2018).

Guerlet et al. (2014) showed that this seasonal model allowed for both efficiency and accuracy, with satisfactory comparisons with Cassini measurements — including the observed temperature "knee" caused by heating at the top of the tropospheric aerosol layer, and the meridional gradient between the summer and winter stratosphere (Fletcher et al., 2010a, 2015). Temperatures predicted with our Saturn DYNAMICO GCM are compared with Cassini measurements in Section 3.1.

The need to address specifically Challenge C_2 (i.e. to achieve fine-enough horizontal resolutions in order to predict the arising of smaller-scale eddies and the inverse cascade in the context of geostrophic turbulence) requires the use of a suitable dynamical core in our Saturn GCM. To that end, we chose to employ DYNAMICO, which is developed at LMD as the next state-of-the-art dynamical core for Earth and planetary climate studies (Dubos et al., 2015), and tailored for massively parallel High-Performance Computing resources (scalability tested up to 10^5 cores).

Our dynamical core DYNAMICO solves the primitive hydrostatic equations assuming a shallow atmosphere, i.e. $z \ll a$ (relaxing this assumption to solve the quasi-hydrostatic deep-atmosphere equations is considered for future developments of the model, Tort et al., 2015). The global horizontal mesh in DYNAMICO is set as a quasi-uniform icosahedral C-grid (Dubos et al., 2015) obtained by subdivision of a regular icosahedron: the total number of hexagonal cells is $10 \times N \times N$ corresponding to $N \times N$ sub-triangles subdividing each of the 10 main triangles of the icosahedron grid (N is the parameter by which the horizontal resolution is set in DYNAMICO). Control volumes for mass, tracers and entropy/potential temperature are the hexagonal cells of the Voronoi mesh to avoid the fast numerical modes of the triangular C-grid. Vertical coordinates are mass-based coordinates: "sigma" levels defined as p/p_b where p_b is the pressure at the bottom of the model.

Spatial discretizations in DYNAMICO are formulated following an energy-conserving three-dimensional Hamiltonian approach (Dubos et al., 2015). Time integration is done by an explicit Runge-Kutta scheme (chosen for stability and accuracy). Subgrid-scale (unresolved) dissipation in the horizontal dimension is included as an additional hyperdiffusion term in the vorticity, divergence and temperature equations (see Section A.1). In the vertical dimension, subgrid-scale dissipation is handled in the physical packages through a combination of a Mellor and Yamada (1982) diffusion scheme for small-scale turbulence, and a dry convective adjustment scheme for organized turbulence (convective plumes, see Section 2.4 of Hourdin et al., 1993) . In the case of our Saturn DYNAMICO GCM simulations, the adjustment scheme is the dominant term enabling a neutral profile in the troposphere. This simple adjustment scheme computes the temperature tendencies required to reach the entropy-conserving mixed layer of any convectively-unstable layer appearing in the model. Those characteristics entail that this scheme is not a source of small-scale eddies in the model, which was checked in practice in our Saturn DYNAMICO GCM.

The XIOS library (XML Input/Output Server, Meurdesoif, 2012, 2013) is employed to handle any input/output operations independently from the timeframe imposed by the numerical integrations: not only this improves the efficiency of the numerical integrations in massively-parallel computing clusters, but this also enables for complex operations on computed fields to be carried out during model

runtime rather than as a post-processing operation. Notably, mapping the dynamical fields computed in the non-conformal icosahedral DYNAMICO grid towards a regular latitude-longitude grid, using finite-volume weighting functions, is performed by XIOS directly during our GCM runtime.

2.2. Model settings and boundary conditions

The simulations discussed in this paper are obtained from integrations with our Saturn DYNAMICO GCM employing an horizontal icosahedral mesh with $N = 160$, corresponding to an approximate horizontal resolution of 1/2° in longitude/latitude (hereafter simply referred to as "1/2° simulations"). Test simulations with $N = 301$ (1/4° simulations) and $N = 625$ (1/8° simulations), aimed at model testing rather than scientific exploration, are discussed in Section 5 to open perspectives for future work. The integration, dynamical timestep in the 1/2° Saturn simulations is 118.9125 s. Computations in physical packages are done every 160 dynamical timesteps (i.e. every half a Saturn day) with the exception of radiative computations, which are done every 40 physical timesteps (i.e. every 6400 dynamical timesteps, which is every 20 Saturn days). This means that while the radiative tendency of temperature is added to the dynamical integrations at each physical timestep (every half a Saturn day), it is only updated by our radiative package every 20 Saturn days. This is long compared to what is considered standard in GCMs for terrestrial planets, yet compliant with the comparatively long radiative timescales (or, equivalently, weak radiative forcing) in gas giants. As is indicated in Guerlet et al. (2014), typical radiative timescales on Saturn are longer than a Saturn year below the 400-mbar pressure level and still about a third of a Saturn year at the 10-mbar level. This is much longer than the time-scales of dynamical phenomena (most notably eddies) resolved in the model. We tested that simulations with smaller radiative timesteps yield similar results as reference simulations; we also checked that the diurnal cycle in radiative tendencies is negligible both in Saturn's troposphere and stratosphere.

Our 1/2° simulations feature 32 levels in the vertical dimension, ranging from $p_b \sim 3$ bars at the model bottom, to 1 mbar at the model top. The Saturn DYNAMICO GCM simulations discussed in this paper thus extend from the lower troposphere to the middle stratosphere. Our model top is too low, and our vertical resolution too coarse in the stratosphere, to address Challenge C_3. This shall be improved in further studies dedicated specifically to Saturn's stratospheric phenomena (notably, the equatorial oscillation). Our DYNAMICO model features an optional absorbing ("sponge") layer with a Rayleigh drag acting on the topmost model layers as a surrogate for gravity wave drag in the stratosphere, but we do not use it for the simulations presented in this paper, similarly to previous studies (Schneider and Liu, 2009; Liu and Schneider, 2010). Indeed, Shaw and Shepherd (2007) showed that the inclusion of sponge-layer parameterizations that do not conserve angular momentum (which is the case for Rayleigh drag), or allow for momentum to escape to space, implies a sensitivity of the dynamical results (especially zonal wind speed) to the choice for model top or drag characteristic timescale, because of spurious downward influence when momentum conservation is violated.

Our bottom condition at the 3-bar level is similar to Liu and Schneider (2010). We include a simple Rayleigh-like drag $du/dt = -u/\tau_R$, with a timescale $\tau_R = 100$ Earth days. This drag plays the role devoted to surface friction on terrestrial planets, which allows to close the angular momentum budget through downward control (Haynes and McIntyre, 1987; Haynes et al., 1991). This could also be regarded as a zeroth-order parameterization for Magneto-HydroDynamic (MHD) drag as a result of Lorenz forces acting on jet streams putatively extending to the depths of Saturn's interior (Liu et al., 2008; Galanti et al., 2019), much deeper than the shallow GCM's model bottom. Whether or not including a bottom drag at 3 bars is physically justified is out of the scope of the present paper, and improving on this admittedly simplistic

bottom boundary condition is an entire research goal on its own (part of what we named Challenge C_4). In the present study, we take this bottom drag as an imperfect, yet unambiguous, means to close the angular momentum budget and accounting for deep-seated phenomena in shallow-forcing models for gas giants (Schneider and Liu, 2009; Liu and Schneider, 2010, 2015).

Similarly to Liu and Schneider (2010), the bottom drag is not exerted at equatorial latitudes (i.e. $|\varphi| < \varphi_R = 33°$) as it artificially suppresses the cylindrical barotropic circulation structures that develop along the rotational axis (Taylor columns). This approach mimics the so-called tangent cylinder, which is thought to cause the equatorial super-rotating jets in deep-convective models (Heimpel et al., 2005; Kaspi et al., 2009). The value $\varphi_R = 33°$ is obtained by the geometrical constraint $r_R = a \cos \varphi_R$, with $r_R = 0.84\, a \simeq 50{,}600$ km, ie. a depth of $\simeq 9600$ km below the 1-bar level. This corresponds to the depths at which electrical conductivity significantly increases and the Lorenz drag putatively slows down Saturn's deep jets (Liu et al., 2008). This value of r_R is also consistent with the 8000–10,000 km value of the depth of Saturn's jet streams determined recently from Cassini "Grand Finale" gravity measurements (Galanti et al., 2019).

The initial temperature field in the three-dimensional Saturn DYNAMICO GCM consists in the same vertical profile being set in every grid point of the horizontal mesh. This profile is obtained from uni-dimensional (single-column) computations (à la Guerlet et al., 2014) using the exact same physical parameterizations and vertical discretization than the full Saturn DYNAMICO GCM integrations. The single-column model is initialized with an isothermal profile and run for two Saturn decades to ensure that the annual-mean steady-state radiative-convective equilibrium is reached, especially at the deepest layers at 3 bars (a couple Saturn years is usually enough to reach equilibrium in the stratosphere where radiative timescales are shorter than in the troposphere, see Fig. 1 discussed in Section 3.1). The initial zonal and meridional wind fields in our reference 1/2° Saturn DYNAMICO GCM simulations are set to zero.

Discussions on the impact of numerical dissipation and on the conservation of angular momentum in our DYNAMICO-Saturn model are respectively detailed in Appendices A.1 and A.2.

3. Atmospheric dynamics in our reference Saturn GCM simulation

Hereafter are discussed the results of 15 complete Saturn years simulated by our Saturn DYNAMICO GCM with 1/2° longitude/latitude resolution.

3.1. Thermal structure

The analysis of angular momentum in Appendix A.1 shows that the 15-year duration of simulation ensures dynamical spin-up and that the dynamical fields are in quasi-steady state. Full radiative spin-up must also be ensured, along with dynamical spin-up. In Fig. 1, the evolution

of the mean temperature in the northern hemisphere is shown: as is expected from differences in radiative timescales, the troposphere takes longer to reach steady-state seasonal cycle (about eight Saturn years) than the tropopause level does (about three Saturn years). This shows that satisfactory spin-up, both dynamical and radiative, is ensured starting from the ninth simulated year.

The comparison of our seasonal radiative-convective model with observations, both from instruments on board the Cassini spacecraft and ground-based telescopes, is discussed at length in Guerlet et al. (2014). Yet a sanity check is necessary, given that we now use this model interactively with a three-dimensional dynamical core.

Fig. 2 shows meridional-vertical sections of zonal-mean temperatures, both simulated by our Saturn DYNAMICO GCM and observed by the Cassini/Composite InfraRed Spectrometer (CIRS) instrument in 2015. The model successfully reproduces the vertical transition from troposphere to stratosphere, and the rather flat meridional gradients of temperature at this season ($L_s \sim 70°$). In Fig. 3 (top), the simulated meridional-vertical section of the Brunt-Väisälä frequency N^2 indicates that the radiative-convective transition, between the neutral profile ($N^2 \sim 0$) in the bulk of the troposphere and the stable profile ($N^2 > 0$) in the upper troposphere and lower stratosphere, occurs around 500–600 mbar, which is in agreement with observations (Pérez-Hoyos and Sánchez-Lavega, 2006; Fletcher et al., 2007).

Nevertheless, while a 1–2 K contrast between low latitudes and the pole is observed by Cassini at 500 mbar (Fletcher et al., 2010a, Fig. 3 bottom), the simulated pole-to-equator meridional gradient of temperature in our Saturn DYNAMICO GCM at the 500 mbar level is about 4 K (Fig. 3 bottom). This is half of the meridional gradient simulated by Liu and Schneider (2010), but still at least twice the observed gradient. Most of the incident solar flux on Saturn is absorbed in the upper troposphere haze (Pérez-Hoyos and Sánchez-Lavega, 2006; Fletcher et al., 2007), but our radiative model (Guerlet et al., 2014) shows that the solar flux is not zero at 500 mbar and enough to cause a hemispheric meridional gradient of temperature.

A more detailed comparison than Fig. 2 is displayed in Fig. 4, at two typical pressure levels where Cassini/CIRS is the most sensitive, close to the two solstices within which Cassini was operating. The meridional gradient of temperature, and the seasonal variability thereof, is correctly represented in our model. The fact that summer stratospheric temperatures are 5–10 K too warm compared to CIRS observations was also noted with one-column radiative-convective modeling (Guerlet et al., 2014; Sylvestre et al., 2015) and is not a feature introduced by our dynamical simulations. Putative dynamical effects (e.g. Brewer-Dobson seasonal circulations) had been proposed to explain this discrepancy between radiative models and CIRS observations; however, the adopted setting for our Saturn DYNAMICO GCM simulations does not allow us to address this question that would require to raise the model top above the 1-mbar level.

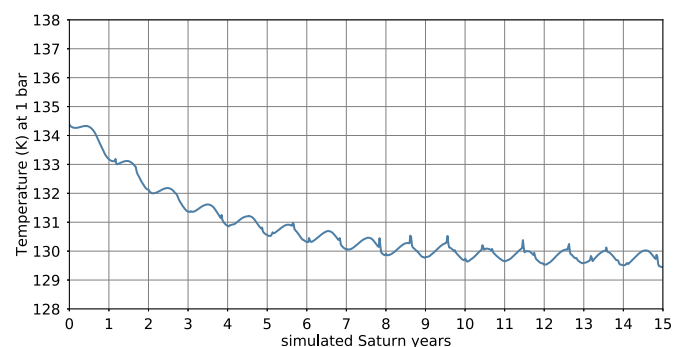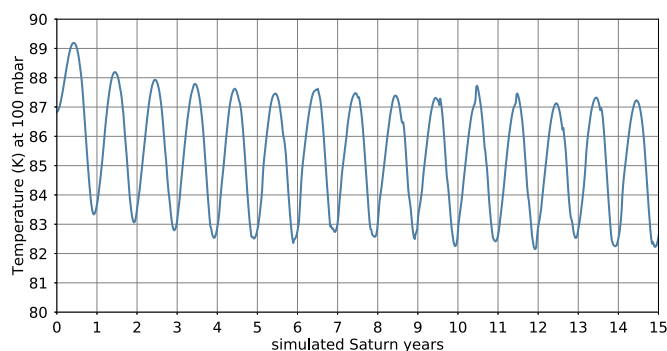The zonal jets produced by our dynamical model (discussed at

Fig. 1. Evolution over the whole 15-year duration of the reference Saturn GCM simulation of zonal-mean temperature $\bar{T}$, averaged over latitudes $\varphi = 20$–$60°$N, in the tropopause region ($p = 100$ mbar, left) and in the troposphere ($p = 1$ bar, right).
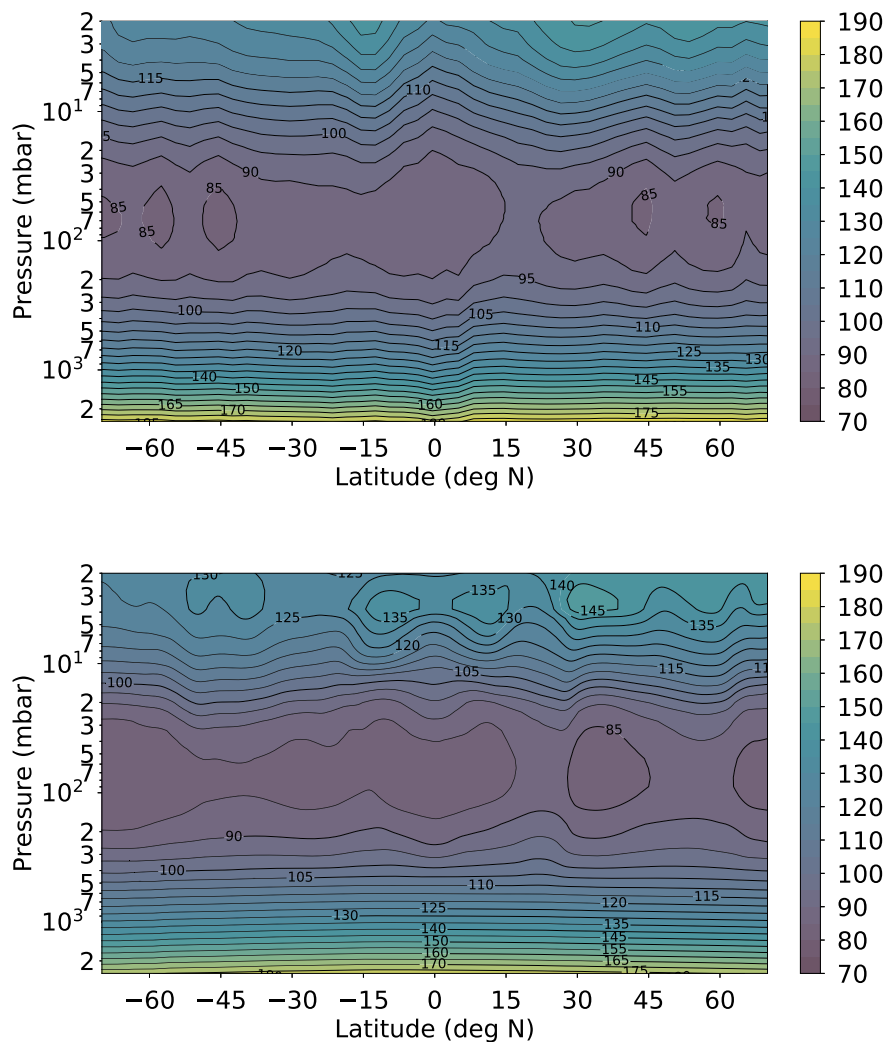
Fig. 2. Latitude-pressure section of zonal-mean temperature $\bar{T}$ (top) observed by Cassini/CIRS in 2015 (Guerlet et al., 2015a) vs. (bottom) produced by our Saturn DYNAMICO GCM in the fourteenth simulated Saturn year at $L_s \sim 70°$ (see Table 1 for a definition of L_s). The Cassini/CIRS observations shown here are nadir retrievals, with optimal sensitivity in the 500–70 mbar and 5–0.5 mbar ranges. Model results are similar should any of the simulated Saturn year starting from year eight be considered.

length in what follows) are associated with distinctive temperature signatures, i.e. localized meridional gradients of temperature (see Fig. 2 and 4), according to the thermal wind equilibrium which links $\partial \bar{u}/\partial z$ to $\partial \bar{T}/\partial y$. These thermal signatures associated with jets are of similar amplitude between modeling and observations, although the localization (i.e. latitude) of those thermal signatures is not compliant between models and observations, echoing the discrepancies in latitude between the observed and modeled jet structures (see Section 3.2).

3.2. Tropospheric and stratospheric jets

3.2.1. Mid-latitude jets

Fig. 5 is a snapshot of the steady-state zonal flow of our 1/2° Saturn DYNAMICO GCM simulation. Our model produces mid-latitude zonal jets, both eastward and westward (i.e. prograde and retrograde), which average intensities over a year reach about 45–50 m s^{-1} for westward jets and 60–65 m s^{-1} for eastward jets at the visible cloud deck (0.8–1.5 bar). Thus, the strength of mid-latitude zonal jets modeled in our Saturn DYNAMICO GCM are, to first order, consistent with the observed winds (Porco et al., 2005; García-Melendo et al., 2010) recast in the System IIIw rotating frame following Read et al. (2009b) (see their Fig. 2a). The quantitative match between our GCM and the observations is not perfect, for modeled mid-latitude jets are

underestimated by about 25% compared to observations. Although the number of mid-latitude prograde zonal jets produced in our Saturn DYNAMICO GCM is compliant with observations (2–3 per hemisphere), the latitude of occurrence of the modeled zonal jets do not exactly match the observations, where the mid-latitude jets are more closely grouped. Our GCM predictions for mid-latitude zonal jets are broadly consistent with the previously-published body of work employing Saturn GCMs (e.g., Liu and Schneider, 2010; Lian and Showman, 2010).

The Ertel potential vorticity (PV) q_θ calculated on isentropic surfaces – a conserved quantity (i.e. a flow "tracer") for adiabatic motions (Vallis, 2006) – is defined under hydrostatic approximation following Read et al. (2009a) Eq. (3).

$$q_\theta = -g \, (f + \zeta_\theta) \, \frac{\partial \theta}{\partial p} \tag{1}$$

where f and ζ_θ are defined as in Table 1, with the θ subscript denoting evaluation across a surface of uniform potential temperature θ. The meridional profile of PV associated with the tropospheric jet structure simulated by our Saturn DYNAMICO GCM is shown in Fig. 6. Characteristic PV "staircases" (i.e. sharp PV gradients) are found within the core of each mid-latitude eastward jet, surrounded by areas with "mixed PV" (i.e. uniform PV with latitude) on the flanks of the jets. The Ertel PV field obtained in Fig. 6 with our model is similar to the one
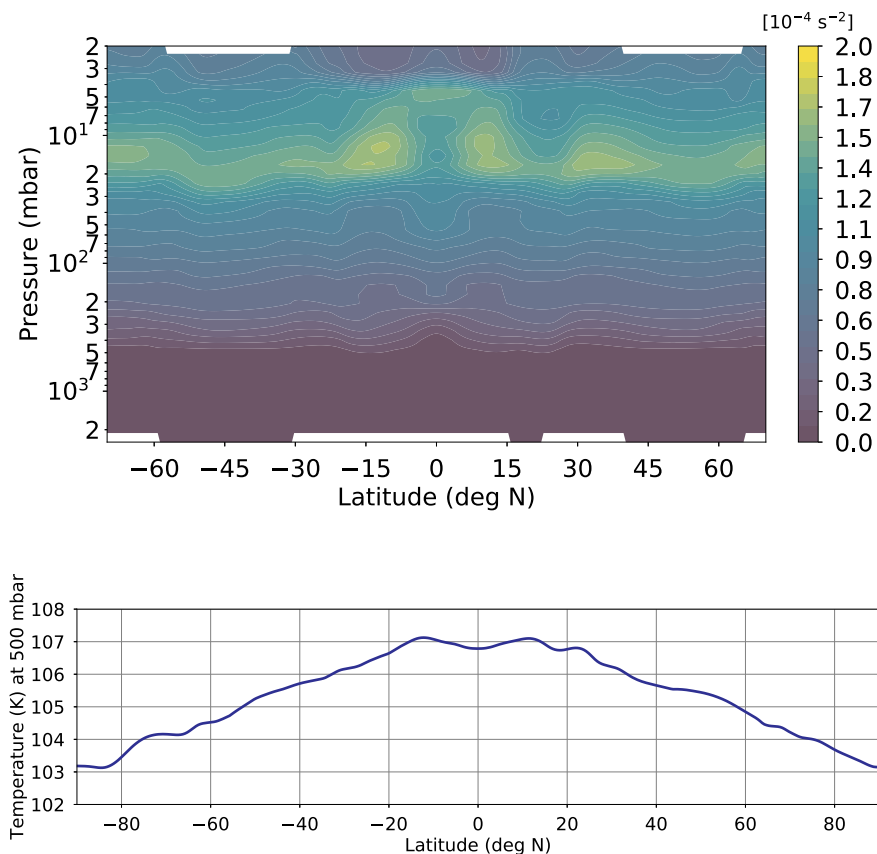
Fig. 3. (Top) Latitude-pressure section of zonal-mean Brunt-Väisälä frequency N^2 and (bottom) meridional profile of zonal-mean temperature $\bar{T}$ at 500 mbar, averaged over the fourteenth simulated Saturn year with our Saturn DYNAMICO GCM.

obtained through Cassini measurements by Read et al. (2009a). This result, reminiscent of those obtained with idealized models of rapidly-rotating flows (Dunkerton and Scott, 2008; Dritschel and Scott, 2011; Marcus and Shetty, 2011), shows that the emergence and sharpening of mid-latitude eastward jets is associated with PV mixing. This homogeneization of PV on the flanks of the jets is associated with the breaking of Rossby waves emitted at the core of the jet (e.g., Dritschel and McIntyre, 2008). This creates a convergence of eastward momentum towards the regions of wave emission, i.e. the core of the eastward jets (Vallis, 2006; Schneider and Liu, 2009; Showman and Polvani, 2011), helping to maintain the jet structure against dissipation (O'Gorman and Schneider, 2008).

The vertical structure of the zonal-mean zonal jet system simulated by our Saturn DYNAMICO GCM is displayed in Fig. 7. The mid-latitude eastward and westward jets exhibit a barotropic structure (i.e. weak vertical shear) in the deep troposphere, and a baroclinic structure (i.e. significant vertical shear) in the upper troposphere/stratosphere. The latter is in balance with the meridional temperature variations observed and modeled in the temperature structure in Fig. 4. Interestingly, eastward mid-latitude jets simulated in our Saturn DYNAMICO GCM does not weaken from the cloud level around 1 bar to the upper troposphere, as is observed (García-Melendo et al., 2010; Del Genio and Barbara, 2012); the jet intensity actually tends to slightly increase upwards from the troposphere to the stratosphere in our simulations. Using Cassini VIMS images, Studwell et al. (2018) found that the intensities of mid-latitude jets were generally increasing from the 2-bar level to the 300–500 hPa level, which tends to confirm our Saturn DYNAMICO GCM results at and below the cloud level.

Accounting for the preferential zonal wavenumber $n = 6$ (hexagonal) mode in the circumpolar jet structure on Saturn is still an open question (Morales-Juberías et al., 2011, 2015), given the narrow

parameter space which allows for this mode to predominate over other modes (Barbosa Aguiar et al., 2010; Rostami et al., 2017). The polar jet in our Saturn DYNAMICO GCM simulation (Figs. 5 and 12) has a different morphology than the other mid-latitudes jets, exhibiting meandering with time, which cause it to undergo latitudinal deformation and temporal variability. However, the meandering of our simulated polar jet is intense and very variable with time, with neither a $n = 6$ nor any mode n predominance. This is clearly at odds with the observed stable slowly-moving hexagonal jet in Saturn's northern polar regions (Sánchez-Lavega et al., 2014; Antuñano et al., 2015). The polar jet's zonal wind speed, latitudinal position and width are, however, key factors to account for Saturn's northern polar hexagon (Morales-Juberías et al., 2011). The polar jet simulated by our Saturn GCM is both too weak and too equatorward (as in Fig. 5) to possibly lead to a predominance of the $n = 6$ mode. Furthermore, the polar jet's temporal evolution influenced by poleward migration causes it to break under intensified meandering by barotropic and baroclinic instability (see Section 4). This obviously prevents any high-latitude jet to settle as a stable, wavenumber-6 hexagon-shaped, structure. Either the baroclinicity in the polar regions is not realistic enough in our Saturn DYNAMICO GCM (this influence of vertical shear is discussed in Morales-Juberías et al., 2015); and/or the central polar vortex is insufficiently resolved in our simulations, hence too weak to stabilize the hexagonal shape of the polar jet against meandering (the influence of the central polar vortex is discussed in Rostami et al., 2017).

3.2.2. Equatorial jets

A prograde equatorial jet is produced in the troposphere by our 1/2° Saturn GCM simulation. It is, however, severely underestimated by one order of magnitude compared to the observed value by Cassini (∼ 350–400 m s^{-1} in System IIIw, Read et al., 2009b; García-Melendo
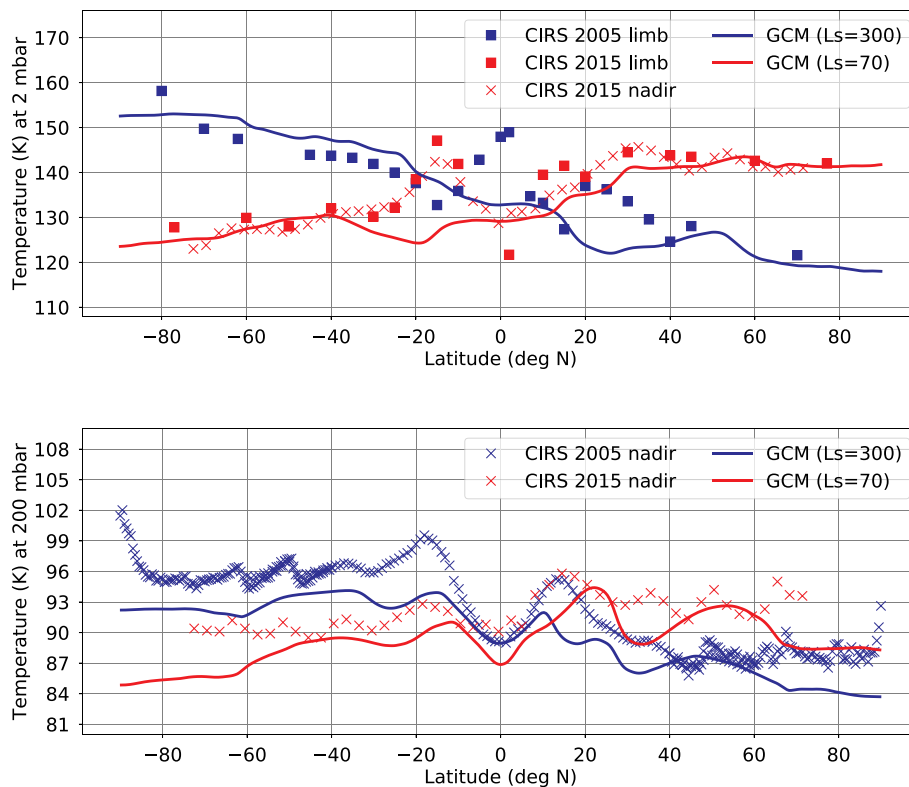
Fig. 4. Meridional profiles of zonal-mean temperature $\bar{T}$ at the two opposite solstices explored by the Cassini spacecraft (blue: year 2005, $L_s = 300°$; red: year 2015, $L_s = 70°$). Squares correspond to Cassini/CIRS limb retrievals (Guerlet et al., 2009 ; Guerlet et al., 2015a), crosses correspond to Cassini/CIRS nadir retrievals (Fletcher et al., 2007; Guerlet et al., 2015a) , lines correspond to Saturn DYNAMICO GCM simulations (fourteenth simulated year). Middle stratospheric conditions (2 mbar) are shown in the top plot, where both CIRS limb and nadir retrievals are valid; upper tropospheric conditions (200 mbar) are shown in the bottom plot, where CIRS nadir retrievals are valid. Model results are similar should any of the simulated Saturn year starting from year eight be considered. (For interpretation of the references to color in this figure legend, the reader is referred to the web version of this article.)

et al., 2010). The local super-rotation index s associated with this equatorial jet writes (e.g., Read and Lebonnois, 2018)

$$s = \frac{\mu^m + \mu^w}{\mu^m_{\varphi=0}} - 1 = \frac{a \cos\varphi \ (\Omega \ a \cos\varphi + \bar{u})}{\Omega \ a^2} - 1 \tag{2}$$

The equatorial zonal jet simulated by our GCM is only weakly super-rotating ($s \sim 0.3\%$) in a very limited area across the equator ($\varphi = \pm 3°$), while the observed superrotating index is an order of magnitude larger (Read and Lebonnois, 2018, their Table 1) and the observed equatorial jet extends towards latitudes $\pm$ 15–20°.

The prograde, eastward, equatorial jet in the Saturn DYNAMICO GCM arises from acceleration caused by convergence of eddy momentum towards the equator (see Eq. (13) in Section 4). Fig. 8 shows that, within the equatorial super-rotating jet, the eddy momentum transport $\overline{u'v'}$ is positive south of the equator and negative north of the equator, meaning that waves and eddies cause a convergence of eastward momentum at the equator. Yet this equatorial acceleration by waves and eddies is probably underestimated by our Saturn DYNAM-ICO GCM, given the resulting modeled jet being ten times less strong than the observed equatorial jet (García-Melendo et al., 2010). This is consistent with the latitudinal profile of Ertel PV shown in Fig. 6, where PV mixing by Rossby waves in equatorial regions appears not sufficient to yield a truly PV-mixed area, as is the case for mid-latitude jets.

Based on the existing literature (e.g., Gierasch et al., 2000; Lian and Showman, 2010), a possible source of this underestimate of Saturn's equatorial superrotation could be the lack of a parameterization for moist convection in our model (see, e.g., the work on Jupiter by Zuchowski et al., 2009; Young et al., 2019b). Our GCM results are actually in contrast with the simulations by Liu and Schneider (2010)

which did not include an additional (moist) convective source, apart from the combination of internal heat flux and convective adjustment. The fact that the convective adjustment scheme in Liu and Schneider (2010) has a non-zero relaxation time (cf. Schneider and Liu, 2009, Appendix B, section d), while ours is instantaneously adjusting, might be an element of explanation for this discrepancy. Using a non-zero relaxation time might emulate the convective overturning time of dry and moist convective structures, confirming the need to add, in our Saturn DYNAMICO GCM, a (dry and moist) convective parameterization more sophisticated than our simple convective adjustment scheme (e.g. thermal plume modeling like Hourdin et al., 2002; Rio and Hourdin, 2008; Colaïtis et al., 2013) that will better represent the local dynamics underlying convective mixing and the impact thereof on the generation of waves and eddies.

While the strengths of mid-latitude jets increase with altitude in our Saturn DYNAMICO GCM simulations (see Section 3.2.1), the intensity of the simulated equatorial jet decreases with altitude, which is also in line with the Cassini observations reported in Studwell et al. (2018). Although a quantitative comparison with observations is prevented by the severely underestimated equatorial wind speed in our GCM, the fact that the equatorial jet decays from the cloud level to the tropopause is also observed by Flasar et al. (2005), Li et al. (2008), and Sánchez-Lavega et al. (2016). Fig. 8 indicates that this decay is caused in our Saturn DYNAMICO GCM by divergence of eastward eddy momentum at the tropopause, in contrast to the convergence of eastward eddy momentum causing the super-rotating jet in the troposphere. Interestingly, to interpret the Cassini VIMS observations of tracers, Fletcher et al. (2011a) proposed that two stacked, reversed cells are present in Saturn's troposphere, one resulting from "jet damping" in the upper troposphere and one resulting from "jet pumping" in the mid-troposphere
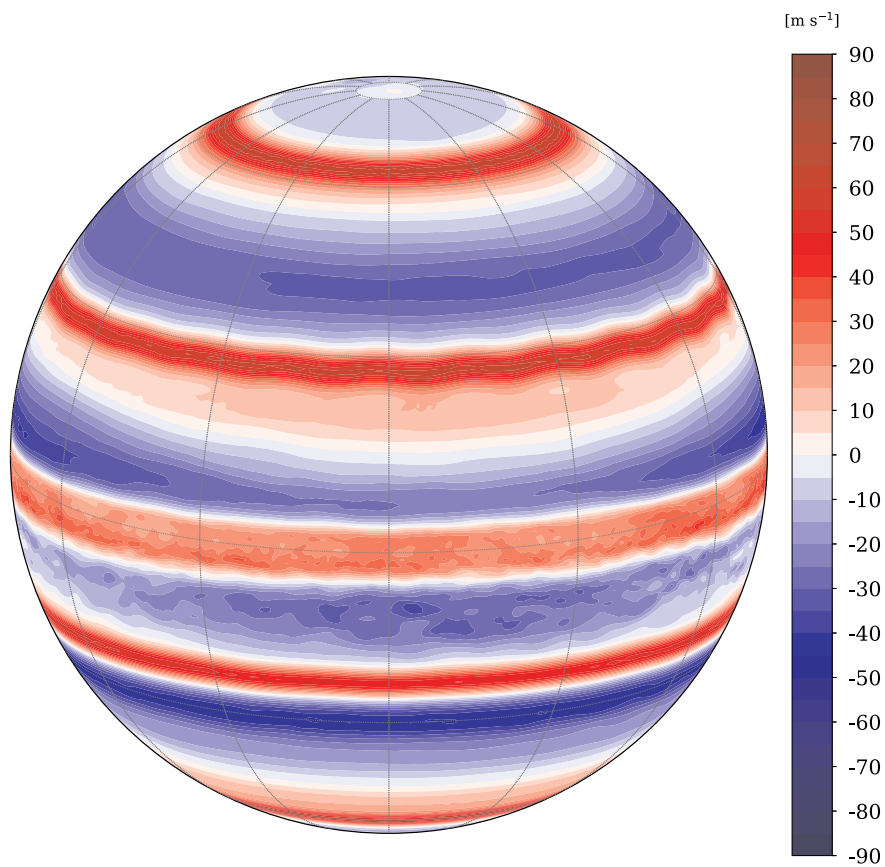
Fig. 5. Instantaneous zonal wind u in the beginning ($L_s \sim 0°$) of the twelfth simulated year (after 270 thousands simulated Saturn days), on the fifth sigma level of the model (pressure level $\sim$ 1.5 bar, corresponding to Saturn's visible cloud deck and tropospheric conditions).
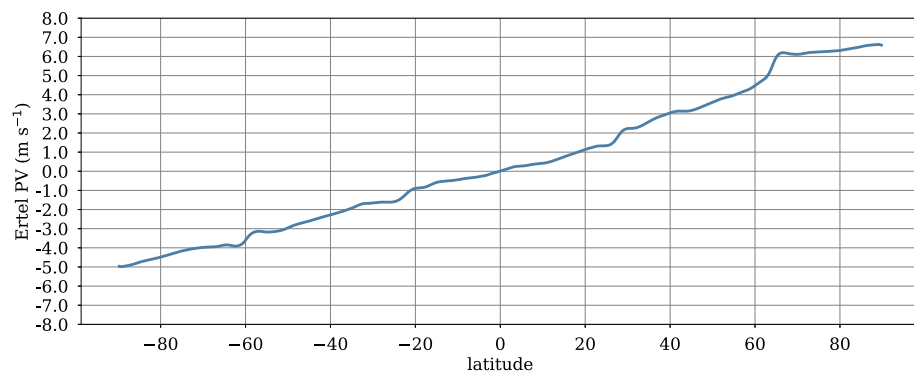

Fig. 6. Instantaneous zonal-mean Ertel potential vorticity (top) and zonal wind (bottom) projected on a surface of equal potential temperature 205 K, corresponding to tropospheric conditions. The time adopted for this plot is similar to Fig. 5. The 205 K value of potential temperature corresponds to upper tropospheric conditions, higher in altitude than Fig. 5; lower tropospheric conditions are not accessible through this diagnostic due to the difficulty of defining the Ertel potential vorticity on isentropes in neutral conditions ($N^2 \sim 0$). Our Python code used to calculate potential vorticity contains excerpts from the code by Barlow (2017) .
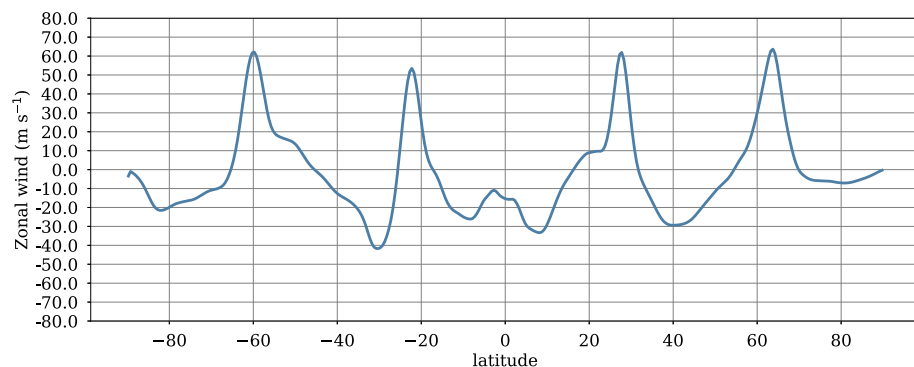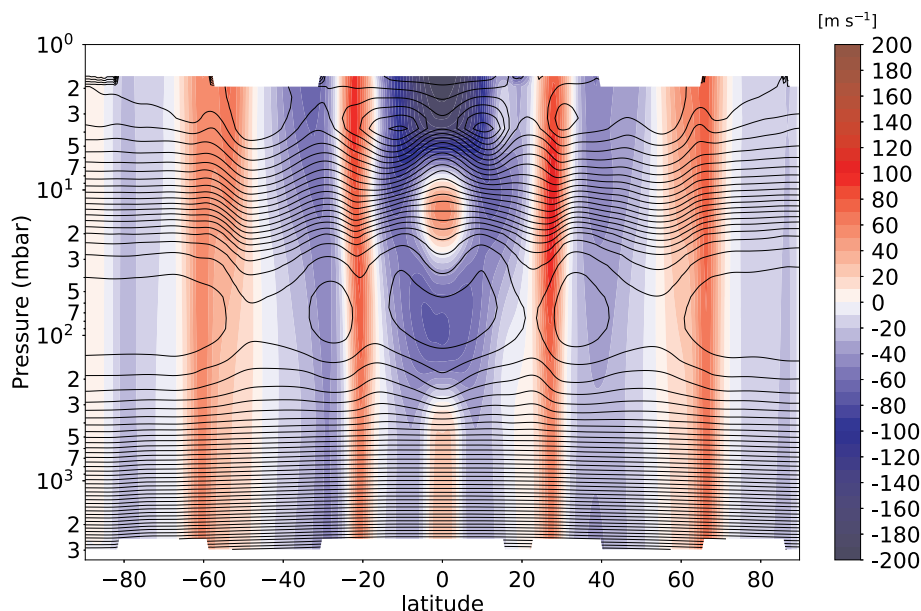
Fig. 7. Instantaneous latitude-pressure cross-section of zonal-mean zonal wind $\bar{u}$ (colors) and zonal-mean temperature $\bar{T}$ (contours) in the beginning ($L_s \sim 0°$) of the fifteenth simulated year (after about 342 thousands simulated Saturn days). Model results are similar should any of the simulated Saturn year starting from year eight be considered.
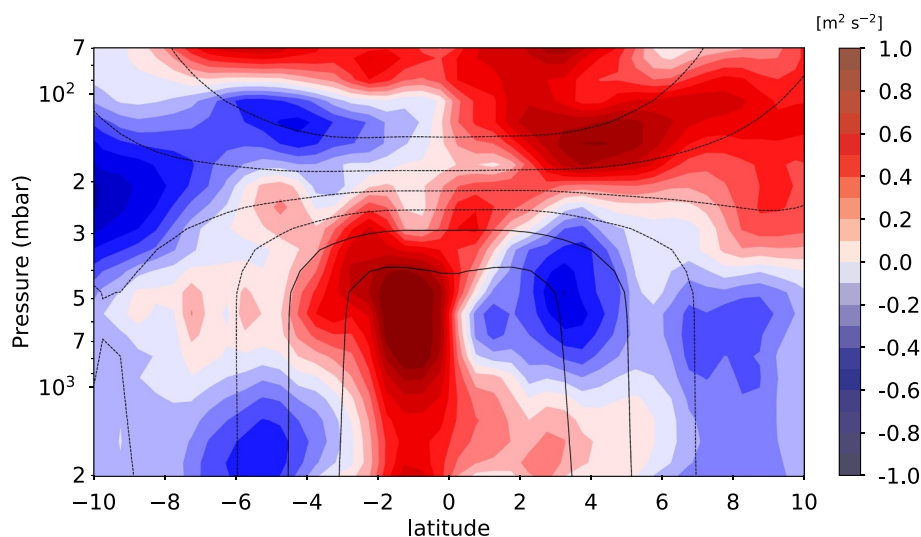

Fig. 8. Latitude-pressure cross-section of zonal-mean eddy momentum transport $u'v'$ (colors) and zonal wind $\bar{u}$ (contours) averaged over the whole 15-year duration of the reference simulation. This temporal averaging is carried out because, contrary to other jets, the equatorial jet does not migrate with time and the equatorial eddies develop continuously rather than through "bursts" (see Fig. 13 in Section 4).

(their section 6). This is compliant with Fig. 8 showing in equatorial regions an area of eddy divergence/westward jet sitting on top of an area of eddy convergence/eastward jet.

Saturn's equatorial stratosphere exhibits a downward propagation of (supposedly zonally-symmetric) alternating positive and negative temperature perturbations with respect to the radiative-equilibrium temperature field (Fouchet et al., 2008; Guerlet et al., 2011; Li et al., 2011; Fletcher et al., 2017; Guerlet et al., 2018). Those temperature signatures are thought to be associated with eastward and westward jets alternating along the vertical, similarly to the Earth's Quasi-Biennal Oscillation (Baldwin et al., 2001). The typical period of this equatorial stratospheric oscillation is 15 Earth years, half a Saturn year (Orton et al., 2008). Modeling could help to identify the mechanisms responsible for Saturn's equatorial oscillation, putatively the interaction of planetary-scale and small-scale waves with the mean zonal flow as it

is the case of the terrestrial Quasi-Biennal Oscillation (Baldwin et al., 2001).

In Fig. 7, above the eastward equatorial tropospheric jet, we note the presence in our reference simulation of stacked, alternatively eastward and westward, stratospheric jets. An eastward jet is centered at pressure level 15 mbar in the latitudinal range − 5°→ 5°N, surrounded above and below by westward jets. This structure is reminiscent of the stacked jet signature derived through thermal wind balance from Cassini observations of equatorial oscillation of temperature (e.g., Guerlet et al., 2018). Yet, contrary to Cassini observations, no downward propagation of this jet signature is reproduced by our Saturn DYNAMICO GCM between northern summer and fall (Fig. 9).

Section 3.3.1 features a discussion of the equatorial waves being most probably responsible for the stacked jet structure in the
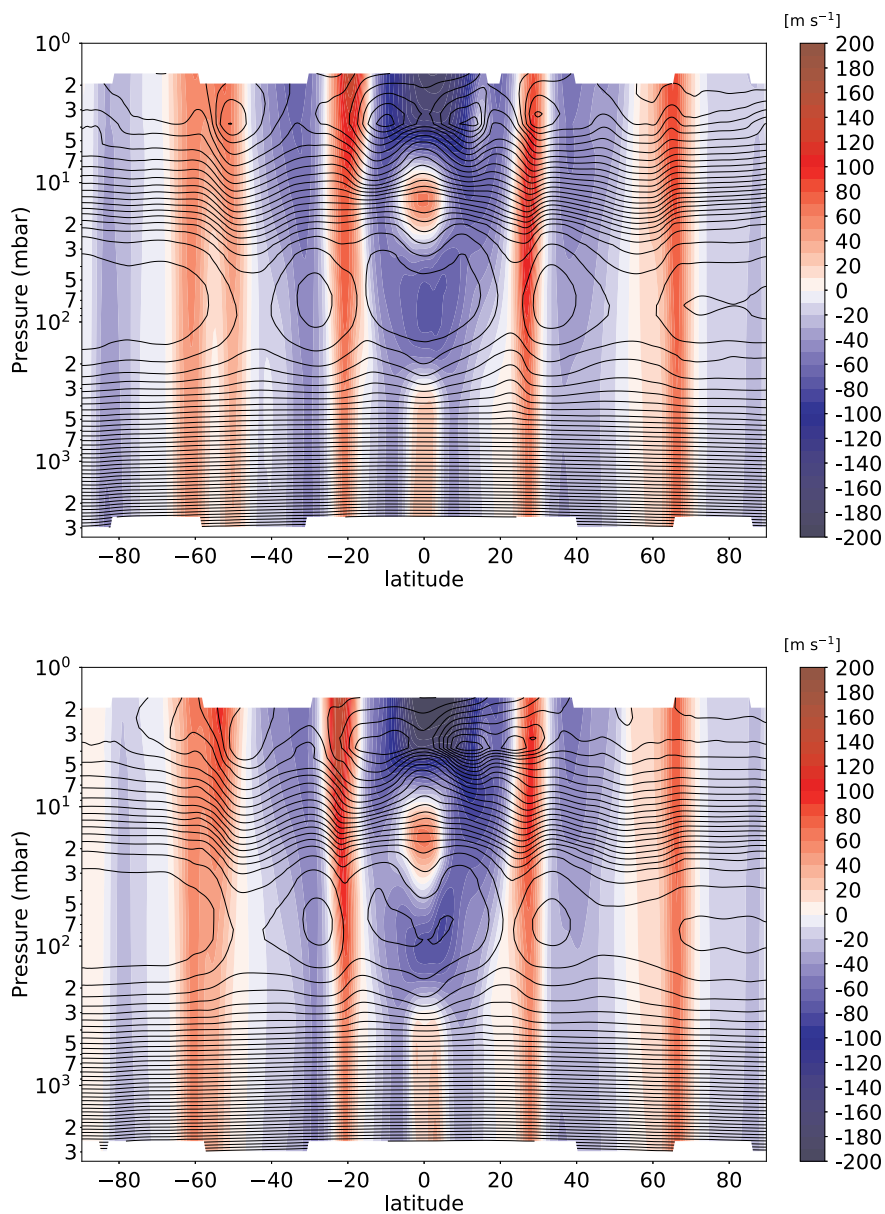
Fig. 9. Same as Fig. 7 for northern summer solstice ($L_s \sim 90°$, top panel) and fall equinox ($L_s \sim 180°$, bottom panel).
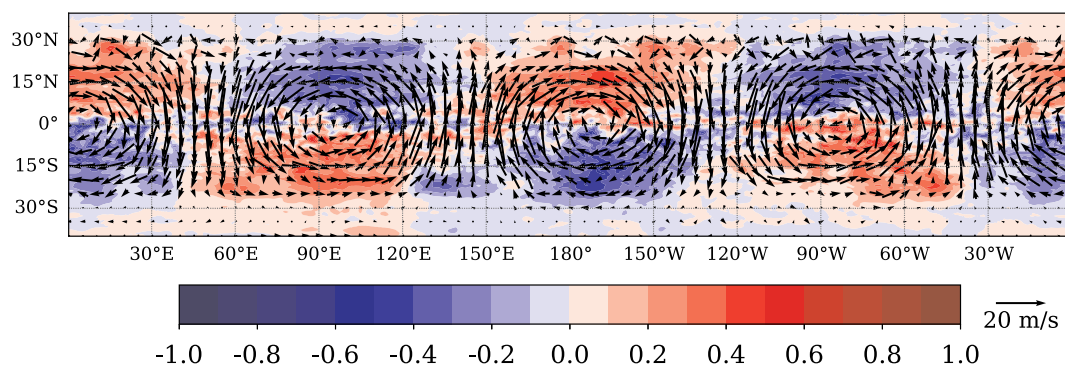

Fig. 10. Instantaneous view on the zonal perturbations of temperature T' (shaded contours) and horizontal winds $[u', v']$ (wind vectors) in the beginning ($L_s \sim 0°$) of the twelfth simulated year (after 270 thousands simulated Saturn days), on the fifteenth sigma level of the model (pressure level ~ 130 mbar, corresponding to Saturn's tropopause, transition between troposphere and stratosphere). Only latitudes below 40°N/S are shown (tropical channel). A similar figure is obtained at Saturn's cloud level (~ 1.5 bar, as in Fig. 5), with an even stronger prominence of the wavenumber-2 signal.
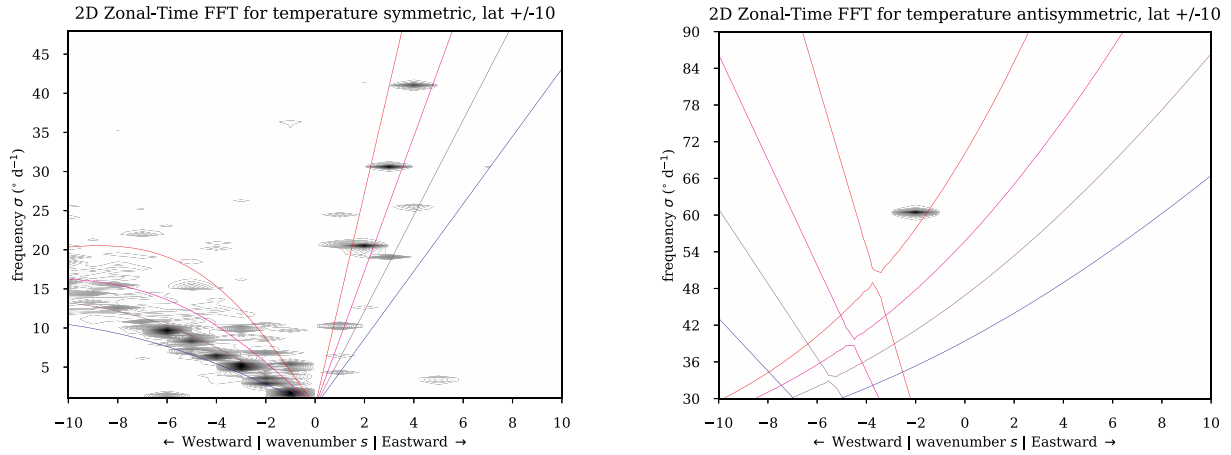
Fig. 11. Spectral analysis of the equatorial waves produced in our Saturn DYNAMICO GCM (in dynamical steady-state) at the same vertical level as Fig. 10. This spectral power mapping is obtained by a two-dimensional Fourier transform from the longitude λ/time t space to the zonal wavenumber s/frequency σ space (Wheeler and Kiladis, 1999) of the symmetric component of temperature T_S about the equator (left, see Eq. (3)) and antisymmetric component of temperature $T_{\mathcal{A}}$ about the equator (right). We follow the common assumption of a positive sign convention for frequency σ, meaning that $s > 0$ modes are eastward-propagating and $s < 0$ modes are westward-propagating. The dispersion relation for equatorial waves (Eq. (4)) is superimposed for meridional mode number $\nu = -1, +1$ (left panel, Rossby waves on the $s < 0$ side and Kelvin waves on the $s > 0$ side) and meridional mode number $\nu = 0$ (right panel, Yanai waves on the part of the curves increasing with s). Four values of equivalent depths (Eq. (5)) are included: $h = 5\,\mathrm{km}$ (blue), $h = 10\,\mathrm{km}$ (purple), $h = 20\,\mathrm{km}$ (magenta), $h = 50\,\mathrm{km}$ (red). (For interpretation of the references to color in this figure legend, the reader is referred to the web version of this article.)

stratosphere, and possible explanations for the lack of vertical propagation of the structure. A key point, not related to the wave analysis, that shall be emphasized here is that the model top is too low (at 1 mbar), and the vertical resolution of the model in the stratosphere is too coarse, to correctly study the observed equatorial oscillations. For instance, the equatorial westward jet above 10 mbar is compliant with the thermal wind field derived by Fouchet et al. (2008), but our too-low model top prevents us from discussing the bulk of the observed oscillation above the 10-mbar pressure level.

3.3. Waves and vortices

3.3.1. Equatorial waves

A close examination of the tropical structure of zonal wind in Fig. 5 hints at planetary wave activity — notably a prominent wavenumber-2 signal. This is confirmed by Fig. 10 in which the eddy (non-axisymmetric) components T', u', v' are shown in the equatorial region at the tropopause level. The prominent wavenumber-2 signal features zonal wind and temperature perturbations (about 0.5 K) which are antisymmetric about the equator, while meridional wind perturbations are symmetric about the equator. The pattern shown in Fig. 10 is strongly reminiscent of an equatorial Yanai wave (also named mixed Rossby-gravity wave, Kiladis et al., 2009, their Fig. 3) , although an interpretation as an eastward inertio-gravity wave is also possible at this stage of the analysis.

To further characterize the wavenumber-2 signal, and offer a more complete wave analysis (Fig. 10 hints at other signals being present besides the prominent wavenumber-2 signal), we follow the method of Wheeler and Kiladis (1999) commonly employed to study equatorial waves in the terrestrial tropical atmosphere (Kiladis et al., 2009; Maury and Lott, 2014). We perform a two-dimensional Fourier transform, from the longitude λ/time t space to the zonal wavenumber s/frequency σ space, of the symmetric (T_S) and antisymmetric ($T_{\mathcal{A}}$) components of the temperature field about the equator

$$T_S = \frac{1}{2}(T_{10°N} + T_{10°S}) \quad T_{\mathcal{A}} = \frac{1}{2}(T_{10°N} - T_{10°S}) \tag{3}$$

(similar computations are also performed for zonal wind u and meridional wind v). Our code uses the Fast Fourier Transform package included in the *scipy* Python library. We validated independently our

spectral analysis code on well-defined (semi-)diurnal tides and Kelvin waves simulated in the Martian atmosphere (Wilson and Hamilton, 1996; Lewis and Barker, 2005; Guzewich et al., 2016).

We perform the Fourier analysis on a specific 1000-day-long 1/2° Saturn DYNAMICO GCM run with frequent (daily) output, restarted from the GCM state after 270 thousands simulated Saturn days (about 11 simulated Saturn years). The spectral mapping in the (s, σ) space enables to evidence Rossby and Kelvin waves in the symmetric component T_S and Yanai waves in the antisymmetric component $T_{\mathcal{A}}$ (the former waves can also be detected in u_S and the latter waves in $u_{\mathcal{A}}$ and v_S, see Kiladis et al., 2009; Wheeler and Kiladis, 1999). Results for the temperature field simulated at the tropopause are shown in Fig. 11, along with the dispersion relation for equatorial waves (Maury and Lott, 2014)

$$\sqrt{\gamma}\,(2\,\nu + 1) = \gamma\,\sigma^2 - s^2 - s/\sigma \qquad \gamma = \frac{4\,a^2\,\Omega^2}{g\,h} \tag{4}$$

where ν is the meridional mode number and defines the considered wave (Rossby: $\nu = +1, +2, \ldots$ Yanai: $\nu = 0$, Kelvin: $\nu = -1, -2, \ldots$), γ is named the Lamb parameter, and h is an equivalent depth associated with the vertical wavenumber m

$$m^2 = \frac{N^2}{g\,h} - \frac{1}{4\,H^2} \tag{5}$$

Dominant modes in the symmetric and antisymmetric components of the temperature and wind fields are detailed in Table 2.

The spectral analysis shows that (consistently in the three analyzed fields) the prominent wavenumber-2 signal is a westward-propagating Yanai wave with a period 6 days (frequency 60° longitude per day). Our analysis also evidences, both in the temperature and zonal wind fields, westward-propagating Rossby waves with wavenumbers $s = -2$ to $s = -6$, exhibiting long periods of hundreds Saturn days and frequencies of a couple degrees longitude per day (the wavenumber-$s = -1$ cannot be evidenced unambiguously since its intrinsic phase speed is too close to zero). The longer-period Rossby waves are modulating the temperature variability caused by the wavenumber-2 Yanai wave with a shorter 6-day period. The temperature field also features eastward-propagating Kelvin waves with wavenumbers $s = +2, +3, +4$, periods 10–20 Saturn days, and frequencies a couple tens of degrees longitude per day; the Kelvin wave signal is much fainter in the
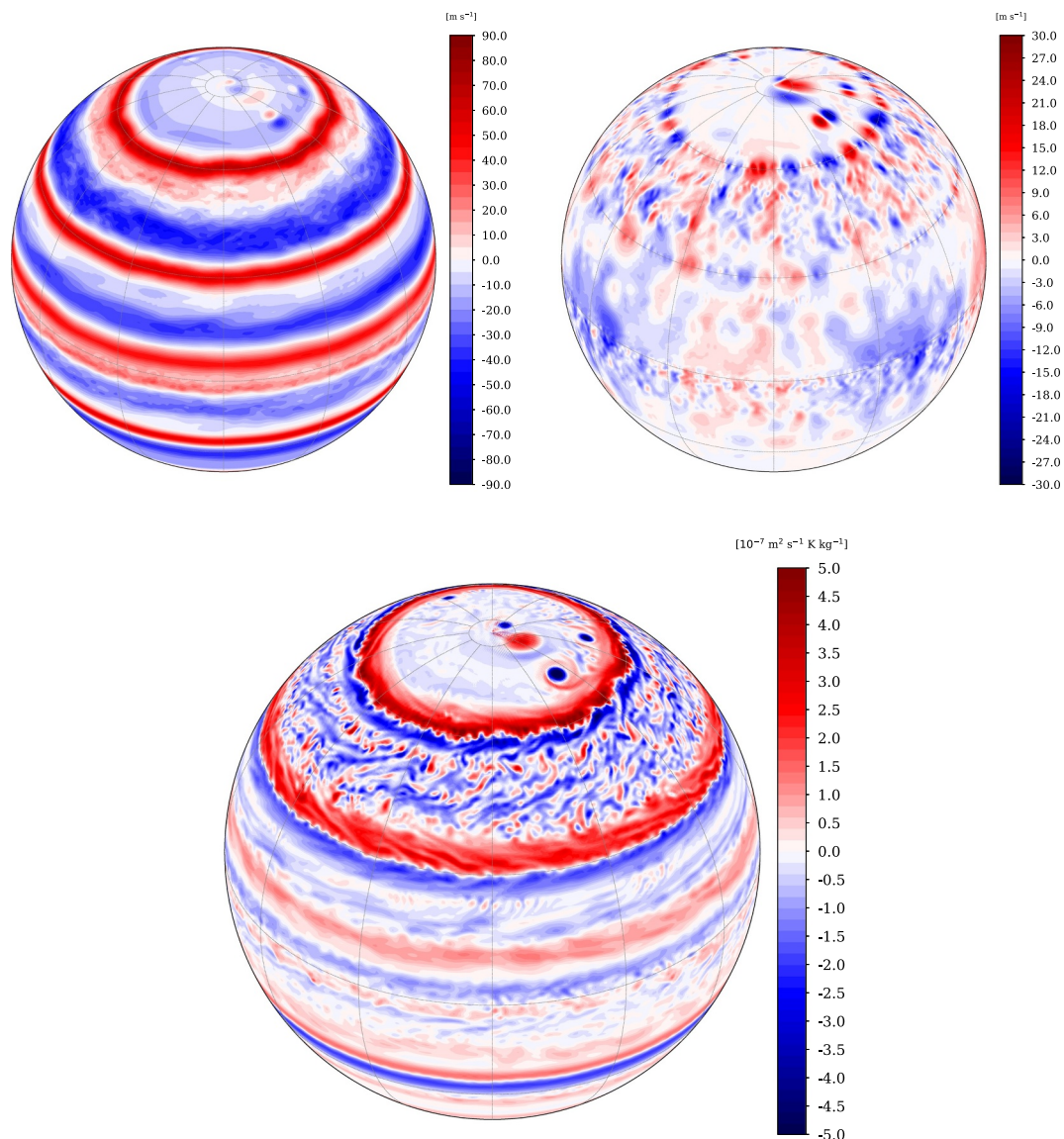
Fig. 12. Instantaneous view on (top left panel) the zonal wind u and (top right panel) the meridional wind v on the fifth sigma level of the model (pressure level ~ 1.5 bar), as in Fig. 5 and (bottom panel) relative Ertel potential vorticity (PV) on tropospheric isentrope $\theta = 205$ K after 171 thousands simulated Saturn days (beginning of the seventh simulated year). Ertel PV computations are described in Eq. (1) and Section 3.2.1.

zonal wind component. This Kelvin wave signal is absent from the temperature field lower in the troposphere, at the cloud level.

Elaborating from Voyager observations, Achterberg and Flasar (1996) detected a Rossby wavenumber-2 signal in the tropics and mid-latitudes of Saturn's tropopause (130 mbar), confined by vertical variations of static stability. A similar signal is present in our Saturn GCM DYNAMICO simulations: 1 degree longitude per day corresponds to ~ $26.3\,\mathrm{m\,s^{-1}}$, hence the simulated Rossby wavenumber-2 signal has a phase speed of ~$37–92\,\mathrm{m\,s^{-1}}$, which is compatible with the phase speed of the order $100\,\mathrm{m\,s^{-1}}$ discussed by Achterberg and Flasar (1996). Our Saturn DYNAMICO GCM results indicate that other tropical Rossby modes (wavenumbers 3, 4, 5, …) are likely to be significant within Saturn's tropics. This is compliant with the recent analysis by Guerlet et al. (2018), based on Cassini CIRS observations, which shows a complex structure at a pressure level of 150 mbar; interestingly, what appears as a wavenumber-3 Rossby mode dominate in the upper stratosphere (0.5 to 5 mbar), possibly indicating conditions for breaking at this level or below for the other modes. Unless the wavenumber-2 signal found by Achterberg and Flasar (1996) is actually eastward-propagating at phase speeds about $1600\,\mathrm{m\,s^{-1}}$ (the fast planetary

modes were discarded by this study in favor of slower, more plausible, Rossby modes), the prominent wavenumber-2 westward-propagating Yanai wave in our Saturn DYNAMICO GCM simulation remains to be evidenced in observations. A westward-propagating wavenumber-9 Yanai wave mode has been, however, detected by Cassini CIRS in the upper stratosphere (1 mbar) by Li et al. (2008), but their observed temperature signature being symmetric about the equator (with a maximum at the equator) would be more compliant with a westward inertia-gravity wave (Guerlet et al., 2018).

The presence of equatorial vertically-propagating eastward Kelvin waves and westward Rossby and Yanai waves in our Saturn DYNAMICO GCM simulations at the 130-mbar level means that both eastward and westward momentum is transferred in the stratosphere where vertically-stacked westward/eastward jets are found (Fig. 7 and Section 3.2.2). This "stacked jets" equatorial signature is similar to the jet structure putatively associated with the equatorial oscillation of temperature (Fouchet et al., 2008; Guerlet et al., 2011). Nevertheless, our model does not reproduce the downward propagation of the observed equatorial oscillation in Saturn's stratosphere (Guerlet et al., 2018), also obtained by idealized simulations (Showman et al., 2018b).

Table 2
Spectral modes detected by Fourier analysis and depicted in Fig. 11. The spectral mapping for wind components is not shown, as it is similar to the spectral mapping for temperature shown in Fig. 11. *SP* stands for spectral power, d for Saturn days. The frequencies and periods are intrinsic, i.e. with respect to a frame fixed on the zonally-averaged zonal flow $\bar{u} \sim -40 m/s$ at latitudes 10°N/S.

s	σ (°/d)	Period (d)	log(SP)
Dominant modes in T_S			
+2	22.0	16.3	7.9
+3	32.1	11.2	7.6
−3	3.5	102.0	7.5
−6	8.2	43.8	7.4
−4	5.0	72.4	7.3
−2	1.4	262.7	7.3
−5	6.8	53.2	7.2
+4	42.5	8.5	7.2
Dominant modes in u_S			
−6	8.2	43.8	9.8
−2	3.5	102.0	9.7
−3	3.2	113.6	9.6
−4	4.3	84.7	9.6
−5	5.3	67.5	9.4
−7	8.9	40.3	9.4
+2	22.0	16.3	9.3
Dominant modes in $T_{\mathcal{A}}, u_{\mathcal{A}}, v_S$			
−2	59.0	6.1	10.1

Furthermore, the modeled temperature contrasts between the equator and latitudes ± 15° associated with the stacked jets (∼ ± 5–10 K, figure not shown) are much lower than the contrasts obtained by Cassini thermal infrared measurements (± 15–20 K, Fouchet et al., 2008; Guerlet et al., 2018) . Those discrepancies with observations are probably related to a weak transfer of momentum to the mean flow by the resolved waves in our model:

(a) while our spectral analysis reveals a Kelvin-wave signal at the tropopause, moist convection in the deep troposphere of Saturn, not accounted for in the current version of our model, could cause convectively-coupled Kelvin Waves, which are an important component to explain the Quasi-Biennal Oscillation on Earth (Kiladis et al., 2009);
(b) mesoscale (inertia-)gravity waves are not resolved by our model and are known to contribute to the momentum flux responsible for equatorial oscillations on Earth (Lindzen and Holton, 1968; Lott and Guez, 2013; Maury and Lott, 2014) and this possibility has also been explored in Jupiter's stratosphere (Cosentino et al., 2017);
(c) the absence of a strong equatorial super-rotating jet in our simulations means that the vertical propagation (and possible filtering) of equatorial waves towards the stratosphere is different between our simulations and the actual Saturn's atmosphere.

According to terrestrial modeling studies (e.g. Takahashi, 1996; Nissen et al., 2000; Watanabe et al., 2008; Lott et al., 2014), our modeling setting is ultimately lacking two key elements to reproduce Saturn's equatorial oscillation: the model top must be raised to cover the stratospheric levels (0.01–10 mbar) where the stratospheric oscillation is observed, and the vertical resolution must be refined in the stratosphere. Those improvements, related to Challenge $\mathcal{C}_3$, are deferred to a dedicated future study of Saturn's stratospheric circulations using our Saturn DYNAMICO GCM (Bardet D. et al., Part IV in preparation).

3.3.2. Extratropical eddies

Our reference simulation with the Saturn DYNAMICO GCM exhibits a variety of extratropical eddies, as is evidenced in Fig. 12.

The simulated tropospheric fields in Fig. 12 indicate that the mid-latitude eastward jets at latitude 30°N and 60°N are prone to meandering

caused by high-wavenumber waves. Those waves are found at the center of the eastward jets, featuring a strong inversion of the meridional gradient of potential vorticity (Rayleigh-Kuo necessary condition for barotropic instability, see Section 4.4). A spectral analysis on a 2000-day sample of the temperature and wind fields, performed similarly to the analysis in Section 3.3.1 (except for a Doppler-shift correction considering the ambient eastward zonal jet $\bar{u} = 60 \text{ m s}^{-1}$) indicates that the 30°N perturbations correspond to a westward-propagating wavenumber-19 Rossby wave with a period of 435 days (frequency 0.8° longitude per day, i.e. about 23 m s^{-1}). The characteristics of this wave (wavenumber, phase speed, and occurrence at the center of a mid-latitude eastward jet) are very similar to the idealized modeling results obtained by Sayanagi et al. (2010) to explain the "Ribbon wave", a Rossby wave propagating in the extratropical latitudes of Saturn as a result of barotropic and baroclinic instability (Godfrey and Moore, 1986; Sanchez-Lavega, 2002; Gunnarson et al., 2018). Furthermore, the meandering phase speed and wavenumber reproduced by our Saturn DYNAMICO GCM in the 30°N eastward jet are compliant with the slow ribbon waves identified by Gunnarson et al. (2018) with Cassini imaging (their Fig. 3d).

It is worthy of notice that our Saturn DYNAMICO GCM simulations exhibit a chain of about ten cyclonic vortices with an horizontal extent of a couple thousand kilometers (the successive red spots of positive vorticity in Fig. 12 bottom) in the equatorward (southern) edge of the 30°N eastward jet. This signature shares the characteristics of the "String of Pearls" observed by Cassini through infrared mapping (Sayanagi et al., 2014). Nevertheless, the simulated vortices are more short-lived (typically a ten-day duration) than the observed cyclonic vortices, so the analogy between the modeled structures and the "String of Pearls" is not complete.

The most distinctive and large-scale vortices are found in polar regions in our Saturn DYNAMICO GCM simulations. Fig. 12 demonstrates a clear and sharp transition between the mid-latitudes where the vorticity field is dominated by eddies, and the polar regions where the vorticity field is dominated by large-scale vortices. This is somewhat compliant with the picture drawn by observations, where no vortex activity was observed in mid-latitudes before the appearance of the 2010 giant storm (Trammell et al., 2016). Both anticyclones and cyclones are produced in our model: the excerpt shown in Fig. 12 comprises four anticyclones and one larger cyclone. Those simulated large-scale vortices exhibit a strong temporal variability, with merging phenomenon combined with beta-drift effect (poleward for anti-cyclones, see Sayanagi et al., 2013), which causes their typical duration to be no more than several hundreds Saturn days. The picture drawn by Fig. 12 is typical of most of our Saturn DYNAMICO GCM simulation: anticyclones appear favored against cyclones, which is in agreement with the putative longer stability of anticyclones compared to cyclones, but at odds with the statistics derived from Cassini imagery over seven Earth years by Trammell et al. (2016). A more in-depth analysis of the large-scale vortices is out of the scope of this paper; furthermore, accounting for moist convection and the associated release of latent heat appears to be a crucial addition to carry out this analysis (O'Neill et al., 2015).

The last class of eddies are the remainder of non-axisymmetric disturbances that are neither waves nor vortices. Such "non-organized" eddies can be seen in Fig. 12 between latitudes 30°N and 60°N. Their activity can strongly vary with time: Fig. 12 shows a case with a "burst" of eddy activity at those latitudes, while the eddy activity can be close to none at other times in the simulation (Fig. 5). The presence of intermittent bursts of eddy activity is reminiscent of the results of Panetta (1993) and is further discussed in Section 4.1.

4. Evolution of the tropospheric jet structure

4.1. Jets and eddies in the 15-year simulation

The evolution of tropospheric jets with time in the 15-year duration of our reference 1/2° Saturn DYNAMICO simulation is summarized in
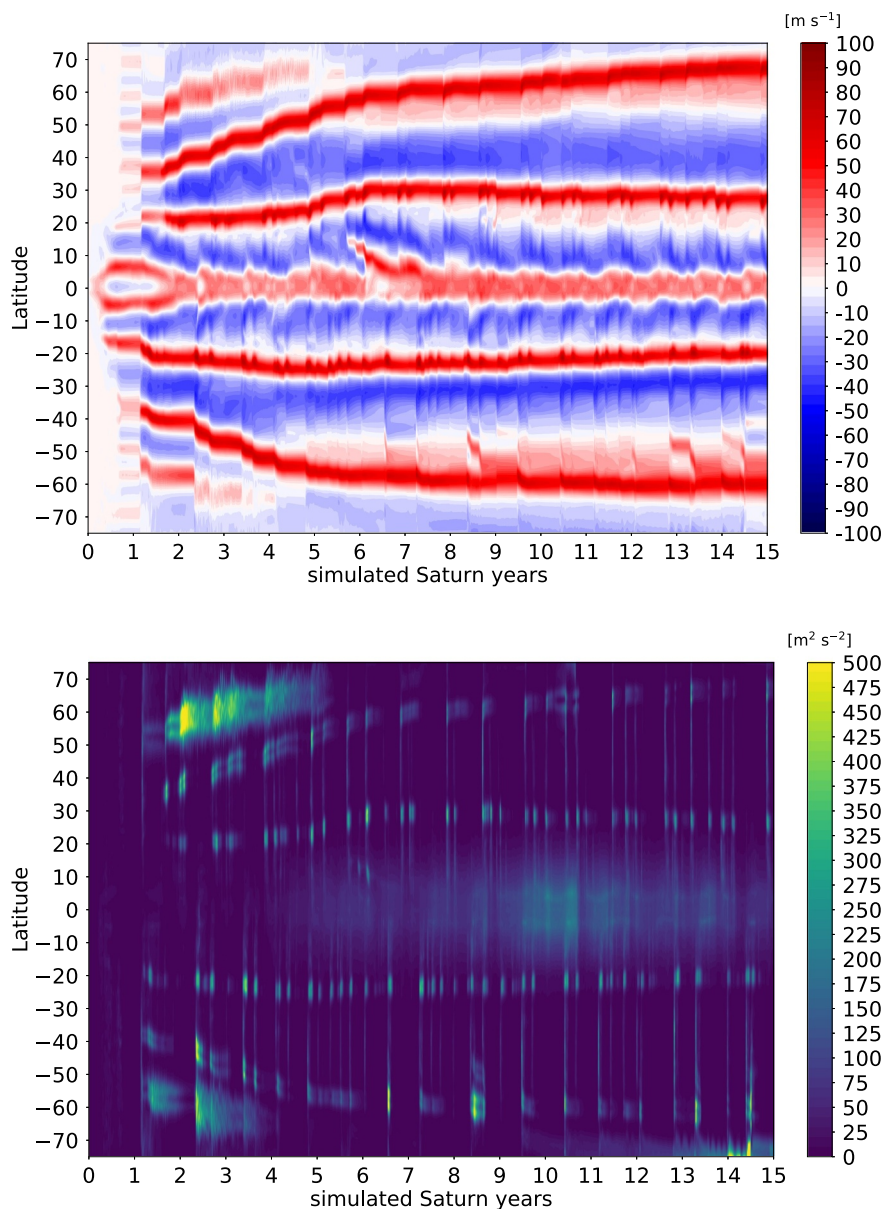
Fig. 13. Evolution of the zonal-mean zonal wind $\bar{u}$ (top plot) and the zonal mean of the Eddy Kinetic Energy (EKE) $1/2(\overline{u'^2} + \overline{v'^2})$ (bottom plot) in Saturn troposphere (800 mbar) within the whole 15-year duration of our Saturn DYNAMICO GCM simulation.

Fig. 13. It takes about 6–7 simulated Saturn years for the jet system to reach what most closely resembles a steady-state equilibrium; a similar conclusion was drawn from the analysis of the temporal evolution of AAM (Fig. 22 in Section A.1). The zonal mean of the Eddy Kinetic Energy (EKE)

$$\bar{e} = \frac{1}{2}(\overline{u'^2} + \overline{v'^2}) \tag{6}$$

is also shown in Fig. 13 to diagnose eddy activity.

The first years of our Saturn DYNAMICO GCM simulations follow the evolution of zonal jets typically obtained with nonlinear analytical models prone to barotropic and baroclinic instability. The evolution of our Saturn DYNAMICO GCM displayed in the top panel of Fig. 14 is similar to the evolution described, e.g., in Fig. 10 of Kaspi and Flierl (2007). The first simulated half-year exhibits no particular zonal organization (except at the equator). In the second half of the first simulated year, the growth of the fastest unstable mode leads to the emergence of numerous weak zonal jets, which subsequently reorganize, as additional growing eddy modes are present, to lead to a

system with less, and wider, jets. The abrupt transition around 1.15 simulated years in Fig. 13 is associated with significant eddy activity. The merging of numerous weak jets into a final jet structure with lesser and stronger jets is typical of the inverse energy cascade by geostrophic turbulence which shapes the jet structure (Cabanes et al., 2017). Another typical feature of the inverse energy cascade shown in Fig. 15 is the overall correlation between the Rhines scale (Rhines, 1975)

$$L_\beta = 2\pi\sqrt{\frac{U}{\beta}} \qquad \text{with} \qquad U = \sqrt{2\bar{e}} \tag{7}$$

and the eastward jets' width/spacing (Chemke and Kaspi, 2015b), with a tendency for broader jets and increased spacing between jets towards higher latitudes (Kidston and Vallis, 2010). A full exploration of the dynamical regimes (e.g., zonostrophy) and the inverse energy cascade in our Saturn DYNAMICO GCM requires detailed spectral analysis of the flow energetics (Sukoriansky et al., 2002; Galperin et al., 2014; Young and Read, 2017) that will be developed in a follow-up paper (Cabanes S. et al., Part III submitted).
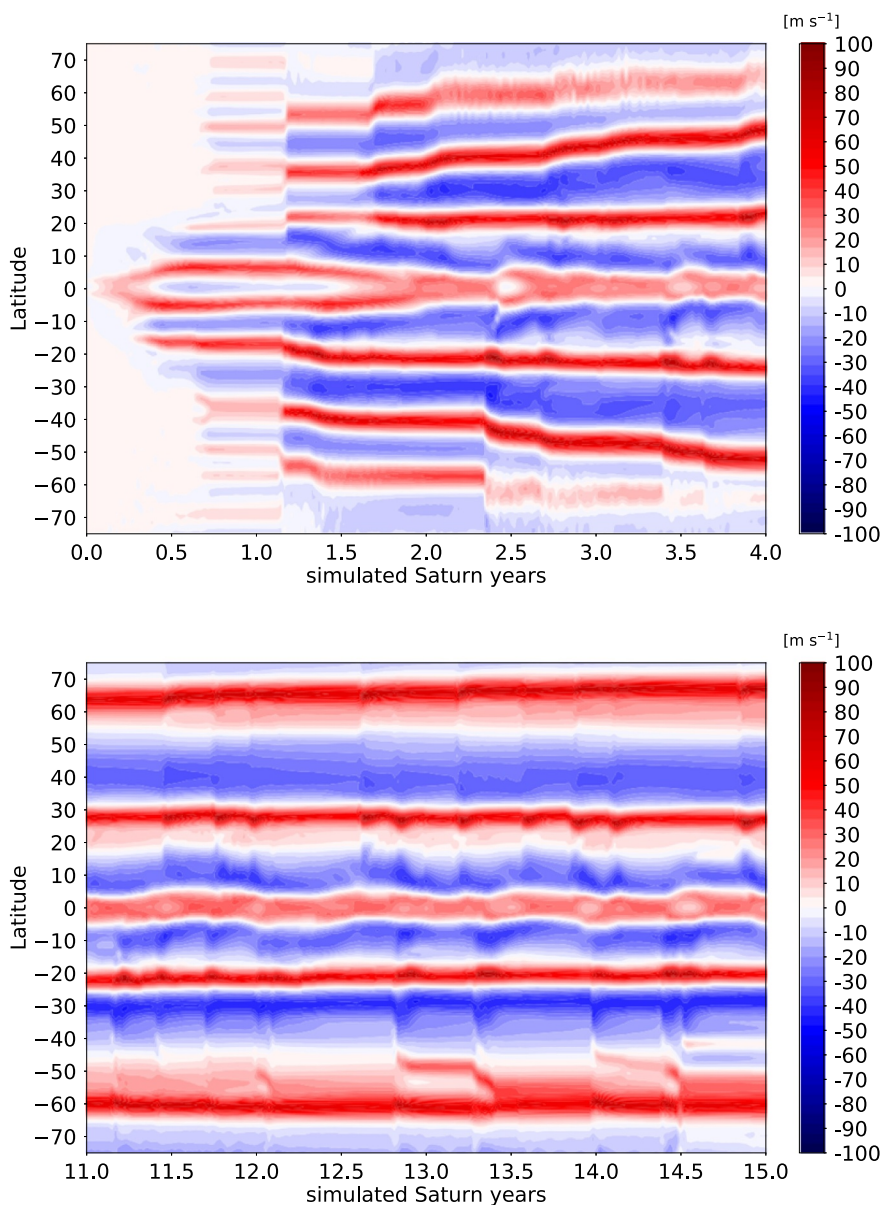
Fig. 14. Same as Fig. 13 with an emphasis on (top) the first four and (bottom) the last four simulated Saturn years of the full 15-year duration of our Saturn DYNAMICO GCM simulation.
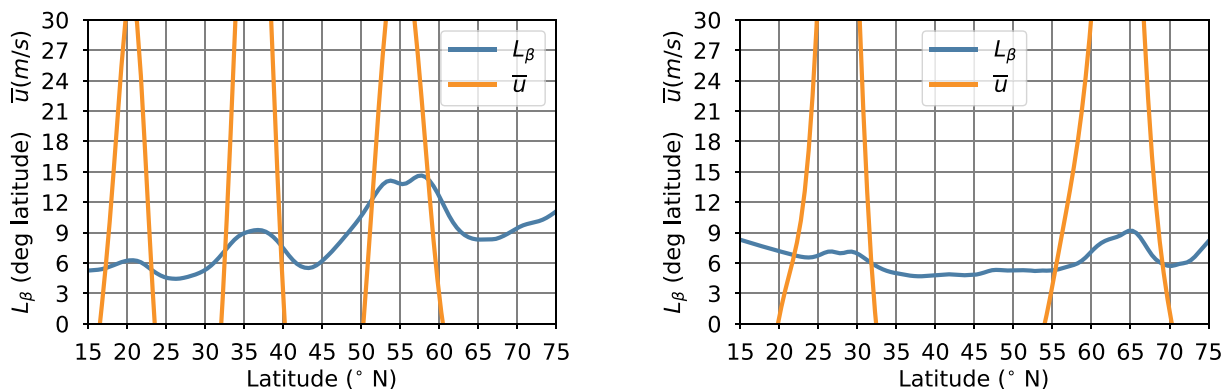

Fig. 15. Meridional profiles of the Rhines scale L_{β} defined as in Eq. (7) (orange line) and eastward jet speed $\bar{u}$ (blue line). Those quantities are vertically-averaged in the pressure range $[10^5, 10^3]$ Pa. The left plot shows a temporal average within half of the second simulated year (during dynamical spin-up and strong jet migration) and the right plot within half of the twelfth simulated year (quasi-steady state). The correlation between the Rhines scale and the jet width/spacing is more obvious in the former than in the latter. The left plot is computed in conditions of strong poleward migration of the eastward jets, a temporal evolution resembling the simulations in Chemke and Kaspi (2015b) . (For interpretation of the references to color in this figure legend, the reader is referred to the web version of this article.)

The most prominent feature of Fig. 13 between the simulated years 1 and 6 is the poleward migration of mid-latitude jets. This echoes the idealized simulations detailed in Chemke and Kaspi (2015a) (see also jovian simulations by Williams, 2003). The migration is gradual, but the jet migration is much stronger in short-lived episodes characterized by a burst of eddy activity, which implies momentum transfer to the jet altering its meridional structure. A detailed analysis of a typical poleward migration episode in Fig. 13 is proposed in Section 4.3. The tropical jets undergo a much weaker migration than the mid-latitude jets. Most of the migration events are poleward, but there is at least one clear equatorward migration event of a jet appearing at latitude 15°N in the beginning of year 7. This equatorward migration contributes to accelerate the equatorial jet. This was also noticed by Young et al. (2019a) in their Jupiter GCM, although their simulations exhibit a global tendency for equatorward jet migration, contrary to the global tendency for poleward jet migration found in our GCM simulations and in Chemke and Kaspi (2015a).

The poleward migration of the mid-latitude jets continues until the migration rate slows down and the zonal jets reach their final latitude of occurrence in our Saturn DYNAMICO GCM simulation. Starting from the seventh simulated year to the fifteenth simulated year (Figs. 13 top and 14 bottom), we notice a continuing, very slow poleward migration of the mid-latitude eastward jets and equatorward migration of the tropical jets. The 15-year duration of our Saturn DYNAMICO GCM simulation allows us to reach robust conclusions about the overall steady-state jets' structure and intensity; the long duration of our simulations also allows us to conclude that this jet structure is still impacted by a slowly-evolving transient state over timescales of tens of Saturn years. It is important to note here that we are not interpreting our Saturn GCM simulations as indicative of a current migration of Saturn zonal jets, which is not supported by observations. Our GCM simulations start with a zero-wind state which is not encountered in the actual Saturn's atmosphere, and may have never been encountered in the past history of Saturn's atmosphere. Thus, we can only speculate that jet migration could have been an important process in the past evolution of Saturn's atmosphere and might explain the present latitudes of Saturn's zonal jets.

The bursts of eddy activities are also associated with acceleration of the zonal jets, would it be a case of a migration episode or not (once the jets have migrated, the impact of the eddies is actually solely jet acceleration and no longer migration). This suggests that eddy forcing plays a great role in shaping the zonal jets in Saturn's atmosphere, as argued by existing modeling studies (Showman, 2007; Lian and Showman, 2010; Liu and Schneider, 2010) and Cassini observations (Del Genio and Barbara, 2012; Del Genio et al., 2007). We discuss this matter in Section 4.2 for a global analysis and Section 4.3 for a local analysis. Despite our Saturn DYNAMICO GCM resolving the seasonal evolution of Saturn's troposphere and stratosphere, there is no clear seasonal trend associated with the bursts of mid-latitude eddy activity (although the typical timescale between the bursts is close to one year). This is in line with theoretical studies supporting abrupt stochastic transitions in the zonal jet structure prone to barotropic and baroclinic instabilities (Bouchet and Simonnet, 2009; Bouchet et al., 2013). The typical timescale between bursts is not so much set by the seasonal cycle, but by the typical life cycle of instabilities (Panetta, 1993).

4.2. Kinetic energy conversion rate

To investigate the mechanism by which zonal banded jets arise in our Saturn DYNAMICO GCM simulation, we first consider a global diagnostic, the conversion rate C of eddy-to-mean kinetic energy. Cloud tracking with Cassini Imaging Science Subsystem (ISS) images has been employed to address the driving of Saturn's zonal jets by eddy momentum fluxes (Del Genio et al., 2007; Del Genio and Barbara, 2012). The conversion rate C in $m^2 s^{-3}$ (or $W kg^{-1}$), estimating the conversion per unit mass of eddy kinetic energy to zonal-mean kinetic energy, can

be obtained by multiplying eddy momentum transport $\overline{u'v'}$ by the meridional curvature of the zonal flow $\frac{\partial \bar{u}}{\partial y}$.

$$C = \overline{u'v'} \, \frac{\partial \bar{u}}{\partial y} \tag{8}$$

Wind observations by cloud tracking exhibit a globally positive conversion rate $C > 0$, both at the middle troposphere ammonia cloud at 1 bar and the upper troposphere haze at 100 mbar, which suggests that Saturn's zonal jets are eddy-driven (Del Genio and Barbara, 2012). The fact that C is positive means that the eddy flux is, on average, equatorward in cyclonic shear regions and poleward in anticyclonic shear regions (Del Genio and Barbara, 2012), hence eastward jets are accelerated by the convergence of eddy flux while westward jets are decelerated by the divergence of eddy flux (see also PV discussions in Section 3.2.1). The values of kinetic energy conversion rate observed by Cassini by Del Genio and Barbara (2012) (their Fig. 11) are large: $C \sim 1 \times 10^{-5} \, W \, kg^{-1}$ at 100 mbar, and four times larger in the troposphere at 1 bar. Those estimates of the energy conversion rates support the idea that eddy momentum transfers are able to maintain jets against dissipation. Similar conclusions were reached for Jupiter's weather layer by Salyk et al. (2006).

The positive conversion rates C simulated by our Saturn DYNAMICO GCM, shown in Fig. 16, indicate that our model supports the conclusion of Del Genio and Barbara (2012) that Saturn's zonal banded jets are, for a significant part, driven and maintained by eddies in the weather layer (see also Read et al., 2009a). This also confirms the diagnostics obtained from previous GCM studies (Lian and Showman, 2008; Liu and Schneider, 2010). In the upper troposphere haze layer at 100 hPa, our model predicts $C \sim 0.5 \times 10^{-5} \, m^2 \, s^{-3}$, which matches to the order-of-magnitude the quantitative estimates obtained from Cassini by Del Genio and Barbara (2012), implying a typical timescale of replenishing the jets of less than a Saturn year. This shows that our Saturn DYNAMICO GCM resolves a satisfactory conversion rate from eddies to zonal jets in the tropopause, providing support for a "downward control" of jets at deeper levels (Haynes et al., 1991) by eddy forcing in the radiatively-driven upper troposphere, as proposed by Schneider and Liu (2009) and Liu and Schneider (2010). Nevertheless, our modeled values for C are half those obtained by cloud tracking on board Cassini, indicating room for improvement in predicting the eddy activity and jet curvature resolved by our GCM in the upper troposphere, suggesting the need for either more accurate radiative computations, or an additional physical process causing eddies.

The conversion rate C increases with altitude in our Saturn GCM simulation, whereas it decreases with altitude in the Cassini observations of Del Genio and Barbara (2012). In other words, if our simulations match the observations at 100 mbar, the conversion rate at the cloud layer is one order of magnitude lower in the Saturn GCM simulations than it is in the observations. Del Genio and Barbara (2012) already noticed this discrepancy by comparing their data to the GCM results of Liu and Schneider (2010). We speculate that our simulated eddy forcing of jets being compliant with observations in the radiatively-driven tropopause, but not in the deeper troposphere, indicates that a source of tropospheric eddy forcing (e.g. latent heat release and convective motions associated with moist processes Zuchowski et al., 2009; Lian and Showman, 2010) is missing in our Saturn GCM. This is also consistent with our equatorial jet super-rotating too weakly for a possible lack of convectively-generated Rossby waves (Schneider and Liu, 2009).

4.3. Local analysis of eddy-induced jets

The approach using kinetic energy conversion rate in Section 4.2 is to be understood on a global sense; here we present diagnostics for eddy-induced jets that bear a more local sense.

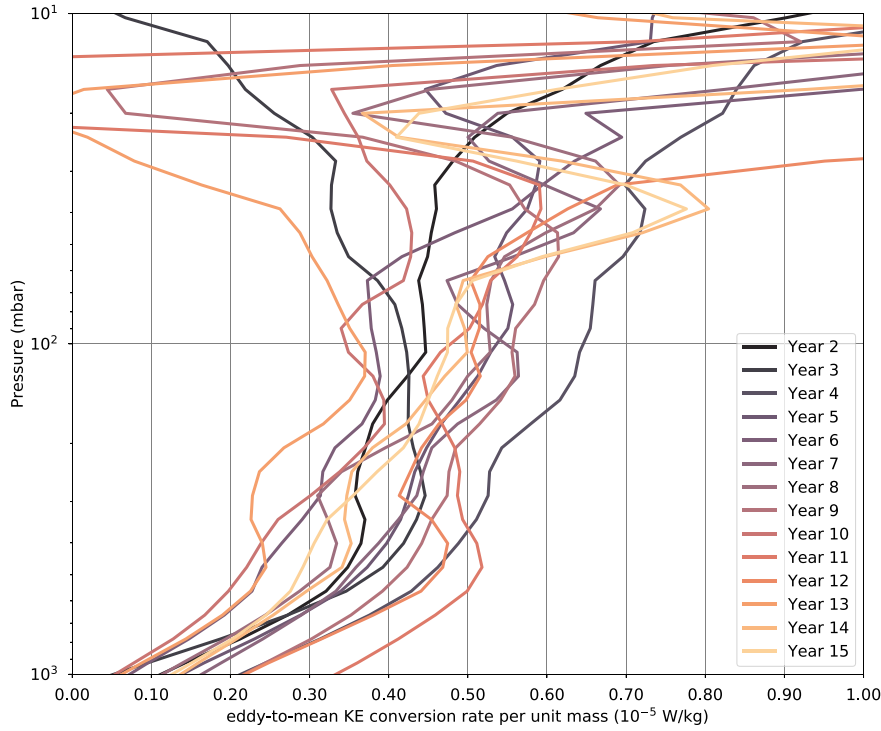We can consider, as a typical and particularly illustrative example,

Fig. 16. Rate per unit mass C in $\mathrm{m}^2\,\mathrm{s}^{-3}$ (or $\mathrm{W\,kg}^{-1}$) estimating the conversion of eddy kinetic energy to zonal-mean kinetic energy. Vertical profiles of C are shown, annually-averaged (one line per simulated year, from year 2 to 15) and globally-averaged (60°S to 60°N latitudes) This spatial and seasonal averaging is chosen to allow a direct comparison with Cassini estimates of C in Del Genio and Barbara (2012) .

the impact of the strong burst of eddy activity taking place in the northern hemisphere within 1000 Saturn days between 1.6 and 1.7 simulated years (Fig. 13). In order to study the contributions to the zonal acceleration, the Eulerian-mean form of the zonal-mean zonal momentum equation of the atmospheric flow motion can be written as follows

$$\frac{\partial \bar{u}}{\partial t} = \left[\frac{\partial \bar{u}}{\partial t}\right]_{\mathrm{R}} + \left[\frac{\partial \bar{u}}{\partial t}\right]_{\mathrm{E}} + \overline{\mathcal{X}} \tag{9}$$

where $\mathcal{X}$ is a mean nonconservative force such as e.g. diffusion, and the respectively "residual-mean" and "eddy-related" terms are written (e.g. Eq. 2.5 in Andrews et al., 1983)

$$\left[\frac{\partial \bar{u}}{\partial t}\right]_{\mathrm{R}} = -\left[\frac{1}{a\cos\varphi}\frac{\partial \bar{u}\cos\varphi}{\partial \varphi} - f\right]\bar{v} - \frac{\partial \bar{u}}{\partial p}\bar{\omega} \tag{10}$$

$$\left[\frac{\partial \bar{u}}{\partial t}\right]_{\mathrm{E}} = -\frac{1}{a\cos^2\varphi}\frac{\partial \overline{u'v'}\cos^2\varphi}{\partial \varphi} - \frac{\partial \overline{u'\omega'}}{\partial p} \tag{11}$$

The contributions of each of those terms, within the considered 1000 Saturn days prone to significant eddy activity, are provided in Fig. 17. As was also noticed by Lian and Showman (2008, their Fig. 8), the two terms described in Eqs. (10) and (11) are generally anti-correlated, which indicates that a significant part of eddy-related acceleration (which might reach $2 \times 10^{-6}\,\mathrm{m\,s}^{-2}$ on average over 1000 Saturn days) contributes to maintaining an associated meridional circulation, in addition to contributing to the zonal jets. Under the assumption of steady-state zonal jets ($\partial u/\partial t \simeq 0$), the quasi-equilibrium between eddy-related and meridional-circulation terms is used in studies exploring the circulations underlying observed temperature and aerosol fields in gas giants (e.g., West et al., 1992).

The three northern zonal jets featured in Fig. 17 illustrate the possible distinct outcome of local eddy forcing: the 21°N eastward jet is slightly accelerated, in a situation where the residual-mean and eddy-related terms almost compensate; the 35°N eastward jet does not

accelerate at its core, but is migrating as a result of an eddy-induced acceleration on its poleward flank; the 52°N eastward jet undergoes strong eddy perturbations, especially on its poleward flank, not compensated by an evolution of the residual-mean circulation, which results in both a poleward migration and an acceleration of this eastward jet. Note that, concomitantly with this overall acceleration of the eastward jets, westward jets are decelerating. This supports the interpretation proposed in Sections 3.2.1 and 4.2, and in the literature (e.g., Schneider and Liu, 2009), that there is a net transfer of momentum from the westward jets towards the eastward jets.

A complementary framework to study the evolution of jets – especially the eddy-related acceleration – is the Transformed Eulerian Mean approach. In this approach, the Eliassen-Palm (EP) flux $\mathcal{F}$ (e.g., Vallis, 2006), which meridional component writes in isobaric coordinates (e.g. Eq. 2.7 in Andrews et al., 1983)

$$\mathcal{F}_\varphi = a\cos\varphi\left(-\overline{u'v'} + \psi\frac{\partial \bar{u}}{\partial p}\right) \quad \text{with} \quad \psi = -\overline{v'T'}/\left(\frac{R\,\bar{T}}{c_p\,p} - \frac{\partial \bar{T}}{\partial p}\right) \tag{12}$$

provides a direct link between the convergence/divergence of eddy momentum and the resulting acceleration/deceleration of zonal jets. The horizontal contribution of eddies to zonal-mean wind acceleration is the divergence of the meridional component $\mathcal{F}_\varphi$ of the EP flux

$$\left[\frac{\partial \bar{u}}{\partial t}\right]_{\mathrm{eddies}} = \frac{1}{a^2\cos^2\varphi}\frac{\partial \mathcal{F}_\varphi\cos\varphi}{\partial \varphi} \quad \left(\simeq -\frac{1}{a\cos^2\varphi}\frac{\partial \overline{u'v'}\cos\varphi}{\partial \varphi}\right) \tag{13}$$

(The vertical contribution of eddies to zonal-mean wind acceleration is omitted in this equation because, in the specific context of our analysis of eddy-driven jets, it was found to be negligible). We use the expression in Eq. (12) to diagnose the eddy-driven acceleration in our Saturn GCM simulations; we note, however, that the approximate expression in parenthesis (used e.g. to interpret Fig. 8 in Section 3.2.2) is reasonable in a vertically-integrated quasi-geostrophic framework, with zonal
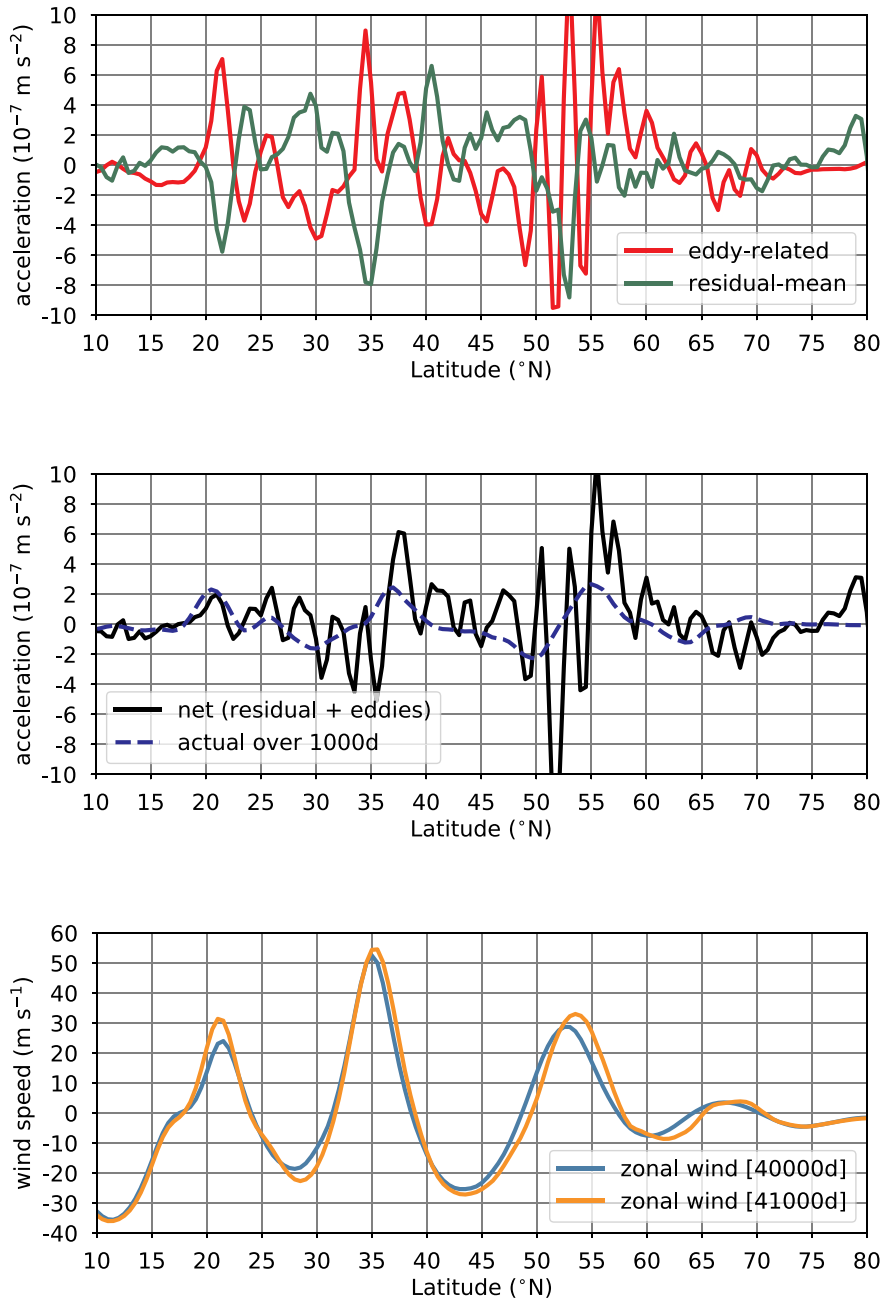
Fig. 17. Meridional profiles of the zonal-mean acceleration terms in the Eulerian-mean formalism described by Eq. (9). The analysis is carried out after 41 thousands simulated Saturn days (around 1.6 simulated year), corresponding to a typical burst of eddies in the northern hemisphere evidenced in Fig. 13. The plots are obtained after averaging over 1000 Saturn days. The residual-mean term (Eq. (10)) is shown in the red line and the eddy-related term (Eq. (11)) is shown in the green line. The net resulting acceleration is shown in the black full line and the actual acceleration obtained within the considered 1000 days is shown in the dashed blue line. The comparison of the latitudinal profiles of zonal-mean zonal winds at the beginning and in the end of the 1000-day sequence are shown respectively in light blue and orange in the bottom plot. (For interpretation of the references to color in this figure legend, the reader is referred to the web version of this article.)

averaging making mean momentum flux convergence terms to be small compared to the eddy momentum flux convergence terms (Hoskins et al., 1983; Vallis, 2006; Chemke and Kaspi, 2015a).

As was found from analyzing Fig. 17, the 35°N eastward jet in the end of the first simulated year typically undergoes a poleward migration associated with a burst of eddy activity; this eddy-driven migration is continuing in the beginning of the second simulated year. Fig. 18 indicates that the divergence of the Eliassen-Palm flux associated with this eddy activity indeed acts to slow down the jet core and accelerate its flanks, with a larger acceleration being experienced in the poleward side.

4.4. Barotropic vs. baroclinic instability of the jets

The importance of barotropic and baroclinic instabilities has been discussed in the existing literature as the source for gas giants' banded jets (Dowling, 1995; Liu and Schneider, 2010) and the evolution thereof, notably migration (Williams, 2003; Chemke and Kaspi, 2015a). Just as the vertical gradient of potential temperature enables to assess convective instability, the meridional gradient of potential vorticity enables to assess barotropic/baroclinic instability (Dowling, 1995; Holton, 2004; Vallis, 2006). The Rayleigh-Kuo [RK] necessary condition for barotropic instability is that the meridional gradient of PV

$$\left[\frac{\partial \bar{q}}{\partial y}\right]_{BT} = \beta - \frac{\partial^2 \bar{u}}{\partial y^2} \tag{14}$$

changes sign in the domain interior. The Charney-Stern-Pedlosky [CSP] necessary condition for baroclinic instability is that the full-baroclinic meridional gradient of PV

$$\left[\frac{\partial \bar{q}}{\partial y}\right]_{BC} = \left[\frac{\partial \bar{q}}{\partial y}\right]_{BT} - \frac{1}{\rho_0}\frac{\partial}{\partial \mathcal{Z}}\left[\rho_0 \frac{f_0^2}{N^2}\frac{\partial \bar{u}}{\partial \mathcal{Z}}\right] \qquad \mathcal{Z} = -H\ln(p/p_0) \tag{15}$$
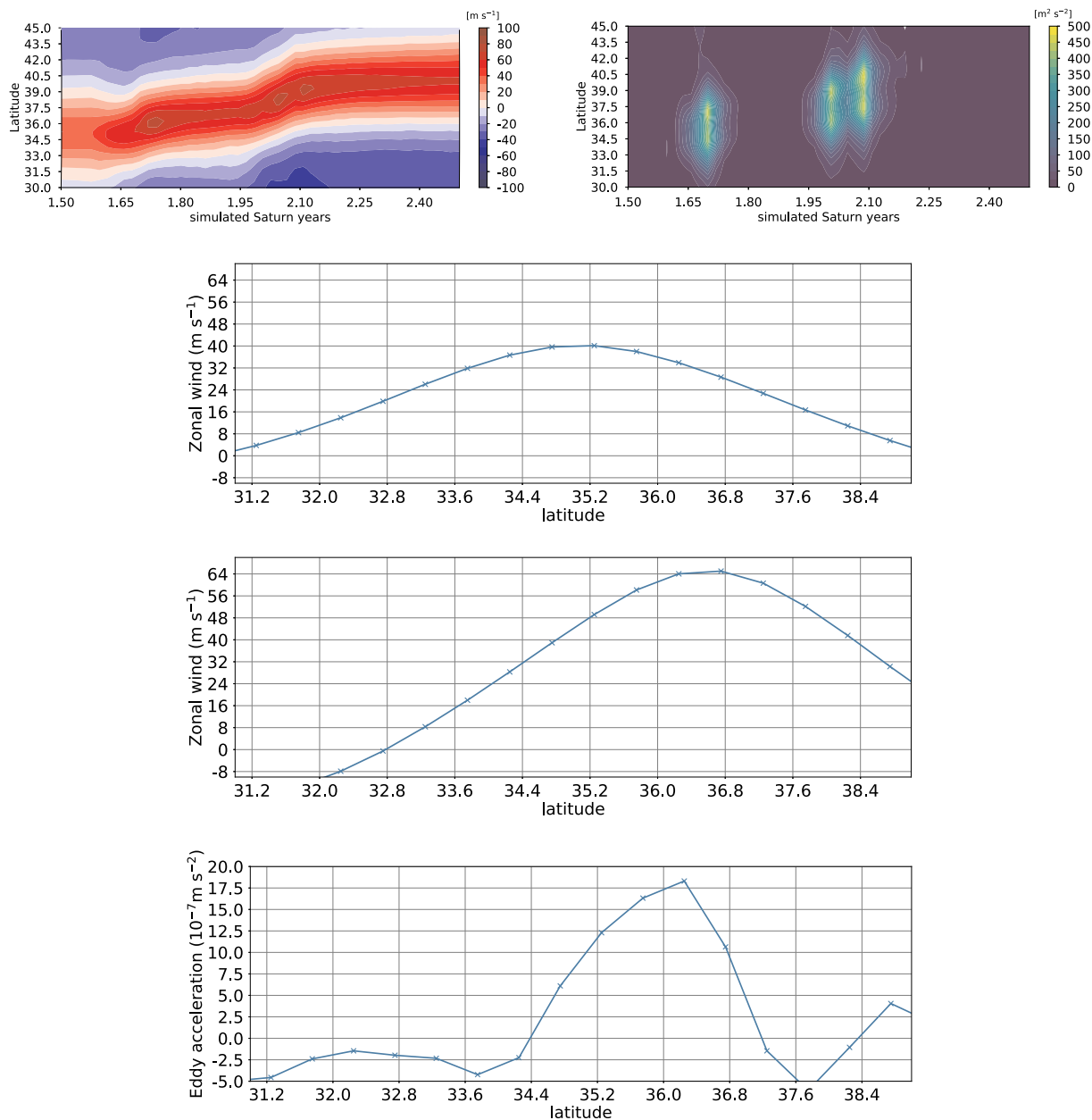
Fig. 18. An episode of the poleward migration of a mid-latitude jet is shown on the top two figures offering a magnified view of a relevant portion of Fig. 13 showing an episode of jet migration. The latitudinal profiles of the zonal-mean zonal jet at the beginning and in the end of the temporal interval spanned by the top plots are shown as middle plots (pressure level is 200 mbar). The bottom plot features the acceleration term obtained by Eq. (13) (computation of the divergence of the Eliassen-Palm flux).

either: changes sign in the interior [CSP1, similar to RK], is the opposite sign to $\bar{u}_Z$ at the upper boundary [CSP2], is the same sign as $\bar{u}_Z$ at the lower boundary [CSP3], or is zero and $\bar{u}_Z$ is the same sign at both boundaries [CSP4]. The CSP criterion is not defined in a neutral layer (where $N^2 \sim 0$) such as Saturn's troposphere, thus we carry out the analysis of the two necessary conditions in Eqs. (14) and 15 near the tropopause level in our simulations.

The necessary condition RK for barotropic instability can be assessed from Fig. 19 by determining when the quantity described by Eq. (14) changes sign. In the first four simulated years, the mid-latitude eastward jets migrating from 30°N/S to 60°N/S fulfil the RK condition on the poleward flanks, but not on the equatorward flank. In subsequent years (from year 5 to year 15) in our Saturn DYNAMICO GCM simulations, those eastward jets fulfil the RK on both flanks, which is also the case for the weakly-migrating 20°N/S jets throughout the 15-year simulation. The simulated mid-latitude jets in our Saturn DYNA-MICO GCM are thus possibly impacted by barotropic instability; this could be expected from the PV mapping in Fig. 12 which clearly shows that strong inversions of the meridional gradients of PV are found at the location of the eastward jets. This provides an explanation for the extratropical eddies found in the bulk of eastward jets and discussed in Section 3.3.2. It is worth reminding here that barotropic instability acts to transfer momentum from jets to eddies, and not the contrary. Hence the positive conversion rate C indicating an overall transfer from eddies to jets (Section 4.2) hints at baroclinic instability complementing barotropic instability.

Referring to the CSP1 criterion, Fig. 19 shows that the conditions for baroclinic instability are met in polar regions — this is also true for barotropic instability according to the RK criterion. In mid-latitude eastward jets, the CSP1 necessary criterion for baroclinic instability is
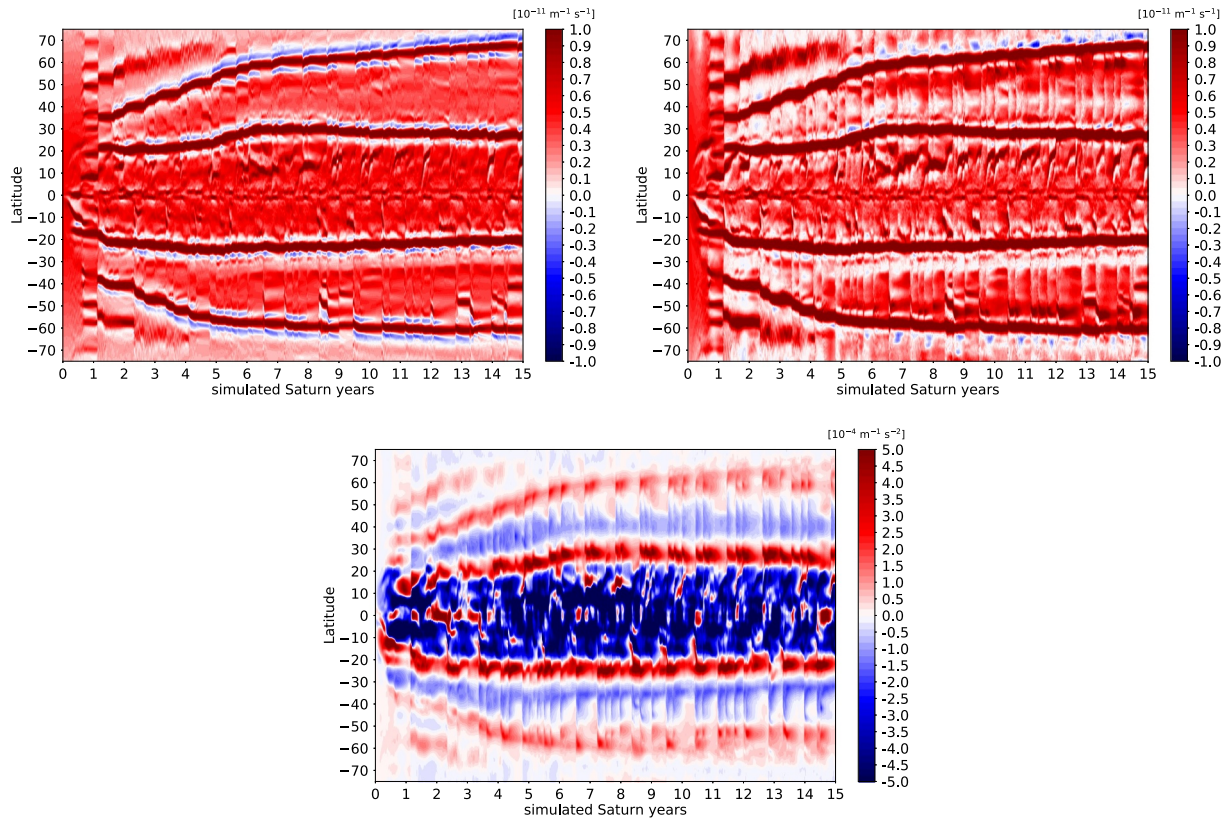
Fig. 19. Evolution of the meridional gradients of zonal-mean potential vorticity (top left: barotropic, Eq. (14) for necessary condition RK, top right: baroclinic, Eq. (15) for necessary condition CSP1) and vertical shear of zonal-mean zonal wind (bottom) at Saturn's tropopause (100 mbars) within the whole 15-year duration of our Saturn DYNAMICO GCM simulation. The diagnostic in Eq. (14) cannot be computed in the troposphere where the atmosphere is neutral ($N^2 \sim 0$) and barotropic; the two other diagnostics are shown at the tropopause for consistency but are similar at deeper levels.

however only verified in the poleward flank of the jets; the quantity described in Eq. (15) is mostly positive at all latitudes (outside polar regions). The fact that the CSP1 criterion for baroclinic instability is fulfilled in the poleward flank of the mid-latitude jets, and less so in the equatorward flank, echoes the conclusions of Chemke and Kaspi (2015a) who demonstrated that the poleward migration of jets in idealized GCM simulations of high-rotation planets is caused by a poleward bias in baroclinicity across the width of the jet.

The condition CSP3 is fulfilled in the simulated mid-latitude eastward jets since the (baroclinic) meridional gradient of PV is of the same sign as the vertical shear $\bar{u}_z$, i.e. positive as is shown in Fig. 19 (see also Section 3.2.1). Those simulated jets could thus be baroclinically unstable[1]. This is not the case for the equatorial eastward jet, and the broad westward jets, for which vertical shear is negative.

We conclude that both barotropic and baroclinic instabilities could account for the maintenance, migration and (in polar regions) disappearance of eastward zonal jets in our Saturn DYNAMICO GCM simulations. The putative role of baroclinic instability in driving the mid-latitude jets was also highlighted by Liu and Schneider (2010); the possibility that barotropic and baroclinic instabilities exist in Saturn's troposphere is also argued in Studwell et al. (2018). In that respect, the pole-to-equator meridional gradient of temperature in the deep troposphere (e.g. at pressures greater and equal to 500 mbar) is a key constraint for baroclinic instability, owing to its link to the vertical shear of zonal wind involved in the CSP3 criterion, through the thermal wind equation.

The equator-to-pole temperature gradient of 4 K found at the 500-

mbar level in Figs. 2 and 3 (bottom) translates into about 7 K at the 2.5-bar level, in accordance with potential temperature being constant in the neutral lower troposphere. Both correspond to an equator-to-pole gradient of potential temperature of 7 K. As is discussed in Section 3.1, while a good agreement between our model and the observations is obtained in the upper troposphere/lower stratosphere (Fig. 4), the simulated baroclinicity in the lower troposphere is at least twice larger than it is in the observations. In addition to this, the shallowness of our Saturn GCM (as well as other models sharing the same strategy, e.g. Liu and Schneider, 2010) prevents it from resolving the deep large-scale circulations that could act to counteract and further homogenize the meridional gradients of potential temperature in the deeper troposphere (Aurnou et al., 2008). According to the CSP3 criterion, an unrealistic baroclinicity at the bottom boundary entails that part of the eddies resolved by our Saturn DYNAMICO GCM could be spurious and not occurring in the real Saturn – contrary to the baroclinicity associated with PV gradient reversals within the atmospheric fluid related to the CSP1 criterion. This would impact the structure of the resolved zonal jets, as well as their meandering and migration. A similar word of caution applies to the analysis of the conversion rate C in Fig. 16 and Section 4.2, even if the order of magnitude compared to observations is correct. For instance, the fact that baroclinic instabilities cause unrealistically strong jet meandering in polar regions may be deemed an indication that meridional gradients could be improved at the bottom of our model. Deepening the model bottom and ensuring a more realistic baroclinicity in the lower troposphere is an area of future improvement of our Saturn DYNAMICO GCM, as is the case for most existing shallow-atmosphere models.

---

[1] CSP3 is often the decisive condition in the terrestrial environment too, see Vallis (2006). An assessment of conditions CSP 2 and CSP 4 in the case of our Saturn DYNAMICO GCM simulations indicates that those are not fulfilled.
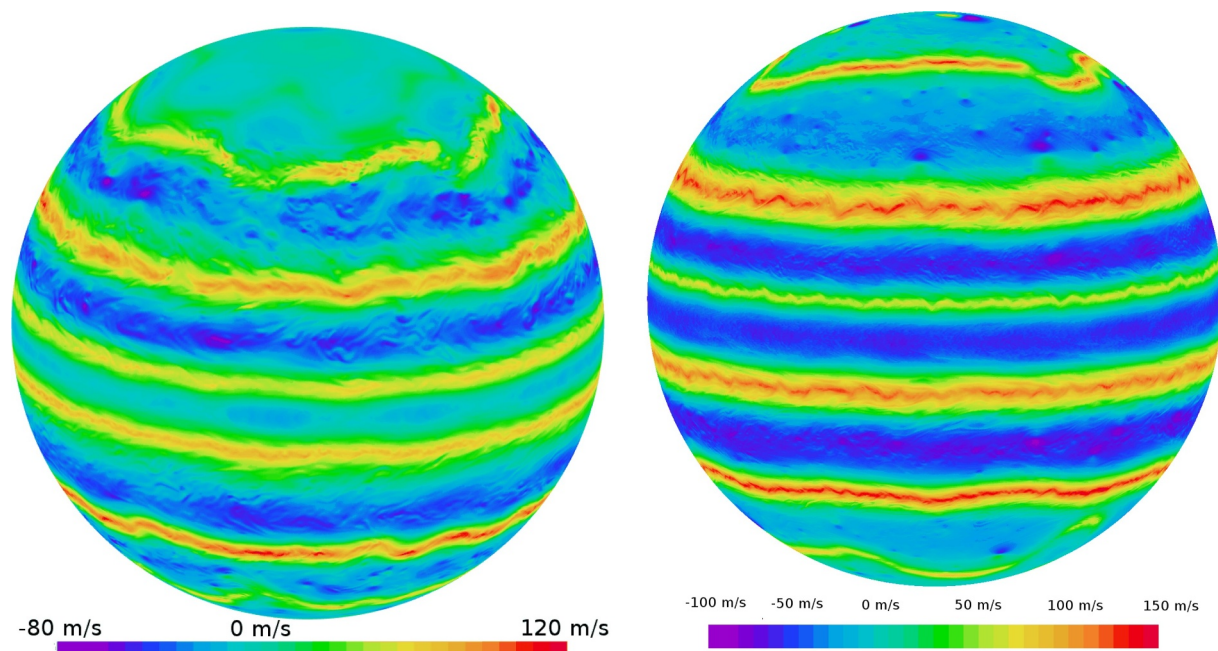
Fig. 20. Instantaneous zonal winds predicted at 0.5 bar (yellow/red: prograde jets, blue/violet: retrograde jets) after 500 simulated Saturn days by our Saturn DYNAMICO GCM. Our simulations used a horizontal resolution of 1/4° (left) and 1/8° (right) longitude, and extent from troposphere to the stratosphere. In the left plot, jets' instabilities and filamentation can be noticed; in the right plot, the even finer horizontal resolution allows the model to reproduce the propagation of gravity waves on the flanks of the jets, as well as the possible emergence of traveling vortices (cf. blue/green spots in the northern hemisphere). The objectives behind those simulations were more technical (testing a massively-parallel computing cluster) than scientific: the strong hyperdiffusion made the structures seen in the figure to disappear after about a thousand simulated Saturn days. (For interpretation of the references to color in this figure legend, the reader is referred to the web version of this article.)

5. Conclusions

The conclusions of our study can be summarized as follows.

1. The Cassini mission opened novel questions on tropospheric and stratospheric circulations on Saturn, with new modeling challenges (Section 1 and challenges C_1, C_2, C_3, and C_4).
2. The Global Climate Model (GCM) we built is named the Saturn DYNAMICO GCM and couples the radiative transfer of Guerlet et al. (2014) tailored for Saturn with the icosahedral dynamical core DYNAMICO of Dubos et al. (2015) tailored for massively-parallel computing resources (Section 2).
3. Care must be taken when developing a GCM for gas giants in setting the subgrid-scale dissipation and verifying the conservation of global axial angular momentum (Appendix A).
4. We reached the capability to simulate the dynamics of Saturn's atmosphere from the troposphere to the lower stratosphere during 15 Saturn years with an horizontal resolution of 1/2° longitude/ latitude, which made our reference simulation (Sections 3 and 4); our Saturn DYNAMICO GCM produces a satisfactory thermal structure, and seasonal variability thereof, compared to Cassini CIRS measurements (Section 3.1).
5. The number and intensity of mid-latitude eastward jets (and broad westward jets) reproduced by the reference GCM simulation is compliant with observations, although slightly underestimated, but no stable circumpolar jet (less so hexagonal-shaped) is reproduced; those jets' intensities increase with altitude and their latitudinal organization exhibits potential-vorticity staircases (Section 3.2.1).
6. The GCM simulation exhibits at the equator both a superrotating zonal jet in the troposphere and stacked alternating zonal jets in the stratosphere; nevertheless, the former is one order of magnitude less powerful than the observed jet, and the latter are not downward-propagating with time as would be expected from the observed equatorial oscillation (Section 3.2.2).
7. Our model produces a wealth of Yanai (Rossby-gravity), Rossby and Kelvin waves in the tropical channel, part of them hinted at in available observations (Section 3.3.1).
8. Outside the tropics, the cores of eastward jets are perturbed by Rossby waves reminiscent of Ribbon-like waves, while westward jets host an eddy activity not especially organized in vortices, which transitions in polar regions into a predominance of large-scale vortices (Section 3.3.2).
9. In the 15-Saturn-year course of our Saturn DYNAMICO GCM simulation, eastward jets undergo poleward migration and perturbations by bursts of eddies (Section 4.1).
10. The global kinetic energy conversion rate simulated in our Saturn DYNAMICO GCM, albeit half the value of the observed estimates, is positive and argues for a significant contribution of eddy acceleration in driving the eastward jets (Section 4.2).
11. The acceleration (and, if applicable, migration) of jets caused by eddy momentum transfers is evidenced by local analysis with either Eulerian-mean or transformed Eulerian-mean formalism (Section 4.3).
12. Eastward jets produced by our Saturn DYNAMICO GCM are prone to both barotropic and baroclinic instabilities (Section 4.4).

Based on the present study, and the comparison between available observations and our GCM simulations, we can envision the following improvements of our Saturn DYNAMICO GCM in the future:

(a) to refine the horizontal resolution to 1/4°;
(b) to include a physically-based parameterization for subgrid-scale dry and moist convection, and to subsequently deepen the model bottom to 10–20 bars;
(c) to extend the model top to the upper stratosphere and to refine the vertical resolution in the troposphere and the stratosphere;
(d) to implement a parameterization for the impact of unresolved mesoscale gravity waves on the mean flow.

This list is not exhaustive, but represents the near-future evolution of our model. Long-term developments would be inspired by the model-coupling methodology for the climate of telluric planets, i.e. coupling our Saturn DYNAMICO GCM with stratospheric photo-chemical models, deep-interior convection models and upper-atmosphere thermo-ionospheric models.

What the refinement of horizontal resolution would bring to Saturn GCM studies can be illustrated by the tests of an earlier version of the Saturn DYNAMICO GCM at the horizontal resolutions of 1/4° and 1/8°. We carried out overdissipated GCM simulations at those resolutions, using both a sponge layer and hyperdiffusion timescales of the order $\tau_D = 500$–1000 s, to ensure overly-conservative numerical stability in order to test the performance of the model on massively-parallel architectures (up to 60,000 cores). Those simulations are thus not optimized for scientific return[2] and the approach described in Appendix A will have to be carried out again in the future for the 1/4° and 1/8° configuration of the model. Yet, even those imperfect 1/4° and 1/8° simulations with the Saturn DYNAMICO GCM demonstrate the potential of the model to better resolve eddies, waves and vortices with refined horizontal resolution, as is shown in Fig. 20 and in the movie included as supplementary material, showing wind amplitude and vorticity from the 1/8° Saturn DYNAMICO simulation.

Finally, we note that the Saturn DYNAMICO GCM is only a first step towards a GCM system able to simulate the atmospheres of all giant planets, ice giants Uranus and Neptune included. The development of the Jupiter DYNAMICO GCM is currently ungoing (Guerlet and Spiga, 2016; Boissinot et al., 2018), along the lines drawn for Saturn by Guerlet et al. (2014) and this study. The similarities and differences between Jupiter and Saturn in their banded jets (Ingersoll, 1990; Dowling, 1995; Kaspi et al., 2018), eddy activity (Salyk et al., 2006) equatorial oscillations (Li and Read, 2000; Simon-Miller et al., 2007), large-scale vortices (Youssef and Marcus, 2003; Fletcher et al., 2010b; Simon et al., 2014; Legarreta and Sánchez-Lavega, 2005) relate to fundamental research in geophysical fluid dynamics. Employing GCMs for giant planets could help, along with observations, to reach a detailed understanding of the big picture of giant planets' climate and meteorology. This is all the more relevant to prepare the next round of observations of the giant planets, with either probes (Mousis et al., 2014), telescopes (Norwood et al., 2014), or orbiting spacecraft

(Cavalié et al., 2017).

Appendix A. Impact of assumptions in the dynamical core

Numerical subgrid-scale dissipation in the model was found to be a critical setting to deal with. The sensitivity of simulated jets with horizontal dissipation is a common issue in GCM: it was specifically discussed for the cases of Venus (Lebonnois et al., 2013), Titan (Newman et al., 2011), and hot Jupiters (Thrastarson and Cho, 2011). This is a particularly important issue for a gas giant GCM, and it is discussed in Section A.1. Another important question is to explore the behaviour of global axial angular momentum in our Saturn DYNAMICO GCM simulations, which is done in Section A.1.

As far as the sensitivity of the modeled jets to the settings adopted for bottom drag (τ_R, φ_R) is concerned, we rely on the work by Liu and Schneider (2010) and Liu and Schneider (2011), and adopt their settings $\tau_R = 100$ Earth days and $\varphi_R = 33°$ for our reference simulation. Simulations with Saturn DYNAMICO carried out with different values of those parameters (respectively $\tau_R = 10$ Earth days and $\varphi_R = 10°$) confirm the conclusions of Liu and Schneider (2010) and Liu and Schneider (2011) that the bottom drag affects the jets' width and speed.

A.1. Exploring the impact of dissipation

A subgrid-scale dissipation term is included in our Saturn DYNAMICO GCM to prevent the accumulation of energy at scales close to the grid resolution, caused by the GCM not resolving the turbulent scales at which this energy is dissipated. This hyperviscosity term is written in our Saturn DYNAMICO model as an iterated Laplacian term on a given variable ψ

$$\left[\frac{\mathrm{d}\psi}{\mathrm{d}t} \right]_{\mathrm{dissip}} = \frac{(-1)^{q+1} \, \ell_{\min}^2}{\tau_D^{\psi}} \, \nabla^{2q}\psi$$

(16)

where q is the order of dissipation and τ_D^{ψ} the damping timescale associated with the variable ψ at the smallest spatial scale $\ell_{\min}$ resolved by the model for a given horizontal discretization. Large values of τ_D^{ψ} means weaker dissipation: τ_D^{ψ} is the times it takes to dissipate a perturbation on variable ψ

---

[2] This is all the more true since the outcome of a 2-Saturn-year simulation at 1/2° (hence not fully spun-up) was used to initialize a 1/4° simulation, and similarly from the 1/4° to the 1/8° simulations.

developing at the spatial scale $\ell_{\min}$. The three variables denoted by ψ are vorticity, divergence, and potential temperature, chosen to set horizontal dissipation on respectively the rotational component of the flow (e.g. Rossby waves), the divergent component of the flow (e.g. gravity waves), and the diabatic perturbations (e.g. coming from the physical packages). In GCMs for telluric planets, strong variations from one grid point to one another result from topography contrasts or mesoscale convective cells, which calls for a preferential damping on the divergent flow (Hourdin et al., 2012). In our Saturn DYNAMICO GCM simulations, we adopt a simpler approach and we set the same dissipation rate for all three variables, namely $\tau_D^\psi \equiv \tau_D$ for divergence, vorticity and potential temperature.

In the GCM methodology, suitable values of (q, τ_D) are determined empirically, using a combination of past modeling experiences and trial-and-error approach using GCM simulations. The "right" settings for numerical dissipation is a trade-off between ensuring model stability, damping energy at the smallest resolved scales, and minimizing impact on the large-scale flow. A common practice is q ranging between 1 and 4, and τ_D typically one-two terrestrial hours (2000–5000 s) for a $1/2° − 1°$ GCM simulation. We chose $q = 2$ (fourth-order dissipation) for the Saturn DYNAMICO GCM simulations, since it is the setting adopted by our team for GCM for telluric bodies (Hourdin et al., 1995; Lebonnois et al., 2010), and because $q = 1$ is overly dissipative on circulations at large scales, while $q = 3$ led to results similar to $q = 2$. We then carried out several one-Saturn-year simulations with our Saturn DYNAMICO GCM to explore the sensitivity of the computed tropospheric jet structure to the dissipation timescale τ_D.
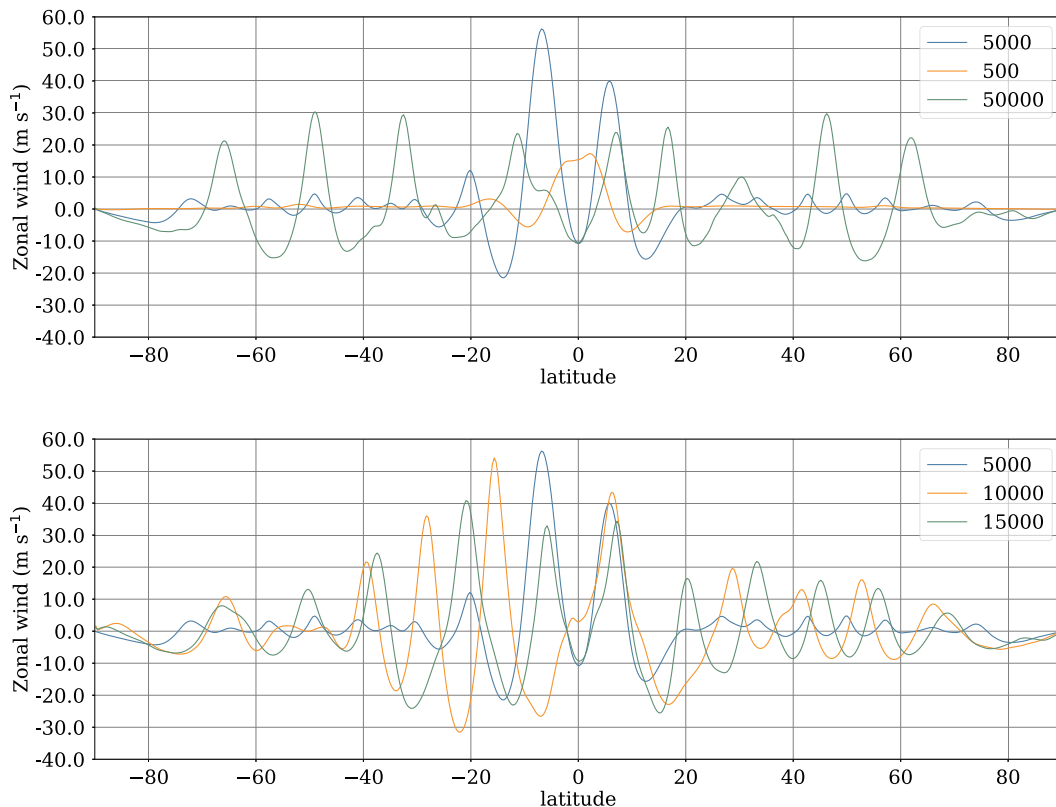

Fig. 21. Zonal-mean jets obtained at cloud level after 20,000 integrated Saturn days (about one simulated Saturn year) with our Saturn DYNAMICO GCM run at a horizontal resolution of $1/2°$. Those tests were carried out with a preceding, slightly different, version of the DYNAMICO model compared to the one used for the reference simulations of Section 3. In the top plot, results are shown for three values of horizontal dissipation timescales varying by one order of magnitude (orange: strong $\tau_D = 500$ s, blue: moderate $\tau_D = 5000$ s, green: weak $\tau_D = 50,000$ s). In the bottom plot, results are shown for three values of horizontal dissipation timescales, two of them (blue: $\tau_D = 5000$ s, green: $\tau_D = 15,000$ s) enclosing the value chosen for the reference simulation discussed in sections 3 and 4 (orange: $\tau_D = 10,000$ s). (For interpretation of the references to color in this figure legend, the reader is referred to the web version of this article.)

Fig. 21 shows that the simulated tropospheric jets in our $1/2°$ Saturn DYNAMICO GCM simulations are sensitive to the value assumed for dissipation timescale τ_D. A first order-of-magnitude sensitivity study (Fig. 21, top) using extreme values disqualifies the strongest dissipation rate ($\tau_D = 500$) which damps the mid-latitude jets out of existence. Setting a weak dissipation ($\tau_D = 50,000$) lets jets significantly accelerate within one simulated year — before the GCM simulation undergoes numerical instabilities in the second year of simulation. A refined sensitivity study (Fig. 21, bottom) indicates that results obtained with $\tau_D = 10,000$ or $\tau_D = 15,000$ are essentially similar: the choice of dissipation mainly impacts jets' meridional location.

The selective criterion to choose τ_D for our reference Saturn DYNAMICO GCM simulation is then based on observations of Saturn's jets (Porco et al., 2005; García-Melendo et al., 2010; Studwell et al., 2018) from which we argue that, qualitatively, $\tau_D = 10,000$ sets a more realistic velocity profile. With $\tau_D = 5000$, high and mid latitudes jets are inconsistently weak, while $\tau_D = 15,000$ smoothes the prevailing contrast that exists between equatorial and high-/mid-latitude jets. The value of $\tau_D = 10,000$ is thus adopted for the 15-year-long reference simulation discussed in Sections 3 and 4. It is important to note here that $\tau_D = 15,000$ would have been an acceptable choice as well. Fig. 21 (right) shows that, even the intensity and location of jets can be different between the Saturn DYNAMICO GCM simulations with either $\tau_D = 10,000$ or $\tau_D = 15,000$, the overall jet structure is qualitatively similar in both cases.

To understand why dissipation impacts the jets, it is important to keep in mind that eddies, which putatively drive the jets, have typical length scales of a couple degrees latitude for a grid spacing of 0.5° (assuming the eddies are baroclinically driven and taking the Rossby radius of

deformation as a first-order theoretical estimate of the eddy length scale, e.g. Young and Read, 2017). These eddies are thus potentially dampened by numerical dissipation that dominantly acts on the smallest-resolved scales. Undoubtedly, the next challenge is to refine GCM resolution towards 1/4° (or better) to enhance simulations of eddies, and hence planetary jets. Even at such refined horizontal resolution though, the chosen value of τ_D will still be impacting the jets' intensities and locations (see also Eq. (21) in Section A.1). Ultimately, how dissipative the Saturn atmosphere is for small-scale circulations remains an open question and difficult to constrain with observations (Ingersoll et al., 2018).

A.1. Angular momentum

The atmospheric Axial Angular momentum (AAM) $\mathcal{M}$ is defined by the sum of the planetary contribution $\mathcal{M}^m$ associated with the solid-body rotation of the planetary sphere and the relative contribution $\mathcal{M}^w$ associated with the motions of the atmosphere with respect to the solid-body rotating reference

$$\mathcal{M} = \mathcal{M}^m + \mathcal{M}^w = \int_V \mu^m \, \mathrm{d}m + \int_V \mu^w \, \mathrm{d}m \tag{17}$$

where $\int_V$ denotes global integration over the volume of the atmosphere and μ denotes the AAM terms per unit mass for respectively the planetary and relative contributions

$$\mu^m = \Omega \, a^2 \cos^2 \varphi \qquad \mu^w = u \, a \cos \varphi \tag{18}$$

Thus, the temporal evolution of AAM is either related to atmospheric mass redistribution (that is, the temporal evolution of surface pressure) or wind variability (that is, the temporal evolution of zonal wind). Assuming that hydrostatic primitive equations are considered, and in the absence of any surface torque and zonal mechanical forcing, the globally-integrated AAM $\mathcal{M}$ is conserved provided the top lid does not vary with longitude (Staniforth and Wood, 2003; Thuburn, 2008; Lauritzen et al., 2014), which is ensured by the DYNAMICO formulation (Dubos et al., 2015).
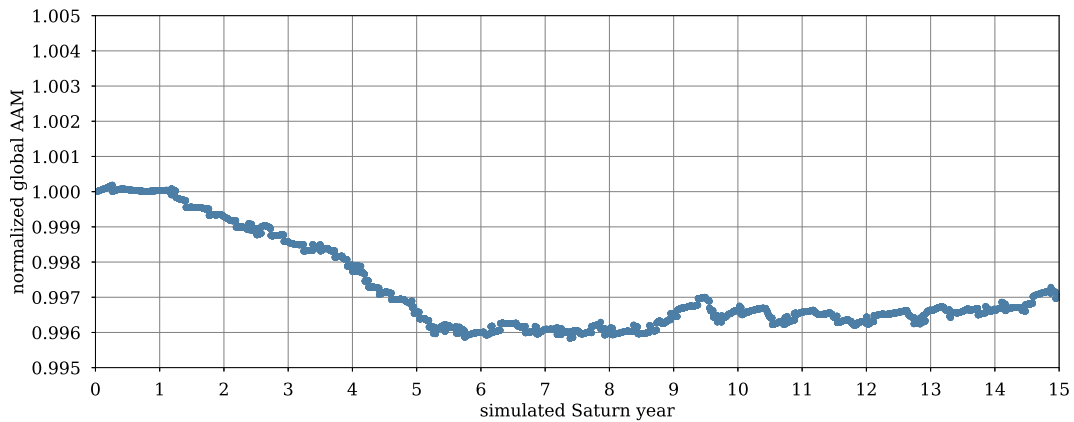

Fig. 22. Temporal evolution of the global AAM $\mathcal{M}$ (normalized to the initial value $\mathcal{M}_0 = 5.244 \times 10^{32}$ kg m^2 s^{-1}) for the complete duration of our reference Saturn GCM simulation.

The conservation of global AAM $\mathcal{M}$ in our Saturn DYNAMICO model is satisfying (Fig. 22). There is a very small decrease of global AAM ($\sim$ 0.4%) in the first six simulated Saturn years, which correspond to the dynamical spin-up of our model, before the global AAM stabilizes at a final value and only undergoes negligible temporal variations of the order $\sim$ 0.05%. The properties of AAM conservation of our Saturn DYNAMICO model compare very favorably to the performance of the dynamical cores described in Polichtchouk et al. (2014), where most models exhibit typical AAM drifts of 1–2%(reaching several tens of % for one particular model).

In addition to the conservation of global AAM, negligible "AAM noise" must be ensured (Lebonnois et al., 2012; Lauritzen et al., 2014). How the temporal evolution of global atmospheric AAM splits between each term of the GCM tendencies can be written

$$\frac{\mathrm{d}\mathcal{M}}{\mathrm{d}t} = \frac{\mathrm{d}\mathcal{M}^m}{\mathrm{d}t} + \frac{\mathrm{d}\mathcal{M}^w}{\mathrm{d}t} = F + T + S + D + \varepsilon, \tag{19}$$

where F is the AAM tendency associated with subgrid-scale mixing in the physical packages (mostly boundary-layer effects), T is the AAM tendency associated with mountain torques, S is the AAM tendency associated with upper sponge layer (a reminder that upper-level sponge layer might alter significantly the AAM balance, Shaw and Shepherd, 2007), D is the AAM tendency due to conservation errors in the parameterization of horizontal dissipation, and ε is a residual numerical rate of AAM variation due to conservation errors (hereinafter named the "AAM noise" since it is a spurious source/sink of AAM in the model). The AAM noise ε can be diagnosed in a GCM by adding the temporal variations of $\mathcal{M}^m$ and $\mathcal{M}^w$ computed by the primitive equations (PE) in the dynamical core, excluding any term accounted for in F, T, S or D (e.g. explicit diffusion operators are included in D)

$$\varepsilon = \left[\frac{\mathrm{d}\mathcal{M}^m}{\mathrm{d}t} \right]_{PE} + \left[\frac{\mathrm{d}\mathcal{M}^w}{\mathrm{d}t} \right]_{PE} \tag{20}$$

In the impossible perfect situation where no numerical approximations or errors are made in the GCM dynamical core when solving the primitive equations, the AAM noise ε should be zero since AAM is exactly transferred from the solid-body rotation to the atmospheric flow and vice versa; a GCM simulation where ε is of similar or larger magnitude than the other torques would be questionable (Lauritzen et al., 2014).

In our Saturn GCM simulations with DYNAMICO, D also includes the Rayleigh friction at the bottom of the atmosphere, S is zero because no upper-level sponge layer is used, T is zero since gas giants are devoid of surface, and for a similar reason, in practice the term F is one order of

magnitude smaller than other terms. This means that in the case of our Saturn GCM (and more generally for any gas giant GCM) Eq. (19) reduces to

$$\frac{\mathrm{d}\mathcal{M}}{\mathrm{d}t} = \frac{\mathrm{d}\mathcal{M}^m}{\mathrm{d}t} + \frac{\mathrm{d}\mathcal{M}^w}{\mathrm{d}t} = D + \varepsilon \qquad (21)$$

Hence, the angular momentum noise ε has potentially a strong impact on the temporal AAM variability in a gas giant GCM. A similar concern is raised by Lebonnois et al. (2012) in the case of idealized Venus simulations without topography. The requirement of low AAM noise is less stringent in realistic GCM simulations for Earth, Venus, or Titan where the contribution of mountain torques T is large (Lebonnois et al., 2012; Lauritzen et al., 2014).
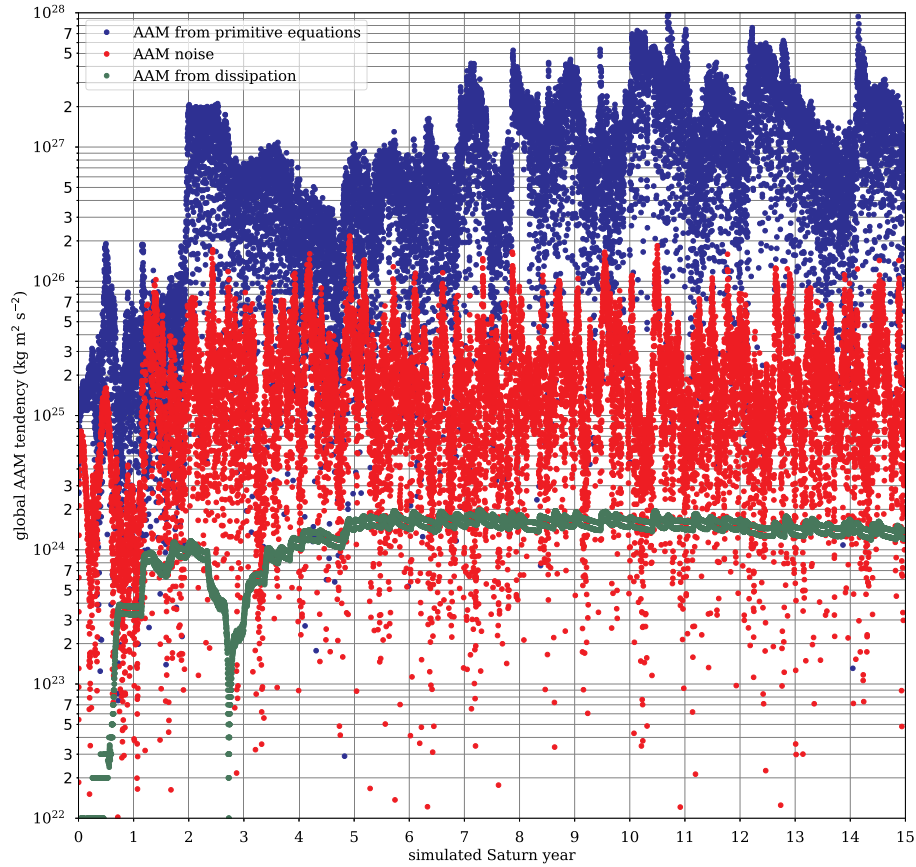

Fig. 23. Temporal evolution of the tendency $\mathrm{d}\mathcal{M}/\mathrm{d}t$ of global AAM for the complete duration of our reference Saturn GCM simulation. Blue points depict the term $[\mathrm{d}\mathcal{M}^w/\mathrm{d}t]_{PE}$ associated with wind tendencies computed in the primitive equations resolved in the dynamical core of the Saturn GCM. Red points depict the term ε associated with AAM noise, i.e. residual numerical rate of AAM variation due to conservation errors. Green points depict the term D associated with AAM tendencies resulting in the dissipation and Rayleigh drag scheme. The log-scale figure is produced with the absolute values of the various tendencies $\mathrm{d}\mathcal{M}/\mathrm{d}t$. (For interpretation of the references to color in this figure legend, the reader is referred to the web version of this article.)

Compared to the analysis presented in Lebonnois et al. (2012) and Lauritzen et al. (2014) for telluric planets, the analysis of AAM noise is more straightforward for gas giants. The following condition[3] must be ensured

$$\varepsilon \ll \left[\frac{\mathrm{d}\mathcal{M}^w}{\mathrm{d}t} \right]_{PE} \qquad (22)$$

Fig. 23 shows that this condition (22) is fulfilled in our Saturn GCM, with AAM noise being one to two orders of magnitude smaller than AAM tendencies computed in the dynamical core's primitive equations (except for a short duration close to one and half simulated year). This indicates that AAM noise does not alter the dynamical predictions for jets and eddies. The same conclusion stands for the AAM tendencies associated with dissipation and Rayleigh drag (Fig. 23), which are even smaller than the AAM noise. This indicates that the horizontal dissipation set in our GCM

---

[3] This condition is equivalent to

$$\varepsilon + D \ll \frac{\mathrm{d}\mathcal{M}^w}{\mathrm{d}t},$$

i.e. the gas-giant (simplified) equivalent of the condition in Lebonnois et al. (2012)

$$\varepsilon^* \ll \frac{\mathrm{d}\mathcal{M}^w}{\mathrm{d}t}$$

(Section A.1) has a negligible impact on the AAM budget — this is consistent with the overall jet structure being similar in simulations using either $\tau_D = 10,000$ or $\tau_D = 15,000$.

In an attempt to explore the model settings that could influence the AAM noise ε, we found that it is basically insensitive to time step, vertical discretization, horizontal dissipation (only a very strong horizontal dissipation significantly lowers AAM noise, but adversely impacts the intensity of jets). This is consistent with Lauritzen et al. (2014) conclusions that AAM noise is likely related to small conservation errors associated with the horizontal discretization of primitive equations. The low AAM noise in our Saturn DYNAMICO GCM simulation level ensures that dynamical spin-up of the jets is not due to convergence of numerically-spurious angular momentum.

References

Achterberg, R.K., Flasar, F.M., 1996. Planetary-scale thermal waves in Saturn's upper troposphere. Icarus 119, 350–369.

Andrews, D.G., Holton, J.R., Leovy, C.B., 1987. Middle Atmosphere Dynamics. Academic Press.

Andrews, D.G., Mahlman, J.D., Sinclair, R.W., 1983. Eliassen-Palm diagnostics of wave-mean flow interaction in the GFDL "SKYHI" general circulation model. J. Atmos. Sci. 40, 2768–2784.

Antuñano, A., Río-Gazteelurrutia, T., Sánchez-Lavega, A., Hueso, R., 2015. Dynamics of Saturn's polar regions. J. Geophys. Res. Planets 120, 155–176.

Aurnou, J., Heimpel, M., Allen, L., King, E., Wicht, J., 2008. Convective heat transfer and the pattern of thermal emission on the gas giants. Geophys. J. Int. 173, 793–801.

Baines, K.H., Momary, T.W., Fletcher, L.N., Showman, A.P., Roos-Serote, M., Brown, R.H., Buratti, B.J., Clark, R.N., Nicholson, P.D., 2009. Saturn's north polar cyclone and hexagon at depth revealed by Cassini/VIMS. Planet. Space Sci. 57, 1671–1681.

Baines, K.H., Sromovsky, L.A., Fry, P.M., Momary, T.W., Brown, R.H., Buratti, B.J., Clark, R.N., Nicholson, P.D., Sotin, C., 2018. The eye of Saturn's North Polar vortex: unexpected cloud structures observed at high spatial resolution by Cassini/VIMS. Geophys. Res. Lett. 45, 5867–5875.

Baldwin, M.P., Gray, L.J., Dunkerton, T.J., Hamilton, K., Haynes, P.H., Randel, W.J., Holton, J.R., Alexander, M.J., Hirota, I., Horinouchi, T., Jones, D.B.A., Kinnersley, J.S., Marquardt, C., Sato, K., Takahashi, M., 2001. The quasi-biennial oscillation. Rev. Geophys. 39, 179–229.

Barbosa Aguiar, A.C., Read, P.L., Wordsworth, R.D., Salter, T., Hiro Yamazaki, Y., 2010. A laboratory model of Saturn's North Polar hexagon. Icarus 206, 755–763.

Barlow, M., 2017, mathewbarlow/potential-vorticity: minor fix (version 1.2).

Boissinot, A., Spiga, A., Guerlet, S., Cabanes, S., 2018. Modeling atmospheric dynamics in Jupiter's troposphere. In: volume 10 of European Planetary Science Congress 2018 Conference Abstracts, pages EPSC2018–1050.

Bouchet, F., Nardini, C., Tangarife, T., 2013. Kinetic theory of jet dynamics in the stochastic barotropic and 2D Navier-Stokes equations. J. Stat. Phys. 153, 572–625.

Bouchet, F., Simonnet, E., 2009. Random changes of flow topology in two-dimensional and geophysical turbulence. Phys. Rev. Lett. 102 (9), 094504.

Butchart, N., 2014. The Brewer-Dobson circulation. Rev. Geophys. 52, 157–184.

Cabanes, S., Aurnou, J., Favier, B., Le Bars, M., 2017. A laboratory model for deep-seated jets on the gas giants. Nat. Phys.

Cavalié, T., Fletcher, L., Krupp, N., Masters, A., Witasse, O., 2017. Exploration of Jupiter's atmosphere and magnetosphere with the European Jupiter Icy Moons Explorer (JUICE). In: European Planetary Science Congress. 11.

Charnay, B., Forget, F., Wordsworth, R., Leconte, J., Millour, E., Codron, F., Spiga, A., 2013. Exploring the faint young Sun problem and the possible climates of the Archean Earth with a 3-D GCM. J. Geophys. Res. Atmos. 118 (D17), 10414.

Chemke, R., Kaspi, Y., 2015a. Poleward migration of eddy-driven jets. J. Adv. Model. Earth Syst. 7, 1457–1471.

Chemke, R., Kaspi, Y., 2015b. The latitudinal dependence of atmospheric jet scales and macroturbulent energy cascades. J. Atmos. Sci. 72, 3891–3907.

Cho, J.Y.-K., Polvani, L.M., 1996. The emergence of jets and vortices in freely evolving, shallow-water turbulence on a sphere. Phys. Fluids 8, 1531–1552.

Colaïtis, A., Spiga, A., Hourdin, F., Rio, C., Forget, F., Millour, E., 2013. A thermal plume model for the Martian convective boundary layer. J. Geophys. Res. Planets 118, 1468–1487.

Cosentino, R.G., Morales-Juberías, R., Greathouse, T., Orton, G., Johnson, P., Fletcher, L.N., Simon, A., 2017. New observations and modeling of Jupiter's quasi-quadrennial oscillation. J. Geophys. Res. Planets 122, 2719–2744.

Del Genio, A.D., Achterberg, R.K., Baines, K.H., Flasar, F.M., Read, P.L., Sánchez-Lavega, A., Showman, A.P., 2009. Saturn Atmospheric Structure and Dynamics. In: Dougherty, M.K., Esposito, L.W., Krimigis, S.M. (Eds.), Springer, pp. 113.

Del Genio, A.D., Barbara, J.M., 2012. Constraints on Saturn's tropospheric general circulation from Cassini ISS images. Icarus 219, 689–700.

Del Genio, A.D., Barbara, J.M., Ferrier, J., Ingersoll, A.P., West, R.A., Vasavada, A.R., Spitale, J., Porco, C.C., 2007. Saturn eddy momentum fluxes and convection: first estimates from Cassini images. Icarus 189, 479–492.

del Río-Gazteelurrutia, T., Hueso, R., Sánchez-Lavega, A., 2012. The storm alley in the southern hemisphere: analysis of Saturn's mid-scale storm dynamics in the Cassini era. In: In European Planetary Science Congress 2012, pages EPSC2012–332.

del Río-Gazteelurrutia, T., Sánchez-Lavega, A., Antuñano, A., Legarreta, J., García-Melendo, E., Sayanagi, K.M., Hueso, R., Wong, M.H., Pérez-Hoyos, S., Rojas, J.F., Simon, A.A., de Pater, I., Blalock, J., Barry, T., 2018. A planetary-scale disturbance in a long living three vortex coupled system in Saturn's atmosphere. Icarus 302, 499–513.

Dowling, T.E., 1995. Dynamics of jovian atmospheres. Annu. Rev. Fluid Mech 27, 293–334.

Dowling, T.E., 2008. Music of the stratospheres. Nature 453, 163–164.

Dowling, T.E., Bradley, M.E., Colón, E., Kramer, J., Lebeau, R.P., Lee, G.C.H., Mattox, T.I., Morales-Juberías, R., Palotai, C.J., Parimi, V.K., Showman, A.P., 2006. The EPIC atmospheric model with an isentropic/terrain-following hybrid vertical coordinate. Icarus 182, 259–273.

Dowling, T.E., Fischer, A.S., Gierasch, P.J., Harrington, J., Lebeau, R.P., Santori, C.M., 1998. The explicit planetary isentropic-coordinate (EPIC) atmospheric model. Icarus 132, 221–238.

Dritschel, D.G., McIntyre, M.E., 2008. Multiple jets as pv staircases: the Phillips effect and the resilience of eddy-transport barriers. J. Atmos. Sci. 65 (3), 855–874.

Dritschel, D.G., Scott, R.K., 2011. Jet sharpening by turbulent mixing. Philosophical Transactions of the Royal Society of London A: Mathematical. Phys. Eng. Sci. 369 (1937), 754–770.

Dubos, T., Dubey, S., Tort, M., Mittal, R., Meurdesoif, Y., Hourdin, F., 2015. Dynamico-1.0, an icosahedral hydrostatic dynamical core designed for consistency and versatility. Geosci. Model Dev. 8 (10), 3131–3150.

Dunkerton, T.J., Scott, R.K., 2008. A barotropic model of the angular momentum-conserving potential vorticity staircase in spherical geometry. J. Atmos. Sci. 65 (4), 1105–1136.

Dyudina, U.A., Ingersoll, A.P., Ewald, S.P., Porco, C.C., Fischer, G., Kurth, W., Desch, M., Del Genio, A., Barbara, J., Ferrier, J., 2007. Lightning storms on Saturn observed by Cassini ISS and RPWS during 2004 2006. Icarus 190, 545–555.

Dyudina, U.A., Ingersoll, A.P., Ewald, S.P., Vasavada, A.R., West, R.A., Del Genio, A.D., Barbara, J.M., Porco, C.C., Achterberg, R.K., Flasar, F.M., Simon-Miller, A.A., Fletcher, L.N., 2008. Dynamics of Saturn's south polar vortex. Science 319.

Fischer, G., Kurth, W.S., Gurnett, D.A., Zarka, P., Dyudina, U.A., Ingersoll, A.P., Ewald, S.P., Porco, C.C., Wesley, A., Go, C., Delcroix, M., 2011. A giant thunderstorm on Saturn. Nature 475, 75–77.

Flasar, F.M., Achterberg, R.K., Conrath, B.J., Pearl, J.C., Bjoraker, G.L., Jennings, D.E., Romani, P.N., Simon-Miller, A.A., Kunde, V.G., Nixon, C.A., Bézard, B., Orton, G.S., Spilker, L.J., Spencer, J.R., Irwin, P.G.J., Teanby, N.A., Owen, T.C., Brasunas, J., Segura, M.E., Carlson, R.C., Mamoutkine, A., Gierasch, P.J., Schinder, P.J., Showalter, M.R., Ferrari, C., Barucci, A., Courtin, R., Coustenis, A., Fouchet, T., Gautier, D., Lellouch, E., Marten, A., Prangé, R., Strobel, D.F., Calcutt, S.B., Read, P.L., Taylor, F.W., Bowles, N., Samuelson, R.E., Abbas, M.M., Raulin, F., Ade, P., Edgington, S., Pilorz, S., Wallis, B., Wishnow, E.H., 2005. Temperatures, winds, and composition in the Saturnian system. Science 307, 1247–1251.

Fletcher, L., Orton, G., Sinclair, J., Guerlet, S., Read, P., Antuñano, A., Achterberg, R., Flasar, F., Irwin, P., Bjoraker, G., et al., 2018. A hexagon in Saturn's northern stratosphere surrounding the emerging summertime polar vortex. Nat. Commun. 9.

Fletcher, L.N., Achterberg, R.K., Greathouse, T.K., Orton, G.S., Conrath, B.J., Simon-Miller, A.A., Teanby, N., Guerlet, S., Irwin, P.G.J., Flasar, F.M., 2010a. Seasonal change on Saturn from Cassini/CIRS observations, 2004-2009. Icarus 208, 337–352.

Fletcher, L.N., Baines, K.H., Momary, T.W., Showman, A.P., Irwin, P.G.J., Orton, G.S., Roos-Serote, M., Merlet, C., 2011a. Saturn's tropospheric composition and clouds from Cassini/VIMS 4.6–5.1 μm nightside spectroscopy. Icarus 214, 510–533.

Fletcher, L.N., Guerlet, S., Orton, G.S., Cosentino, R.G., Fouchet, T., Irwin, P.G.J., Li, J., Flasar, F.M., Gorius, N., Morales-Juberías, R., 2017. Disruption of Saturn's quasi-periodic equatorial oscillation by the great northern storm. Nature Astronomy 1, 765–770.

Fletcher, L.N., Hesman, B.E., Achterberg, R.K., Irwin, P.G.J., Bjoraker, G., Gorius, N., Hurley, J., Sinclair, J., Orton, G.S., Legarreta, J., García-Melendo, E., Sánchez-Lavega, A., Read, P.L., Simon-Miller, A.A., Flasar, F.M., 2012. The origin and evolution of Saturn's 2011–2012 stratospheric vortex. Icarus 221, 560–586.

Fletcher, L.N., Hesman, B.E., Irwin, P.G.J., Baines, K.H., Momary, T.W., Sanchez-Lavega, A., Flasar, F.M., Read, P.L., Orton, G.S., Simon-Miller, A., Hueso, R., Bjoraker, G.L., Mamoutkine, A., del Rio-Gazteelurrutia, T., Gomez, J.M., Buratti, B., Clark, R.N., Nicholson, P.D., Sotin, C., 2011b. Thermal structure and dynamics of Saturn's northern springtime disturbance. Science 332 1413-.

Fletcher, L.N., Irwin, P.G.J., Sinclair, J.A., Orton, G.S., Giles, R.S., Hurley, J., Gorius, N., Achterberg, R.K., Hesman, B.E., Bjoraker, G.L., 2015. Seasonal evolution of Saturn's polar temperatures and composition. Icarus 250, 131–153.

Fletcher, L.N., Irwin, P.G.J., Teanby, N.A., Orton, G.S., Parrish, P.D., de Kok, R., Howett, C., Calcutt, S.B., Bowles, N., Taylor, F.W., 2007. Characterising Saturn's vertical temperature structure from Cassini/CIRS. Icarus 189, 457–478.

Fletcher, L.N., Orton, G.S., Mousis, O., Yanamandra-Fisher, P., Parrish, P.D., Irwin, P.G.J., Fisher, B.M., Vanzi, L., Fujiyoshi, T., Fuse, T., Simon-Miller, A.A., Edkins, E., Hayward, T.L., De Buizer, J., 2010b. Thermal structure and composition of Jupiter's Great Red Spot from high-resolution thermal imaging. Icarus 208, 306–328.

Fouchet, T., Greathouse, T.K., Spiga, A., Fletcher, L.N., Guerlet, S., Leconte, J., Orton, G.S., 2016. Stratospheric aftermath of the 2010 Storm on Saturn as observed by the TEXES instrument. I. Temperature structure. Icarus 277, 196–214.

Fouchet, T., Guerlet, S., Strobel, D.F., Simon-Miller, A.A., Bézard, B., Flasar, F.M., 2008. An equatorial oscillation in Saturn's middle atmosphere. Nature 453, 200–202.

Friedson, A.J., Moses, J.I., 2012. General circulation and transport in Saturn's upper troposphere and stratosphere. Icarus 218, 861–875.

Galanti, E., Kaspi, Y., 2017. Prediction for the flow-induced gravity field of Saturn: implications for Cassini's grand finale. Astron. J. Lett 843, L25.

Galanti, E., Kaspi, Y., Miguel, Y., Guillot, T., Durante, D., Racioppa, P., Iess, L., 2019. Saturn's deep atmospheric flows revealed by the Cassini grand finale gravity measurements. Geophys. Res. Lett. 46, 616–624.

Galperin, B., Young, R.M.B., Sukoriansky, S., Dikovskaya, N., Read, P.L., Lancaster, A.J., Armstrong, D., 2014. Cassini observations reveal a regime of zonostrophic macroturbulence on Jupiter. Icarus 229, 295–320.

García-Melendo, E., Hueso, R., Sánchez-Lavega, A., Legarreta, J., Del Río-Gaztelurrutia, T., Pérez-Hoyos, S., Sanz-Requena, J.F., 2013. Atmospheric dynamics of Saturn's 2010 giant storm. Nat. Geosci. 6, 525–529.

García-Melendo, E., Sánchez-Lavega, A., Legarreta, J., Perez-Hoyos, S., Hueso, R., 2010. A strong high altitude narrow jet detected at Saturn's equator. Geophys. Res. Lett 37, 22204.

Gastine, T., Wicht, J., Duarte, L.D.V., Heimpel, M., Becker, A., 2014. Explaining Jupiter's magnetic field and equatorial jet dynamics. Geophys. Res. Lett 41, 5410–5419.

Gierasch, P.J., Ingersoll, A.P., Banfield, D., Ewald, S.P., Helfenstein, P., Simon-Miller, A., Vasavada, A., Breneman, H.H., Senske, D.A., Galileo imaging team, 2000. Observation of moist convection in Jupiter's atmosphere. Nature 403, 628–630.

Godfrey, D.A., Moore, V., 1986. The Saturnian ribbon feature — a baroclinically unstable model. Icarus 68, 313–343.

Guerlet, S., Fouchet, T., Bézard, B., Moses, J.I., Fletcher, L.N., Simon-Miller, A.A., Michael Flasar, F., 2010. Meridional distribution of CH_3C_2H and C_4H_2 in Saturn's stratosphere from CIRS/Cassini limb and nadir observations. Icarus 209, 682–695.

Guerlet, S., Fouchet, T., Bézard, B., Flasar, F.M., Simon-Miller, A.A., 2011. Evolution of the equatorial oscillation in Saturn's stratosphere between 2005 and 2010 from Cassini/CIRS limb data analysis. Geophys. Res. Lett 38, 9201.

Guerlet, S., Fouchet, T., Bézard, B., Simon-Miller, A.A., Michael Flasar, F., 2009. Vertical and meridional distribution of ethane, acetylene and propane in Saturn's stratosphere from CIRS/Cassini limb observations. Icarus 203, 214–232.

Guerlet, S., Fouchet, T., Hesman, B., Bjoraker, G., Spiga, A., Sylvestre, M., 2015a. Saturn's stratospheric temperature and composition in 2015 from Cassini/CIRS limb observations. In: AAS/Division for Planetary Sciences Meeting Abstracts #47. of AAS/Division for Planetary Sciences Meeting Abstracts. vol. 47. pp. 311.17.

Guerlet, S., Fouchet, T., Spiga, A., Flasar, F.M., Fletcher, L.N., Hesman, B.E., Gorius, N., 2018. Equatorial oscillation and planetary wave activity in Saturn's stratosphere through the Cassini epoch. J. Geophys. Res. Planets 123, 246–261.

Guerlet, S., Fouchet, T., Vinatier, S., Simon, A.A., Dartois, E., Spiga, A., 2015b. Stratospheric benzene and hydrocarbon aerosols detected in Saturn's auroral regions. Astron. Astrophys 580, A89.

Guerlet, S., Spiga, A., 2016. Radiative and dynamical modeling of Jupiter's atmosphere. In: Of EGU General Assembly Conference Abstracts. vol. 18. pp. 9990.

Guerlet, S., Spiga, A., Sylvestre, M., Indurain, M., Fouchet, T., Leconte, J., Millour, E., Wordsworth, R., Capderou, M., Bezard, B., Forget, F., 2014. Global climate modeling of Saturn's atmosphere. Part I: evaluation of the radiative transfer model. Icarus 238, 110–124.

Guillot, T., Miguel, Y., Militzer, B., Hubbard, W.B., Kaspi, Y., Galanti, E., Cao, H., Helled, R., Wahl, S.M., Iess, L., Folkner, W.M., Stevenson, D.J., Lunine, J.I., Reese, D.R., Biekman, A., Parisi, M., Durante, D., Connerney, J.E.P., Levin, S.M., Bolton, S.J., 2018. A suppression of differential rotation in Jupiter's deep interior. Nature 555, 227–230.

Gunnarson, J.L., Sayanagi, K.M., Blalock, J.J., Fletcher, L.N., Ingersoll, A.P., Dyudina, U.A., Ewald, S.P., Draham, R.L., 2018. Saturn's new ribbons: Cassini observations of planetary waves in Saturn's 42n atmospheric jet. Geophys. Res. Lett. 45 (15), 7399–7408.

Guzewich, S.D., Newman, C.E., de la Torre Juárez, M., Wilson, R.J., Lemmon, M., Smith, M.D., Kahanpää, H., Harri, A.-M., 2016. Atmospheric tides in Gale Crater, Mars. Icarus 268, 37–49.

Haynes, P., McIntyre, M., Shepherd, T., Marks, C., Shine, K.P., 1991. On the "downward control" of extratropical diabatic circulations by eddy-induced mean zonal forces. J. Atmos. Sci. 48 (4), 651–678.

Haynes, P.H., McIntyre, M.E., 1987. On the evolution of vorticity and potential vorticity in the presence of diabatic heating and frictional or other forces. Journal of Atmospheric Sciences 44, 828–841.

Heimpel, M., Aurnou, J., Wicht, J., 2005. Simulation of equatorial and high-latitude jets on Jupiter in a deep convection model. Nature 438, 193–196.

Heimpel, M., Gastine, T., Wicht, J., 2016. Simulation of deep-seated zonal jets and shallow vortices in gas giant atmospheres. Nat. Geosci. 9, 19–23.

Heimpel, M., Gómez Pérez, N., 2011. On the relationship between zonal jets and dynamo action in giant planets. Geophys. Res. Lett 38, 14201.

Holton, J.R., 2004. An introduction to dynamic meteorology. Of International Geophysics Series, 4th ed. 48 Elsevier Academic Press.

Hoskins, B.J., James, I.N., White, G.H., 1983. The shape, propagation and mean-flow interaction of large-scale weather systems. J. Atmos. Sci. 40, 1595–1612.

Hourdin, F., Couvreux, F., Menut, L., 2002. Parameterization of the dry convective boundary layer based on a mass flux representation of thermals. J. Atmos. Sci. 59, 1105–1123.

Hourdin, F., Grandpeix, J.Y., Rio, C., Bony, S., Jam, A., Cheruy, F., Rochetin, N., Fairhead, L., Idelkadi, A., Musat, I., Dufresne, J.L., Lahellec, A., Lefebvre, M.P., Roehrig, R., 2012. Lmdz5b: the atmospheric component of the IPSL climate model with revisited parameterizations for clouds and convection. Clim. Dyn. 79, 2193–2222.

Hourdin, F., Le Van, P., Forget, F., Talagrand, O., 1993. Meteorological variability and the annual surface pressure cycle on Mars. J. Atmos. Sci. 50, 3625–3640.

Hourdin, F., Talagrand, O., Sadourny, R., Régis, C., Gautier, D., McKay, C.P., 1995.

General circulation of the atmosphere of Titan. Icarus 117, 358–374.

Hue, V., Greathouse, T.K., Cavalié, T., Dobrijevic, M., Hersant, F., 2016. 2D photochemical modeling of Saturn's stratosphere. Part II: feedback between composition and temperature. Icarus 267, 334–343.

Hue, V., Hersant, F., Cavalié, T., Dobrijevic, M., Sinclair, J.A., 2018. Photochemistry, mixing and transport in Jupiter's stratosphere constrained by Cassini. Icarus 307, 106–123.

Ingersoll, A.P., 1990. Atmospheric dynamics of the outer planets. Science 248, 308–315.

Ingersoll, A.P., Ewald, S.P., Sayanagi, K.M., Blalock, J.J., 2018. Saturn's atmosphere at 1–10 kilometer resolution. Geophys. Res. Lett 45, 7851–7856.

Karkoschka, E., Tomasko, M.G., 2010. Methane absorption coefficients for the jovian planets from laboratory, Huygens, and HST data. Icarus 205, 674–694.

Kaspi, Y., 2013. Inferring the depth of the zonal jets on Jupiter and Saturn from odd gravity harmonics. Geophys. Res. Lett 40, 676–680.

Kaspi, Y., Flierl, G.R., 2007. Formation of jets by baroclinic instability on gas planet atmospheres. J. Atmos. Sci. 64, 3177.

Kaspi, Y., Flierl, G.R., Showman, A.P., 2009. The deep wind structure of the giant planets: results from an anelastic general circulation model. Icarus 202, 525–542.

Kaspi, Y., Galanti, E., Hubbard, W.B., Stevenson, D.J., Bolton, S.J., Iess, L., Guillot, T., Bloxham, J., Connerney, J.E.P., Cao, H., Durante, D., Folkner, W.M., Helled, R., Ingersoll, A.P., Levin, S.M., Lunine, J.I., Miguel, Y., Militzer, B., Parisi, M., Wahl, S.M., 2018. Jupiter's atmospheric jet streams extend thousands of kilometres deep. Nature 555, 223–226.

Kidston, J., Vallis, G.K., 2010. Relationship between eddy-driven jet latitude and width. Geophys. Res. Lett. 37 (21).

Kiladis, G.N., Wheeler, M.C., Haertel, P.T., Straub, K.H., Roundy, P.E., 2009. Convectively coupled equatorial waves. Rev. Geophys. 47 (2).

Koskinen, T.T., Sandel, B.R., Yelle, R.V., Strobel, D.F., Müller-Wodarg, I.C.F., Erwin, J.T., 2015. Saturn's variable thermosphere from Cassini/UVIS occultations. Icarus 260, 174–189.

Lauritzen, P.H., Bacmeister, J.T., Dubos, T., Lebonnois, S., Taylor, M.A., 2014. Held-Suarez simulations with the Community Atmosphere Model Spectral Element (CAM-SE) dynamical core: a global axial angular momentum analysis using Eulerian and floating Lagrangian vertical coordinates. J. Adv. Model. Earth Syst. 6, 129–140.

Lebonnois, S., Burgalat, J., Rannou, P., Charnay, B., 2012. Titan global climate model: a new 3-dimensional version of the IPSL Titan GCM. Icarus 218, 707–722.

Lebonnois, S., Hourdin, F., Eymet, V., Crespin, A., Fournier, R., Forget, F., 2010. Superrotation of Venus' atmosphere analyzed with a full general circulation model. J. Geophys. Res. Planets 115, 6006.

Lebonnois, S., Lee, C., Yamamoto, M., Dawson, J., Lewis, S.R., Mendonca, J., Read, P.L., Parish, H., Schubert, G., Bengtsson, L., Grinspoon, D., Limaye, S., Schmidt, H., Svedhem, H., Titov, D., 2013. Models of venus atmosphere. In: Bengtsson, L., Bonnet, R.-M., Grinspoon, D., Koumoutsaris, S., Lebonnois, S., Titov, D. (Eds.), Towards understanding the climate of Venus: application of terrestrial models to our sister planet. ISSI Scientific Report series. Vol.11. Springer Netherlands, pp. 129–156.

Leconte, J., Forget, F., Charnay, B., Wordsworth, R., Selsis, F., Millour, E., Spiga, A., 2013. 3D climate modeling of close-in land planets: circulation patterns, climate moist bistability, and habitability. Astron. Astrophys. 554, A69.

Legarreta, J., Sánchez-Lavega, A., 2005. Jupiter's cyclones and anticyclones vorticity from Voyager and Galileo images. Icarus 174, 178–191.

Lewis, S.R., Barker, P.R., 2005. Atmospheric tides in a Mars general circulation model with data assimilation. Adv. Space Res 36, 2162–2168.

Li, L., Gierasch, P.J., Achterberg, R.K., Conrath, B.J., Flasar, F.M., Vasavada, A.R., Ingersoll, A.P., Banfield, D., Simon-Miller, A.A., Fletcher, L.N., 2008. Strong jet and a new thermal wave in Saturn's equatorial stratosphere. Geophys. Res. Lett 35 23208-+.

Li, L., Ingersoll, A.P., Huang, X., 2006. Interaction of moist convection with zonal jets on Jupiter and Saturn. Icarus 180, 113–123.

Li, L., Jiang, X., Ingersoll, A.P., Del Genio, A.D., Porco, C.C., West, R.A., Vasavada, A.R., Ewald, S.P., Conrath, B.J., Gierasch, P.J., Simon-Miller, A.A., Nixon, C.A., Achterberg, R.K., Orton, G.S., Fletcher, L.N., Baines, K.H., 2011. Equatorial winds on Saturn and the stratospheric oscillation. Nat. Geosci. 4, 750–752.

Li, X., Read, P.L., 2000. A mechanistic model of the quasi-quadrennial oscillation in Jupiter's stratosphere. Planet. Space Sci. 48, 637–669.

Lian, Y., Showman, A.P., 2008. Deep jets on gas-giant planets. Icarus 194, 597–615.

Lian, Y., Showman, A.P., 2010. Generation of equatorial jets by large-scale latent heating on the giant planets. Icarus 207, 373–393.

Lindzen, R.S., Holton, J.R., 1968. A theory of the quasi-biennial oscillation. J. Atmos. Sci. 25, 1095–1107.

Liu, J., Goldreich, P.M., Stevenson, D.J., 2008. Constraints on deep-seated zonal winds inside Jupiter and Saturn. Icarus 196, 653–664.

Liu, J., Schneider, T., 2010. Mechanisms of jet formation on the giant planets. J. Atmos. Sci. 67, 3652–3672.

Liu, J., Schneider, T., 2011. Convective generation of equatorial superrotation in planetary atmospheres. J. Atmos. Sci. 68, 2742–2756.

Liu, J., Schneider, T., 2015. Scaling of off-equatorial jets in giant planet atmospheres. J. Atmos. Sci. 72, 389–408.

Lott, F., Denvil, S., Butchart, N., Cagnazzo, C., Giorgetta, M.A., Hardiman, S.C., Manzini, E., Krismer, T., Duval, J.-P., Maury, P., Scinocca, J.F., Watanabe, S., Yukimoto, S., 2014. Kelvin and Rossby-gravity wave packets in the lower stratosphere of some high-top CMIP5 models. J. Geophys. Res. Atmos. 119, 2156–2173.

Lott, F., Guez, L., 2013. A stochastic parameterization of the gravity waves due to convection and its impact on the equatorial stratosphere. J. Geophys. Res. Atmos. 118, 8897–8909.

Marcus, P.S., Shetty, S., 2011. Jupiter's zonal winds: are they bands of homogenized potential vorticity organized as a monotonic staircase? In: Philosophical Transactions

of the Royal Society of London Series A. 369. pp. 771–795.

Maury, P., Lott, F., 2014. On the presence of equatorial waves in the lower stratosphere of a general circulation model. Atmos. Chem. Phys 14, 1869–1880.

Medvedev, A.S., Sethunadh, J., Hartogh, P., 2013. From cold to warm gas giants: a three-dimensional atmospheric general circulation modeling. Icarus 225, 228–235.

Mellor, G.L., Yamada, T., 1982. Development of a turbulence closure model for geo-physical fluid problems. Rev. of Geophys. 20 (4), 851–875.

Meurdesoif, Y., 2012. XIOS Presentation Given at the Workshop on Scalable IO in Climate Models, Hamburg, Germany.

Meurdesoif, Y., 2013. XIOS Presentation Given at the Second Workshop on Coupling Technologies for Earth System Models (CW2013, NCAR), Boulder, Colorado-USA.

Morales-Juberías, R., Sayanagi, K.M., Dowling, T.E., Ingersoll, A.P., 2011. Emergence of polar-jet polygons from jet instabilities in a Saturn model. Icarus 211, 1284–1293.

Morales-Juberías, R., Sayanagi, K.M., Simon, A.A., Fletcher, L.N., Cosentino, R.G., 2015. Meandering shallow atmospheric jet as a model of Saturn's north-polar hexagon. Astron. J. Lett. 806, L18.

Moses, J.I., Bézard, B., Lellouch, E., Gladstone, G.R., Feuchtgruber, H., Allen, M., 2000. Photochemistry of Saturn's atmosphere. I. Hydrocarbon chemistry and comparisons with ISO observations. Icarus 143, 244–298.

Mousis, O., Fletcher, L.N., Lebreton, J.-P., Wurz, P., Cavalié, T., Coustenis, A., Courtin, R., Gautier, D., Helled, R., Irwin, P.G.J., Morse, A.D., Nettelmann, N., Marty, B., Rousselot, P., Venot, O., Atkinson, D.H., Waite, J.H., Reh, K.R., Simon, A.A., Atreya, S., André, N., Blanc, M., Daglis, I.A., Fischer, G., Geppert, W.D., Guillot, T., Hedman, M.M., Hueso, R., Lellouch, E., Lunine, J.I., Murray, C.D., O'Donoghue, J., Rengel, M., Sánchez-Lavega, A., Schmider, F.-X., Spiga, A., Spilker, T., Petit, J.-M., Tiscareno, M.S., Ali-Dib, M., Altwegg, K., Bolton, S.J., Bouquet, A., Briois, C., Fouchet, T., Guerlet, S., Kostiuk, T., Lebleu, D., Moreno, R., Orton, G.S., Poncy, J., 2014. Scientific rationale for Saturn's in situ exploration. Planet. Space Sci. 104, 29–47.

Müller-Wodarg, I.C.F., Moore, L., Galand, M., Miller, S., Mendillo, M., 2012. Magnetosphere-atmosphere coupling at Saturn: 1 — response of thermosphere and ionosphere to steady state polar forcing. Icarus 221, 481–494.

Newman, C.E., Lee, C., Lian, Y., Richardson, M.I., Toigo, A.D., 2011. Stratospheric su-perrotation in the Titan WRF model. Icarus 213, 636–654.

Nissen, K.M., Braesicke, P., Langematz, U., 2000. QBO, SAO, and tropical waves in the Berlin TSM GCM: sensitivity to radiation, vertical resolution, and convection. J. Geophys. Res. Atmos. 105, 24.

Norwood, J., Hammel, H., Milam, S., Stansberry, J., Lunine, J., Chanover, N., Hines, D., Sonneborn, G., Tiscareno, M., Brown, M., Ferruit, P., 2014. Solar System Observations with JWST. ArXiv e-prints.

O'Gorman, P.A., Schneider, T., 2008. Weather-layer dynamics of baroclinic eddies and multiple jets in an idealized general circulation model. J. Atmos. Sci. 65 (2), 524–535.

O'Neill, M.E., Emanuel, K.A., Flierl, G.R., 2015. Polar vortex formation in giant-planet atmospheres due to moist convection. Nat. Geosci. 8, 523–526.

Orton, G.S., Yanamandra-Fisher, P.A., Fisher, B.M., Friedson, A.J., Parrish, P.D., Nelson, J.F., Bauermeister, A.S., Fletcher, L., Gezari, D.Y., Varosi, F., Tokunaga, A.T., Caldwell, J., Baines, K.H., Hora, J.L., Ressler, M.E., Fujiyoshi, T., Fuse, T., Hagopian, H., Martin, T.Z., Bergstralh, J.T., Howett, C., Hoffmann, W.F., Deutsch, L.K., van Cleve, J.E., Noe, E., Adams, J.D., Kassis, M., Tollestrup, E., 2008. Semi-annual os-cillations in Saturn's low-latitude stratospheric temperatures. Nature 453, 196–199.

Panetta, R.L., 1993. Zonal jets in wide baroclinically unstable regions: persistence and scale selection. J. Atmos. Sci. 50 (14), 2073–2106.

Pérez-Hoyos, S., Sánchez-Lavega, A., 2006. Solar flux in Saturn's atmosphere: penetration and heating rates in the aerosol and cloud layers. Icarus 180, 368–378.

Polichtchouk, I., Cho, J.Y.-K., Watkins, C., Thrastarson, H.T., Umurhan, O.M., de la Torre Juárez, M., 2014. Intercomparison of general circulation models for hot extrasolar planets. Icarus 229, 355–377.

Porco, C.C., Baker, E., Barbara, J., Beurle, K., Brahic, A., Burns, J.A., Charnoz, S., Cooper, N., Dawson, D.D., Del Genio, A.D., Denk, T., Dones, L., Dyudina, U., Evans, M.W., Giese, B., Grazier, K., Helfenstein, P., Ingersoll, A.P., Jacobson, R.A., Johnson, T.V., McEwen, A., Murray, C.D., Neukum, G., Owen, W.M., Perry, J., Roatsch, T., Spitale, J., Squyres, S., Thomas, P., Tiscareno, M., Turtle, E., Vasavada, A.R., Veverka, J., Wagner, R., West, R., 2005. Cassini imaging science: initial results on Saturn's at-mosphere. Science 307, 1243–1247.

Read, P.L., Conrath, B.J., Fletcher, L.N., Gierasch, P.J., Simon-Miller, A.A., Zuchowski, L.C., 2009a. Mapping potential vorticity dynamics on saturn: zonal mean circulation from Cassini and Voyager data. Planet. Space Sci. 57, 1682–1698.

Read, P.L., Dowling, T.E., Schubert, G., 2009b. Saturn's rotation period from its atmo-spheric planetary-wave configuration. Nature 460, 608–610.

Read, P.L., Lebonnois, S., 2018. Superrotation on Venus, on Titan, and elsewhere. Annu. Rev. Earth Planet. Sci 46, 175–202.

Rey, M., Nikitin, A.V., Bézard, B., Rannou, P., Coustenis, A., Tyuterev, V.G., 2018. New accurate theoretical line lists of $^{12}CH_4$ and $^{13}CH_4$ in the 0-13400 cm^{-1} range: appli-cation to the modeling of methane absorption in Titan's atmosphere. Icarus 303, 114–130.

Rhines, P.B., 1975. Waves and turbulence on a beta-plane. J. Fluid Mech. 69 (3), 417–443.

Rio, C., Hourdin, F., 2008. A thermal plume model for the convective boundary layer: representation of cumulus clouds. J. Atmos. Sci. 65, 407–425.

Rostami, M., Zeitlin, V., Spiga, A., 2017. On the dynamical nature of Saturn's North Polar hexagon. Icarus 297, 59–70.

Rothman, L.S., Gordon, I.E., Babikov, Y., Barbe, A., Chris Benner, D., Bernath, P.F., Birk, M., Bizzocchi, L., Boudon, V., Brown, L.R., Campargue, A., Chance, K., Cohen, E.A., Coudert, L.H., Devi, V.M., Drouin, B.J., Fayt, A., Flaud, J.-M., Gamache, R.R., Harrison, J.J., Hartmann, J.-M., Hill, C., Hodges, J.T., Jacquemart, D., Jolly, A., Lamouroux, J., Le Roy, R.J., Li, G., Long, D.A., Lyulin, O.M., Mackie, C.J., Massie,

S.T., Mikhailenko, S., Müller, H.S.P., Naumenko, O.V., Nikitin, A.V., Orphal, J., Perevalov, V., Perrin, A., Polovtseva, E.R., Richard, C., Smith, M.A.H., Starikova, E., Sung, K., Tashkun, S., Tennyson, J., Toon, G.C., Tyuterev, V.G., Wagner, G., 2013. The HITRAN2012 molecular spectroscopic database. J. Quant. Spectrosc. Radiat. Transf. 130, 4–50.

Salyk, C., Ingersoll, A.P., Lorre, J., Vasavada, A., Del Genio, A.D., 2006. Interaction be-tween eddies and mean flow in Jupiter's atmosphere: analysis of Cassini imaging data. Icarus 185, 430–442.

Sanchez-Lavega, A., 2002. Observations of Saturn's ribbon wave 14 years after its dis-covery. Icarus 158, 272–275.

Sánchez-Lavega, A., del Río-Gaztelurrutia, T., Hueso, R., GÓmez-Forrellad, J.M., Sanz-Requena, J.F., Legarreta, J., García-Melendo, E., Colas, F., Lecacheux, J., Fletcher, L.N., Barrado y Navascués, D., Parker, D., International Outer Planet Watch Team, Akutsu, T., Barry, T., Beltran, J., Buda, S., Combs, B., Carvalho, F., Casquinha, P., Delcroix, M., Ghomizadeh, S., Go, C., Hotershall, J., Ikemura, T., Jolly, G., Kazemoto, A., Kumamori, T., Lecompte, M., Maxson, P., Melillo, F.J., Milika, D.P., Morales, E., Peach, D., Phillips, J., Poupeau, J.J., Sussenbach, J., Walker, G., Walker, S., Tranter, T., Wesley, A., Wilson, T., Yunoki, K., 2011. Deep winds beneath Saturn's upper clouds from a seasonal long-lived planetary-scale storm. Nature 475, 71–74.

Sánchez-Lavega, A., García-Melendo, E., Pérez-Hoyos, S., Hueso, R., Wong, M.H., Simon, A., Sanz-Requena, J.F., Antuñano, A., Barrado-Izagirre, N., Garate-Lopez, I., Rojas, J.F., Del Río-Gaztelurrutia, T., Gómez-Forrellad, J.M., de Pater, I., Li, L., Barry, T., 2016. An enduring rapidly moving storm as a guide to Saturn's Equatorial jet's complex structure. Nat. Commun. 7, 13262.

Sánchez-Lavega, A., Río-Gaztelurrutia, T., Hueso, R., Pérez-Hoyos, S., García-Melendo, E., Antuñano, A., Mendikoa, I., Rojas, J.F., Lillo, J., Barrado-Navascués, D., Gomez-Forrellad, J.M., Go, C., Peach, D., Barry, T., Milika, D.P., Nicholas, P., Wesley, A., 2014. The long-term steady motion of saturn's hexagon and the stability of its en-closed jet stream under seasonal changes. Geophys. Res. Lett. 41, 1425–1431.

Sayanagi, K.M., Blalock, J., Dyudina, U.A., Ewald, S.P., Ingersoll, A.P., 2017. Cassini ISS observation of Saturn's north polar vortex and comparison to the south polar vortex. Icarus 285, 68–82.

Sayanagi, K.M., Dyudina, U.A., Ewald, S.P., Fischer, G., Ingersoll, A.P., Kurth, W.S., Muro, G.D., Porco, C.C., West, R.A., 2013. Dynamics of Saturn's great storm of 2010-2011 from Cassini ISS and RPWS. Icarus 223, 460–478.

Sayanagi, K.M., Dyudina, U.A., Ewald, S.P., Muro, G.D., Ingersoll, A.P., 2014. Cassini ISS observation of Saturn's String of Pearls. Icarus 229, 170–180.

Sayanagi, K.M., Morales-Juberías, R., Ingersoll, A.P., 2010. Saturn's Northern Hemisphere Ribbon: Simulations and Comparison with the Meandering Gulf Stream. J. Atmos. Sci. 67, 2658–2678.

Sayanagi, K.M., Showman, A.P., 2007. Effects of a large convective storm on Saturn's equatorial jet. Icarus 187, 520–539.

Schneider, T., Liu, J., 2009. Formation of Jets and Equatorial Superrotation on Jupiter. J. Atmos. Sci. 66 579-+.

Shaw, T.A., Shepherd, T.G., 2007. Angular Momentum Conservation and Gravity Wave Drag Parameterization: Implications for Climate Models. J. Atmos. Sci. 64, 190.

Showman, A.P., 2007. Numerical Simulations of Forced Shallow-Water Turbulence: Effects of Moist Convection on the Large-Scale Circulation of Jupiter and Saturn. J. Atmos. Sci. 64, 3132.

Showman, A.P., Kaspi, Y., Achterberg, R., Ingersoll, A.P., 2018a. The Global Atmospheric Circulation of Saturn. Cambridge University Press, pp. 000.

Showman, A.P., Polvani, L.M., 2011. Equatorial Superrotation on Tidally Locked Exoplanets. Astrophys. J. 738, 71.

Showman, A.P., Tan, X., Zhang, X., 2018b. Atmospheric Circulation of Brown Dwarfs and Jupiter and Saturn-Like Planets: Zonal Jets, Long-Term Variability, and QBO-Type Oscillations. ArXiv e-prints, page arXiv:1807.08433.

Simon, A.A., Wong, M.H., Rogers, J.H., Orton, G.S., de Pater, I., Asay-Davis, X., Carlson, R.W., Marcus, P.S., 2014. Dramatic Change in Jupiter's Great Red Spot from Spacecraft Observations. Astrophys. J. Lett. 797, L31.

Simon-Miller, A.A., Poston, B.W., Orton, G.S., Fisher, B., 2007. Wind variations in jupiter's equatorial atmosphere: A QQO counterpart? Icarus 186, 192–203.

Sinclair, J.A., Irwin, P.G.J., Fletcher, L.N., Moses, J.I., Greathouse, T.K., Friedson, A.J., Hesman, B., Hurley, J., Merlet, C., 2013. Seasonal variations of temperature, acet-ylene and ethane in Saturn's atmosphere from 2005 to 2010, as observed by Cassini-CIRS. Icarus 225, 257–271.

Staniforth, A., Wood, N., 2003. The Deep-Atmosphere Euler Equations in a Generalized Vertical Coordinate. Mon. Weather Rev. 131, 1931.

Studwell, A., Li, L., Jiang, X., Baines, K.H., Fry, P.M., Momary, T.W., Dyudina, U.A., 2018. Saturn's Global Zonal Winds Explored by Cassini/VIMS 5-μm Images. Geophys. Res. Lett 45, 6823–6831.

Sukoriansky, S., Galperin, B., Dikovskaya, N., 2002. Universal Spectrum of Two-Dimensional Turbulence on a Rotating Sphere and Some Basic Features of Atmospheric Circulation on Giant Planets. Phys. Rev. Lett. 89 (12), 124501.

Sylvestre, M., Guerlet, S., Fouchet, T., Spiga, A., Flasar, F.M., Hesman, B., Bjoraker, G.L., 2015. Seasonal changes in Saturn's stratosphere inferred from Cassini/CIRS limb observations. Icarus 258, 224–238.

Takahashi, M., 1996. Simulation of the stratospheric Quasi-Biennial Oscillation using a general circulation model. Geophys. Res. Lett. 23, 661–664.

Thrastarson, H.T., Cho, J.Y., 2011. Relaxation Time and Dissipation Interaction in Hot Planet Atmospheric Flow Simulations. Astrophys. J. 729, 117.

Thuburn, J., 2008. Some conservation issues for the dynamical cores of NWP and climate models. J. Comput. Phys. 227, 3715–3730.

Tort, M., Dubos, T., Melvin, T., 2015. Energy-conserving finite-difference schemes for quasi-hydrostatic equations. Q. J. R. Meteorol. Soc. 141 (693), 3056–3075.

Trammell, H.J., Li, L., Jiang, X., Pan, Y., Smith, M.A., Bering, E.A., Hörst, S.M., Vasavada, A.R., Ingersoll, A.P., Janssen, M.A., West, R.A., Porco, C.C., Li, C., Simon, A.A.,

Baines, K.H., 2016. Vortices in saturn's northern hemisphere (2008-2015) observed by cassini iss. J. Geophys. Res. Planets 121 (9), 1814–1826 2016JE005122.

Vallis, G.K., 2006. Atmospheric and oceanic fluid dynamics: fundamentals and large-scale circulation. Cambridge University Press.

Vasavada, A.R., Hörst, S.M., Kennedy, M.R., Ingersoll, A.P., Porco, C.C., Del Genio, A.D., West, R.A., 2006. Cassini imaging of saturn: Southern hemisphere winds and vortices. J. Geophys. Res. Planets 111, 5004.

Vasavada, A.R., Showman, A.P., 2005. Jovian atmospheric dynamics: an update after Galileo and Cassini. Rep. Prog. Phys. 68, 1935–1996.

Watanabe, S., Kawatani, Y., Tomikawa, Y., Miyazaki, K., Takahashi, M., Sato, K., 2008. General aspects of a T213L256 middle atmosphere general circulation model. J. Geophys. Res. Atmos. 113, D12110.

West, R.A., Friedson, A.J., Appleby, J.F., 1992. Jovian large-scale stratospheric circulation. Icarus 100, 245–259.

Wheeler, M., Kiladis, G.N., 1999. Convectively Coupled Equatorial Waves: Analysis of Clouds and Temperature in the Wavenumber-Frequency Domain. J. Atmos. Sci. 56, 374–399.

Williams, G.P., 2003. Jovian Dynamics. Part III: Multiple, Migrating, and Equatorial Jets. J. Atmos. Sci. 60, 1270–1296.

Wilson, R.W., Hamilton, K., 1996. Comprehensive model simulation of thermal tides in the Martian atmosphere. J. Atmos. Sci. 53, 1290–1326.

Wordsworth, R., 2012. Transient conditions for biogenesis on low-mass exoplanets with escaping hydrogen atmospheres. Icarus 219, 267–273.

Wordsworth, R.D., Forget, F., Selsis, F., Madeleine, J.-B., Millour, E., Eymet, V., 2010. Is Gliese 581d habitable? Some constraints from radiative-convective climate modeling. Astron. Astrophys. 522, A22.

Yano, J.-I., Talagrand, O., Drossart, P., 2005. Deep two-dimensional turbulence: An idealized model for atmospheric jets of the giant outer planets. Geophys. Astrophys. Fluid Dyn 99, 137–150.

Young, R.M.B., Read, P.L., 2017. Forward and inverse kinetic energy cascades in Jupiter's turbulent weather layer. Nat. Phys. 13, 1135–1140.

Young, R.M.B., Read, P.L., Wang, Y., 2019a. Simulating Jupiter's weather layer. Part I: Jet spin-up in a dry atmosphere. Icarus 326, 225–252.

Young, R.M.B., Read, P.L., Wang, Y., 2019b. Simulating Jupiter's weather layer. Part II: Passive ammonia and water cycles. Icarus 326, 253–268.

Youssef, A., Marcus, P.S., 2003. The dynamics of jovian white ovals from formation to merger. Icarus 162, 74–93.

Zuchowski, L.C., Yamazaki, Y.H., Read, P.L., 2009. Modeling Jupiter's cloud bands and decks. 2. Distribution and motion of condensates. Icarus 200, 563–573.